PONTIFICIA UNIVERSIDAD CATOLICA DE CHILE

SCHOOL OF ENGINEERING

MULTISCALE ANALYSIS OF FLOWS PAST MARINE HYDROKINETIC DEVICES USING NUMERICAL SIMULATIONS

KARINA ANDREA SOTO RIVAS

Thesis submitted to the Pontificia Universidad Católica de Chile and University of Notre Dame in partial fulfillment of the requirements for the Degree of Doctor in Engineering Sciences and Doctor of Philosophy

Advisors:

CRISTIÁN ESCAURIAZA & DAVID RICHTER

Santiago de Chile, January, 2021

PONTIFICIA UNIVERSIDAD CATOLICA DE CHILE
SCHOOL OF ENGINEERING

MULTISCALE ANALYSIS OF FLOWS PAST MARINE HYDROKINETIC DEVICES USING NUMERICAL SIMULATIONS

KARINA ANDREA SOTO RIVAS

Members of the Committee:

CRISTIÁN ESCAURIAZA

DAVID RICHTER

RODRIGO CIENFUEGOS

DIOGO BOLSTER

HARINDRA JOSEPH FERNANDO

JUAN DE DIOS ORTÚZAR

Thesis submitted to the Pontificia Universidad Católica de Chile and University of Notre Dame in partial fulfillment of the requirements for the Degree of Doctor in Engineering Sciences and Doctor of Philosophy

Santiago de Chile, January, 2021

MULTISCALE ANALYSIS OF FLOWS PAST MARINE HYDROKINETIC DEVICES USING NUMERICAL SIMULATIONS

A Dissertation

Submitted to the Graduate School
of the University of Notre Dame
in Partial Fulfillment of the Requirements
for the Degree of

Doctor of Philosophy

by

Karina A. Soto Rivas

David Richter , Co-Director

Cristián Escauriaza , Co-Director

Graduate Program in Civil & Environmental Engineering & Earth Sciences
Notre Dame, Indiana

January 2021

MULTISCALE ANALYSIS OF FLOWS PAST MARINE HYDROKINETIC DEVICES USING NUMERICAL SIMULATIONS

Abstract

by

Karina A. Soto Rivas

In this work, we seek to understand the effects that a farm of Marine Hydrokinetic (MHK) devices would have on the flow in the Chacao channel, Chile. We adopted a multi-scale approach to study the flow at the turbine scales and propose a parameterization for representing a group of turbines in the mesoscale. In Chapter II, we used the hybrid turbulence model DES coupled with the actuator disk approach to simulate staggered turbine configurations with different separations between devices and channel depths on an idealized domain. Using the time-averaged results, we obtained an expression for a new thrust coefficient representative of an entire farm of turbines, C_{tFarm}, which only depends on the lateral and longitudinal separation of the devices and the number of rows of turbines. In Chapter III, we incorporated C_{tFarm} into the ocean circulation model FVCOM, representing a specific finite farm of turbines in the Chacao channel. Firstly, we simulated a base case without devices to choose three suitable locations for installing a farm of turbines according to a commercial device's specifications. Then, we characterized the local bathymetry of the chosen locations to design an appropriate computational grid that considers the dominant bedforms. After simulating turbines, we observe variations in the velocity, turbulent kinetic energy (TKE), and shear bottom since these factors could affect the local ecosystem. The results showed that in flatter bathymetries, the magnitude of the percentage

change in TKE and bottom shear is higher than in complex bathymetries since the presence of turbines represents a more significant alteration of the initial conditions. On the other hand, the absolute changes show that the initial conditions in velocity and TKE dominate the momentum extraction despite the bedforms because they have more power available. In this research, we were able to take the thrust force of a specific farm of turbines using high-resolution simulations and bring it to a larger scale model with realistic tides and bathymetries, which provides more insights to predict and mitigate the possible negative impacts of an MHK farm installation.

To my parents, who always have encouraged me to follow my dreams

CONTENTS

Figures v

Tables x

Acknowledgments xi

Abbreviations xii

Chapter 1: Introduction 1
1.1 Hypothesis and Objectives 8

Chapter 2: MHK Devices Farm Parameterization 12
2.1 Introduction 12
2.2 Numerical Simulations for Representing MHK Devices 16
2.2.1 Force Distribution in the Actuator Disks 18
2.2.2 Validation of DES Coupled With Actuator Disk 24
2.3 Methodology 28
2.3.1 Thrust Coefficient for a Farm of Turbines 32
2.3.2 Setup for Numerical Simulations 33
2.4 Results and Discussion 35
2.4.1 Formulation of the Thrust Coefficient Representative for Farms of Turbines 36
2.4.2 Comparison of $\mathbf{C_{tFarm}}$ Parameterization With Previous Work 44
2.5 Summary 46

Chapter 3: MHK Devices Farm Representation in Ocean Circulation Models . 49
3.1 Introduction 49
3.2 Numerical Simulations of MHK Farms in the Chacao Channel 53
3.2.1 Incorporation of Farms of Turbines in FVCOM 56
3.3 Methodology 58
3.3.1 Choice of Farm Location 59
3.3.2 Bathymetry Characterization 64
3.3.3 Simulation Cases 71
3.4 Results 73
3.4.1 Chacao Channel Simulations Without Turbines 74

3.4.2 Chacao Channel Simulations With Farms of Turbines 79
3.5 Discussion 88
3.6 Summary 91

Chapter 4: Conclusions 95
4.1 Thesis Summary 96
4.2 Thesis Contribution 100
4.3 Future Work 100

Appendix A: Numerical Simulations of Devices in Chacao Channel Using an Improved Vertical Resolution 102

Bibliography 104

FIGURES

1.1 The Chacao channel is located in southern Chile, between the continent and the main island of Chiloé archipelago. It is characterized by high velocities produced by the narrowing of the flow between the two bodies. 8
1.2 Scheme for temporal-spatial scales of tidal motions that influence the energy generation. Colored zones show the range where this research is focused on. Blue zone shows the scales of the wakes produced by the devices. Green zone shows the scales, where farms of devices interact with tides. 10

2.1 Schematic distribution of disks for the validation of numerical simulations, following the laboratory experiments of Chamorro and Porté-Agel (2011) and Markfort et al. (2012) 19
2.2 Velocity profiles 3D downstream the 1^{st} and the 3^{rd} rows of turbines at the center span of the channel. Continuous lines are the result of simulations using different distributions of C_t' over the actuator disks. Circles indicate the measurements taken by Markfort et al. (2012). Black dashed lines indicate the bottom, center, and top of the disks. . 21
2.3 Turbulence intensity, σ_u, 3D downstream the 1^{st} and the 3^{rd} rows of turbines at the center span of the channel. Continuous lines are the result of simulations using different distributions of C_t' over the actuator disks. Circles indicate the measurements taken by Markfort et al. (2012). Black dashed lines indicate the bottom, center, and top of the disks. 22
2.4 Comparison of the Reynolds stress' component $\overline{\tilde{u}'\tilde{w}'}$ between three different distributions of C_t over the disk, and an experimental data. The measurements are at the center span for two different heights. coefficient C_t. 24
2.5 Mean streamwise velocity normalized by U_0 (the inlet velocity at the hub height, z_{hub}) as a function of Z/z_{hub}, downstream of the 1^{st}, 5^{th}, and 11^{th} rows of turbines. Circles show the measurements of Markfort et al. (2012). Continuous lines are the results of the DES simulations coupled with the actuator disk approach. Dashed lines mark the bottom, center, and top of the disks. 26

2.6 Turbulence intensity in the streamwise direction (σ_u/U_0) profile as a function of Z/z_{hub}, downstream of the 1^{st}, 5^{th}, and 11^{th} rows of turbines. Circles show the measurements of Markfort et al. (2012). Continuous lines are the results from the DES simulations coupled with the actuator disk approach. Dashed lines mark the bottom, center, and top of the disks. 27
2.7 Schematic of a representative control volume used to calculate the resultant force for an array of devices. Here L_x and L_y are the length and the width of the control volume, respectively, meanwhile the height, L_z is the same as the channel. In this example, the control volume encloses 18 devices, and comprises a volume that includes from the first to the seventh row of turbines. 30
2.8 Resultant force calculated by using control volumes that go from the first row of turbines through the last one (see Figure 2.7), per unit of mass ($\rho L_x L_y L_z$). ■ Analytic force calculated as the force of one actuator disk times the total number of devices in the farm. ♦ Analytic force calculated by using the average velocity at the location of the disks, U_d, instead of the undisturbed velocity, U_∞. • Resultant force obtained from DES numerical simulations. 31
2.9 (**a**): Variation of C_{tFarm} due to changes in the size of the farm in the spanwise direction, L_y. The ratio L_y/S_y can be interpreted as the number of columns of turbines. (**b**): Schematic of the control volumes used for calculating C_{tFarm} for two and four rows of turbines. 37
2.10 (**a**): Variation of C_{tFarm} due to changes in the size of the farm in the streamwise direction, L_x. The ratio L_x/S_x can be interpreted as the number of rows of turbines. (**b**): Schematic of the control volumes used for calculating C_{tFarm} for various numbers of rows. 38
2.11 Changes in C_{tFarm} due to the variation of: (**a**) The streamwise distance between devices, S_x/D, (**b**) the spanwise distance between devices, S_y/D, and (**c**) the ratio between the depth of the channel and the hub height, H/z_{hub}. The results are divided into two cases: farms with two rows of turbines (light blue), and farms with more than two rows (purple). Since we do not observe a significant influence of S_x/D on C_{tFarm} for farms with two rows, we perform extra simulations (marked with dashed lines), where we see C_{tFarm} remains insensitive to the distance in the streamwise direction 40
2.12 C_{tFarm}/C_t', for farms with exactly two rows of turbines, versus the disk separation in: (**a**) the streamwise direction, and (**b**) in the spanwise direction. Continuous line: Empirical solution proposed in Equation 2.9. Dots: Results from DES numerical simulations. 43
2.13 C_{tFarm}/C_t', for farms with more than two rows of turbines, versus the disks separation in: (**a**) the streamwise direction, and (**b**) in the spanwise direction. Continuous line: Empirical solution proposed in Equation 2.9. Dots: Results from DES numerical simulations. 44

3.1 Grid for the numerical simulations of the Chacao channel in FVCOM. The entire mesh surrounds the entire Chiloé island and is used to obtain the boundary conditions for the Chacao channel. Meanwhile, the zoom shows the domain we use for all the simulations, which has a higher resolution. 56
3.2 Minimum (left) and maximum (right) depth at every point through the time in the Chacao channel. Gray areas show the points where the minimum depth is under 40 m, and the maximum depth is over 85 m. Enclosed in dashed lines are the areas where the installation of MHK devices is restricted. 61
3.3 Absolute value of the time-averaged velocity at the hub height. Left: Ebb flow. Right: Flood flow. Gray areas show the points where the velocity is under 0.4 m/s and over 4 m/s. Enclosed in dashed lines are the areas where the installation of MHK devices is restricted. 62
3.4 Map of the chosen zones for simulating farms in the Chacao channel labeled as A, B, and C, colored by the bathymetry. We also show a schematic of zone C dimensions, which are the same for zones A and B. 64
3.5 Scheme of the vectors used for calculating the directional variograms of a discretized bathymetry. (i) and (ii) are schemes of the vectors with magnitude $k = k_1$, and k_2, respectively, for calculating the variogram in latitude 0^o (East direction). (iii) and (iv) schemes of the vectors with magnitude $k = k_1$, and k_2, respectively, for calculating the variogram in latitude 45^o (North-East direction). 66
3.6 Variograms of the bathymetry of the simulated cases in the Chacao channel (marked in Figure 3.4), calculated in different directions, where 0^o corresponds to the East direction, and 90^o, to the North direction. The data set used for calculating them corresponds to the high-resolution bathymetric data (10 m) 68
3.7 Discretized domain for the simulations with turbines in FVCOM for the Chacao channel, colored by the interpolated high-resolution bathymetric data. The zoom highlights the area where the turbines are simulated; there, every element has a height of 100 m and a width of 150 m. The rectangles in purple indicate the exact area of zones A, B, and C. The legend at the left corresponds to the bathymetry of the entire domain; meanwhile, the legend at the right, belongs to the bathymetry of the zoomed area. 70
3.8 Bathymetry at the center-span of the zones of cases A, B, and C. In continuous line, is the bathymetry used for the simulations. In dashed lines, is the high-resolution bathymetry taken from Guerra et al. (2017) every 10 m. The zone occupied by the farms is marked in gray. 71

3.9 Scheme of turbines distribution for cases A, B, and C, where S_x is the distance between rows, and S_y, the lateral distance between the center of the disks. Black lines show the computational grid used in FVCOM for representing the farms, which are the same purples rectangles highlighted in the zoomed area of Figure 3.7. 72
3.10 Absolute velocity in the streamwise direction, u, at the hub height, before simulating turbines in zones A, B, and C (see Figure 3.4). The profiles are located at the center span of every zone. In the streamwise direction, the profiles go from $45D$ upstream to the center of the farm location ($x/D = 0$), to $45D$ downstream. The gray areas indicate the location of the farms in the next simulations; meanwhile, the black arrows indicate the flow direction. 75
3.11 Incidence angle of velocity, at the hub height, before simulating turbines in zones A, B, and C (see Figure 3.4). The profiles are located at the center span of every zone. In the streamwise direction, the profiles go from $45D$ upstream to the center of the farm location ($x/D = 0$), to $45D$ downstream. The gray areas indicate the farms' location; meanwhile, the black arrows indicate the flow direction. 76
3.12 Modeled TKE at the top turbines height before simulating them in zones A, B, and C (see Figure 3.4). The profiles are located in the center span of every zone. In the streamwise direction, the profiles go from $45D$ upstream to the center of the farm location ($x/D = 0$) to $45D$ downstream. The gray areas indicate the location of the farms in the next simulations; meanwhile, the black arrows indicate the flow direction. 77
3.13 Bottom shear, τ_b before simulating the turbines in zones A, B, and C (see Figure 3.4). The profiles are located in the center span of every zone. In the streamwise direction, the profiles go from $45D$ upstream to the center of the farm location ($x/D = 0$) to $45D$ downstream. The gray areas indicate the location of the farms in the next simulations; meanwhile, the black arrows indicate the flow direction. 79
3.14 Slices at farm center coloured by the absolute velocity deficit in the streamwise direction, in m/s, with respect to the results of case 0. (**i**), (**ii**), (**iii**) are cases A, B, and C, respectively for the flood regime. (**iv**), (**v**), (**vi**) are cases A, B, and C, respectively for the ebb regime. White diamonds indicates the center of the farms. 81
3.15 Percentage of the absolute velocity deficit in the streamwise direction, u, at the farm center height, and farm's center span, due to the device's installation. The 100% are the results of case 0 in the same location as the other cases. The location of the farms is highlighted in gray; meanwhile, $x/D = 0$ is the center. The black arrows indicate the flow direction. 83

3.16 Percentage of modeled TKE increment at the height of the top turbines, and farm center span, due to the device's installation. The 100% are the results of case 0 in the same location as the other cases. The location of the farms is highlighted in gray; meanwhile, $x/D = 0$ is the center. The black arrows indicate the flow direction. 85
3.17 Percentage of bottom shear stress, τ_b, deficit, due to the farms installation, at the farm center span. The 100% are the results of case 0 in the same location of the other cases. The location of the farms is highlighted in gray; meanwhile, $x/D = 0$ is the center. The black arrows indicate the flow direction. 86
3.18 Percentage of modeled TKE deficit at the bottom, and farm center span, due to the farms installation. The 100% are the results of case 0 in the same location of the other cases. The location of the farms is highlighted in gray; meanwhile, $x/D = 0$ is the center. The black arrows indicate the flow direction. 87
3.19 Theoretical extractable power, P, of cases A, B, and C, in flood, and ebb regime. 88
3.20 Difference in the bottom shear, $\Delta\tau_b(m^2/s^2)$, caused by the farm installation in case A, where a positive difference implies a decrease in the bottom shear. Right figure corresponds to the flood regime, and left figure, to the ebb. Black rectangles indicate the area occupied by the turbines; meanwhile the arrows indicates the flow direction. . . . 91

A.1 Vertical velocity and TKE profiles at the center of the farm of case A in spanwise and streamwise directions. (a) and (b) are profiles for flood regime; meanwhile, (c) and (d) are profiles for the ebb regime. In purple, profiles obtained from the original simulations (i.e., using ten sigma layers). In green, profiles obtained by using 21 sigma layers in the simulations. In dashed lines, Profiles obtained from simulations without turbines and with 21 sigma layers. 103

TABLES

2.1 RSR for simulated velocity profiles downstream turbines rows using different C_t' distributions over the disks area. 23
2.2 RSR for simulated turbulent intensity profiles downstream turbines rows using different C_t' distributions over the disks area. 23
2.3 %RMSE for simulated Velocity and Turbulent intensity profiles downstream rows 1, 5 and 11 27
2.4 Summary of the simulated cases. 34
2.5 Main variables common for all the simulated cases 35
2.6 Comparison of the results of the ξ parameter proposed by Abkar and Porté-Agel (2015) with ξ calculated by using our parameterization of C_{tFarm}/C_t'. 46

3.1 Main variables for the simulated cases in FVCOM 73

ACKNOWLEDGMENTS

I am deeply grateful to my two advisors, Cristián Escauriaza and David Richter, for their belief in me, their constant support, and most importantly, for their immense patience. Many thanks to my coworkers and friends from Notre Dame University and the Catholic University of Chile for sharing their experiences with me, giving me feedback and advice that made this challenge easier. I also want to thank the funding of CONICYT-PCHA/Doctorado Nacional/2016-21160137 and the Marine Energy Research & Innovation Center (MERIC) project, CORFO 14CEI2-28228; this work hadn't been possible without them. I'm very grateful for my friends' emotional support, especially Sebastian, who encouraged me to go to Notre Dame. Finally, I want to thank my family, my dad, mom, and sister, which are the people who have believed in me the most, even more than myself. I love you.

ABBREVIATIONS

ADM:	Actuator Disk Model
BEM:	Blade Element Momentum
DES:	Detached-Eddy Simulations
LES:	Large-Eddy Simulations
MHK:	Marine Hydrokinetic
OCM:	Ocean Circulation Models
RANS:	Reynolds-averaged Navier-Stokes
RMSE:	Root Mean Square Error
RSR:	RMSE-observation Standard Deviation Ratio
TKE:	Turbulent kinetic energy

CHAPTER 1

INTRODUCTION

The extraction of kinetic energy from tidal currents using marine hydrokinetic (MHK) devices can contribute to solve problems associated with the increase of global energy demand and greenhouse gas emissions (IEA and World Bank, 2015). Tidal energy is characterized by being predictable, CO_2 emission-free in operation, and minimal visual impact. Plenty of studies have shown a considerable amount of extractable power from tides available around the world (Hagerman et al., 2006; Robins et al., 2015; Tarbotton and Larson, 2006). However, there are just a handful of marine energy projects in construction or testing. Nevertheless, even though harnessing energy from the tides could potentially be a positive contribution to the energy supply, the impacts on the tidal flow itself in the marine environment are yet unclear. For this reason, it is essential to first analyze and assess the hydrodynamic effects before any installation to understand the changes in the physical environment.

The harnessing of tidal energy from the Chacao channel located in southern Chile (see Figure 1.1) between Chiloé Island and Puerto Montt city has become an interesting option for the energy supply of its surrounding area. Currently, almost the 60% of the energy sources in Chiloé Island are non-renewable (CNE, Chile, 2020); however, the Chilean government is planning to reach at least a 70% of renewable sources of energy in the country by the year 2050. The Chacao channel has favorable conditions due to the flow narrowing between the continent and the large Chiloé island that allows currents that can exceed 4 m/s (Guerra et al., 2017). Additionally, a research based on the distance to the electric grid, available resources, channel depth, and

possible conflicts with the fishery industry has shown that this channel is one of the best places in the area for installing MHK devices (Cruz et al., 2009). Nevertheless, those above are not enough to affirm that an MHK farm would positively contribute to the Chacao channel since it is necessary to study the flow in the area and predict the changes provoked by a marine devices' installation before.

The studies to characterize the flow past MHK turbines require a thorough understanding of the flow physics. For this, numerical simulations offer an option to recognize and characterize the interactions between the flow, the turbines, and the environment at different ranges. Their advantage is they can provide information over an entire discretized domain through time. For the oceanic physical processes, some models can represent the different temporal and spatial scales involved, which are shown in Figure 1.2; however, it is impossible to use just one numerical simulation to cover all scales because of the computational cost restrictions. For example, the interaction between a realistic flow and turbine farms can be represented by using ocean circulation models (from now referred to as OCM) because they can incorporate the tides and can encompass a length of the coastline's order of magnitude (located at the green zone in Figure 1.2). Nevertheless, the resolution of those models does not allow the representation of every single device, so a parameterization for a group of them is needed to consider the effects of the turbines' distribution at larger scales. On the other hand, high-resolution models cover smaller scales that can simulate the highly turbulent zone located downstream of the turbines caused by the disturbance of the flow, also known as wakes (see blue zone in Figure 1.2). At that scale, we can observe how the wake downstream of every device interacts with the other turbines' wakes, so those high-resolution models are useful for studying the physical processes inside a farm and up-scaling their effects.

At the wakes' scale (blue zone in Figure 1.2), there are several options for simulating the flow and representing the turbines. On the one hand, the most straightforward

approach for the flow solver is using the Reynolds-Averaged Navier-Stokes (RANS) equations since they solve the mean velocity field; meanwhile, they use a turbulence model for the averaged fluctuations. Models with RANS have the advantage of being less computationally expensive than other models; however, RANS cannot accurately predict the unsteadiness of the separated flow (Breuer et al., 2003), which is relevant in the representation of shear layers such as the ones produced between the flow and the turbines. More sophisticated models use Large-Eddy simulations (LES) that use a filter where the structures up to the grid size are explicitly calculated, which means that LES solves the large-scale unsteady motions. However, this model needs a higher resolution than RANS close to the walls, so LES is more computationally expensive (Pope, 2000). An intermediate approach is the hybrid turbulence model called Detached-Eddy Simulations (DES) (Escauriaza and Sotiropoulos, 2010, 2011a,b; Gajardo et al., 2019; Soto-Rivas et al., 2019; Spalart and Allmaras, 1992), which combines the advantages of RANS and LES. Near the walls, DES uses RANS, which avoids the very high-resolution that LES would use there. Meanwhile, far from the walls (i.e., in the main flow), DES uses LES that can solve, for example, the main vortexes downstream of the MHK devices. This way, DES has a balance between precision and affordability.

The options to represent the MHK devices go from increasing the bottom drag as Kramer and Piggott (2016) to represent the turbines' whole geometry as Daskiran et al. (2015); Kang et al. (2012, 2014); Riglin et al. (2015, 2016); Schleicher et al. (2015). An intermediate level of complexity is the momentum sink approach, which consists of incorporating an equivalent force to the conservation of momentum equations. This methodology is used in the Actuator Disk Model (ADM) (Burton et al., 2011; Ramos et al., 2019), where the turbines are simplified as a static disk with the same radio as the devices. In the ADM, the force depends on the disk area and the velocity and density of the flow. Other uses of the momentum sink approach, are the

Blade Element Momentum (BEM) (Creech et al., 2015; Gajardo et al., 2019; Schluntz and Willden, 2015), and the Actuator Lines Model (ALM) (Marjanovic et al., 2017; Ouro and Stoesser, 2017; Ouro et al., 2019; Sørensen and Shen, 2002; Stevens et al., 2018). On the one hand, BEM is similar to the ADM, but it incorporates the turbine rotation and the blades' features to compute the resultant force. Meanwhile, ALM is more sophisticated since it distributes the resultant force along rotating lines representing each turbine blade.

At the tides scale (green zone in Figure 1.2), it is possible to incorporate the momentum sink approach in OCM for simulating multiple devices. For this, it is necessary to add to the momentum conservation equation the thrust force applied by the total of the devices in the grid element. In the literature, we can see how this approach has been used to predict the effect of MHK devices in real marine channels, as in the works of Fallon et al. (2014); Nash et al. (2014); Wang and Yang (2017); Yang et al. (2014); however, the changes in the resistant force caused by different turbines distribution are not considered. This problem can be solved by representing just one turbine per grid cell, in which the grid resolution restricts their distribution. It is essential to consider those above because depending on the distance between the turbines and their distribution, the flow velocity can change in direction and magnitude, which allows some configurations to be more efficient than others (Myers and Bahaj, 2012; Riglin et al., 2016). As we can see, numerous works use OCM to represent MHK devices in real marine environments; however, almost all of them consider an unrealistic number of turbines that exceed hundreds and even thousands of units (Dominicis et al., 2017; Garcia-Oliva et al., 2017; Yang et al., 2013). Another limitation in the representation of marine turbines in OCM is the lack of field measurement data for validating their performance. Nevertheless, some works use OCM to replicate laboratory conditions with MHK devices that have shown a good agreement between simulated and measured data (Roc et al., 2013;

Thiébot et al., 2016).

The up-scaling of MHK devices is similar to that for wind energy turbines because the flow solver of both calculates the mass and momentum conservation equations; meanwhile, for the representation of the turbines, we can use the same approaches. We have to clarify that it is not always possible to use the same models for wind and marine energies because this depends on the simulation's considerations, such as marine surface interaction and salinity, among others. The reason for considering wind energy research is because there are more studies and field measurements for validating the simulations. For example, Fitch et al. (2012) proposed a parameterization for representing a farm of wind turbines in a mesoscale atmospheric model that showed good agreement with available measurements; however, they still did not include the interactions for different turbines configurations. Later, Abkar and Porté-Agel (2015) improved the parameterization of Fitch et al. (2012) by calculating a correction factor, from Large Eddy Simulations (LES), that changes with the lateral separation between the turbines; still, they did not give a parameterization for calculating the correction factor for other configurations. Besides, in their work, Abkar and Porté-Agel (2015) used a domain with periodic boundaries, which means that their results are just valid for fully developed flow. Despite this, the use of MHK devices is an incipient technology, and even the largest farms installed in the world do not exceed five turbines; therefore, for the representation of a tidal energy farm in an OCM, it is essential to comprehend how the devices interact in a finite domain. An example of a parameterization for a finite wind farm is the work of Vanderwende et al. (2016), which uses the momentum sink approach into a mesoscale model. The results of Vanderwende et al. (2016) show good agreement with previously validated LES simulations; however, they just studied one configuration of turbines, so they did not provide information about how the device's distribution could affect the flow at larger scales models.

One of the objectives of up-scaling a specific farm's effects into an OCM is to represent them accurately and study their interaction with the natural environment's characteristics, such as realistic bathymetries. Currently, some works represent MHK devices to describe how bedforms affect their performance. Some of those studies are the work of Peebles and Johnson (2015), which performed numerical simulations of around 100 devices in an idealized flow over simplified bathymetries, where it was shown that lateral bottom sloping (less than 12^o) does not have a significant effect on the performance of farms. Meanwhile, longitudinal sloping (around 5^o) can significantly improve the array's performance increasing the farm's net thrust force around 200%. Those above are because the increment of the longitudinal bottom's slope increments the streamwise velocity due to the decrease in the cross-sectional area. Regarding experimental works, there are studies of mobile bedforms that highlighted the importance of considering the complex topographies in MHK devices (Hill et al., 2016; Musa et al., 2018, 2019). In particular, the work of Hill et al. (2016) shows that bedforms located in the near-field upstream the devices increase their mean voltage. The aforementioned occurs because larger bedforms allow the flow to accelerate, increasing the turbulent kinetic energy (TKE) at the turbines' height. However, in the experiments of Hill et al. (2016), they use a ratio between the height of the dunes and the turbines' diameter around 0.3 and 0.5, which is very high in comparison with real conditions.

As we show, plenty of studies analyze the interactions between MHK devices with flow and bedforms; however, many of them can be improved by incorporating more realistic conditions. For example, the simulations of MHK devices at a large scale should consider the distribution of the devices for calculating the resultant force of a specific farm. Another example is to simulate finite farms since most of the existing research considers too many devices, which is impossible due to the current technologies and resources in the marine energy field. Finally, the studies of

the bathymetries' impacts over the farms and the wakes downstream should point towards representing complex bathymetries with realistic bedform sizes.

To improve the study of the representation of MHK farms in OCM and their interaction with the flow and the local bathymetry, we divided our work into the next two chapters:

- In Chapter II, we look for improving the momentum sink approach for representing finite farms of MHK turbines to incorporate the different interactions between the devices according to their distribution. We also look to incorporate the effect of the farm's depth, which is one of the main differences between the representation of marine and wind turbines. For this, we simulate the flow around individual devices by using the DES approach, coupled with the actuator disk approach. We calculate a dimensionless thrust coefficient for an entire finite farm of turbines from this high-resolution model, C_{tFarm}, to represent the sink of momentum at larger scales. We make a systematic study to understand how this coefficient is affected by changes in the mean flow and the turbine's distribution.
- In Chapter III, we introduce the new parameterization into the ocean circulation model FVCOM (Finite-Volume Coastal Ocean Model) (Chen et al., 2003) to represent a finite farm of turbines at larger spatial and temporal scales. We simulate a farm in different locations within the channel, considering the tides and bathymetry of the Chacao channel. With the simulation results, we study the turbines' effects on the mean flow, depending on their location.

The approach we propose can contribute to understanding the interactions between the turbines and the environment and among the turbines themselves. This analysis provides a consistent approach to connect two separated scales at which MHK devices operate. We test the results of the parameterization of finite turbine farms in the large-scale ocean model to evaluate the potential impacts such as the extension of the local changes on the mean flow, bed stresses, and turbulent kinetic energy produced by the turbine wakes. We hope that with this information, it will be possible to improve the selection of a suitable location for the farms and to take mitigation measures to minimize the negative impacts.

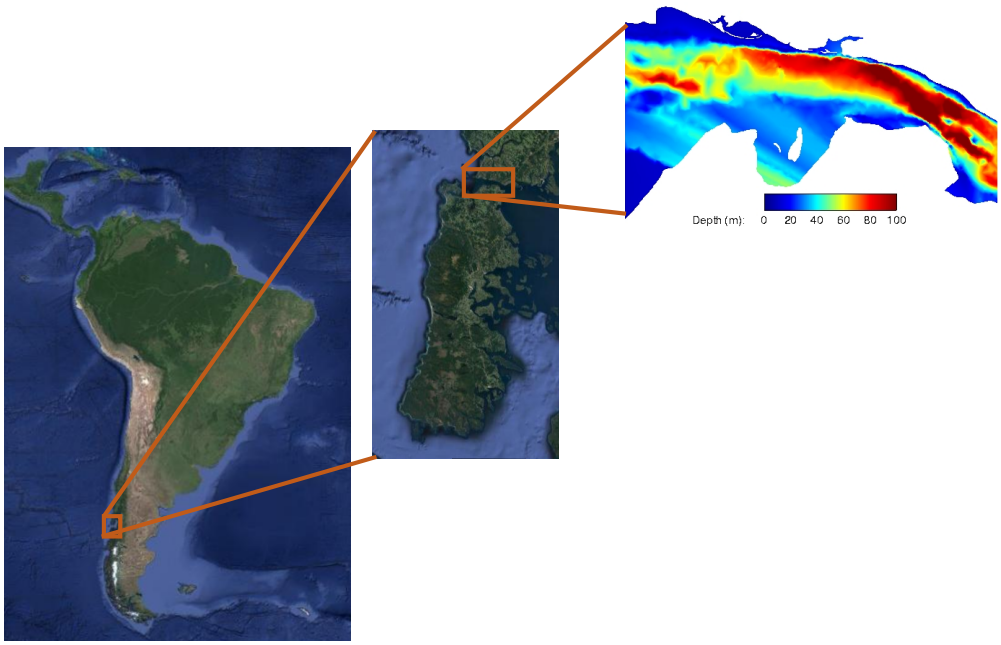

Figure 1.1. The Chacao channel is located in southern Chile, between the continent and the main island of Chiloé archipelago. It is characterized by high velocities produced by the narrowing of the flow between the two bodies.

1.1 Hypothesis and Objectives

The main goal of this work is to represent finite farms of MHK turbines in the Chacao channel to describe the interaction between the flow, the devices, and the local bathymetry. The challenges of this research are to represent the dominant physical variables at two different scales, using appropriate numerical models to simulate the flow, and choosing the best approaches to representing the turbines at larger scales where the details cannot be resolved. The study of the simulated data has to result in a new parameterization capable of representing the local effects of farms of turbines in ocean circulation models to extend the simulation scope and reduce computational

costs. The hypothesis of this work is:

"By adopting a multiscale approach, we can use a high-resolution model to derive a parameterization for marine hydrokinetic (MHK) devices, and represent farms of turbines with realistic tides and bathymetry in ocean circulation models (OCM)."

For proving the hypothesis, we are looking for achieving the specific objectives listed below:

E.O. 1: Develop advanced numerical simulations at different spatial and temporal scales of tidal streams, considering the installation of multiple turbines to evaluate the impacts on flow resistance and the local environment.

E.O. 2: Establish a solid and consistent framework to represent farm of turbines over real bathymetries, parameterizing MHK device's interaction, and up-scaling the effects of the turbines on larger-scale, tide-resolving models.

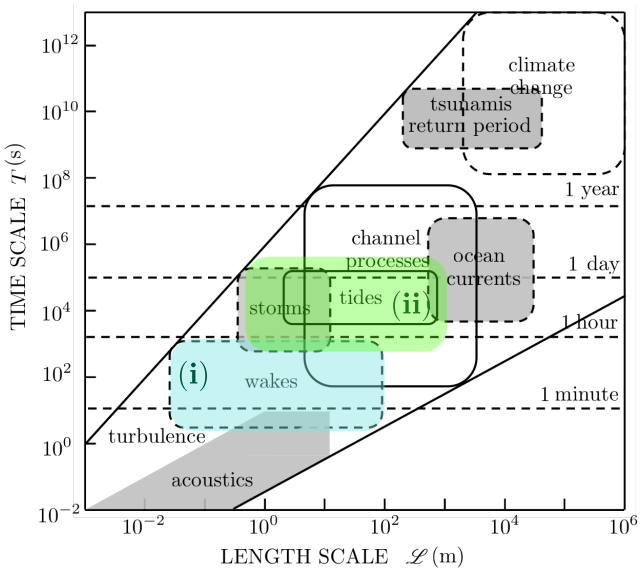

Figure 1.2. Scheme for temporal-spatial scales of tidal motions that influence the energy generation. Colored zones show the range where this research is focused on. Blue zone shows the scales of the wakes produced by the devices. Green zone shows the scales, where farms of devices interact with tides.

This work is organized as follows: In Chapter II, we seek a new parameterization for a thrust coefficient representing an entire farm of turbines in OCM, which we call C_{tFarm}. For that, we present and validate the DES model coupled with the actuator disk approach. After that, we make a dimensional analysis to recognize the variables that dominate the new parameter, C_{tFarm}. Finally, we use the DES model with actuator disk to represent different turbines configuration and study how C_{tFarm} changes with the turbines' distribution. In Chapter III, we incorporate the new parameterization into the ocean circulation model, FVCOM, to represent farms of turbines in the Chacao channel. There, we run a base case without turbines to know the undisturbed conditions and choose the best three locations for turbines based on the device's velocity and depth. After that, we characterize the local bathymetry of

the three cases to observe the differences between them and design an appropriate grid resolution. Finally, we observe the turbines' effects on the mean flow inside and downstream the farms according to their location.

CHAPTER 2

MHK DEVICES FARM PARAMETERIZATION

2.1 Introduction

Three-dimensional numerical simulations can represent the flow around marine hydrokinetic (MHK) turbines, providing detailed information about the physics among different scales of space and time. By using computational models, it is possible to study the effects of the devices in the mean flow and the interaction among the turbines' wakes in an arrangement. There are different options for the flow solver and the turbine representation approach that differs in the level of complexity and use of computational resources.

At the scale of the turbines, the alternatives for the flow solver go from solving the Reynolds-average Navier-Stokes equations (RANS), which demands less computational resources, but does not have good performance over obstacles (Pope, 2000). Then, we have the Large Eddy Simulations (LES) that solve the turbulent structures that are equal or larger than the grid size; however, this model can increment the computational costs excessively depending on the resolution. On the other hand, the approaches for representing the devices go from the most straightforward option, which enhances the drag at the bottom (Kramer and Piggott, 2016). There is the momentum sink approach in an intermediate level that consists of applying an equivalent thrust force in the momentum conservation equations (Abkar and Porté-Agel, 2015; Calaf et al., 2010; Porté-Agel et al., 2011). Most sophisticated alternatives represent the entire turbine's geometry and even its rotation (Daskiran et al., 2015;

Kang et al., 2012, 2014; Riglin et al., 2015, 2016; Schleicher et al., 2015); nonetheless, due to the high computational resources they need, they can only simulate a couple of devices (e.g., only one in the work of Kang et al. (2014), and up to four in the work of Riglin et al. (2016)).

To represent farms of turbines at larger scales, such as tidal channels, we need to use ocean circulation models (OCM). When using an OCM, it is not possible to represent every device because the resolution is larger than a group of devices; otherwise, the computational cost would highly increase. For that reason, to represent farms of MHK devices in OCM, it is necessary to use a parameterization. One option is to incorporate a sink of momentum in the momentum conservation equation, which is equal to the thrust force applied by a single turbine, multiplied by the number of devices in the grid element. Examples of works where this technique is applied in tidal channels are Nash et al. (2014); Wang and Yang (2017); Yang et al. (2014). However, in those works, the resistance force's changes due to the distribution of the turbines inside the farm are not considered. Recently, Piano et al. (2018) demonstrated that neglecting the interaction between devices is a reasonable approximation for up-scaling the effect of farms with less than 25 turbines into two-dimensional vertically-averaged ocean models. Nevertheless, we cannot assume the same for three-dimensional OCM, especially for flows with substantial vertical velocity components. Another option for incorporating the effect of turbines into large scale models is to represent just one device per grid cell. In this case, the distribution of the devices will be restricted by the grid resolution, which can represent a problem because depending on the inter-turbine spacing, the flow's velocity can change in magnitude and direction (Myers and Bahaj, 2012; Riglin et al., 2016).

Some studies have presented parameterizations for farms of MHK devices. One example is the work of Nishino and Willden (2012), who proposed the idea of a global thrust coefficient representative of an entire farm. In their work, Nishino and Willden

(2012) calculated the efficiency of a group of turbines based on the local and global blockage areas, which are defined as the ratio between the area of the devices over the farm area, and the entire domain area, respectively. Nonetheless, the analytical formulation they proposed is only valid for very large farms. Stansby and Stallard (2016) carried out another study of farms parameterization, in which they represented and optimized arrangements of tidal turbines, by proposing a correction factor to the blockage area that considers the velocity deficit and the turbines upstream of every row. Although the results of Stansby and Stallard (2016) have shown good agreement with experimental cases, they did not provide a formula that could be extended for other arrays.

Since many of the physical processes observed in the flow past MHK devices are similar to conditions in wind turbines, we can refer to the literature related to wind energy, where there is a wider variety of numerical simulations. Fitch et al. (2012), for example, proposed and validated a parameterization scheme for a group of wind turbines on a mesoscale atmospheric model. However, their representation does not consider the spatial distribution of the devices, and the limitations of the model concerning the separation distance are unclear since they did not study cases where the wakes of the devices have a strong interaction due to their proximity. Later, Abkar and Porté-Agel (2015) improved the parameterization of Fitch et al. (2012) by using LES to incorporate the effects of the distribution of turbines on the flow. They assumed periodic boundaries, following a common approach in wind turbine simulations (e.g., Calaf et al. (2010, 2011); Porté-Agel et al. (2014a)), since wind farms are often sufficiently large to allow the flow to reach a fully developed state inside the arrangement. In contrast, the largest MHK farm installed in the world does not exceed five turbines, and an accurate representation of tidal energy farms in larger-scale models requires improving our understanding of the interaction of devices on finite domains.

Additional differences arise when comparing wind turbine farms and MHK arrays, such as the vertical position of the devices within the turbulent boundary layer. In wind farms, the atmospheric boundary layer thickness is around 1000 m, and the wakes downstream of the devices are not confined from above. In the case of tidal energy, the free-surface of the flow represents a boundary that restricts the development of a symmetrical Gaussian wake and affects the velocity recovery (Aghsaee and Markfort, 2018). In some cases, turbines are close to the interface, generating disturbances of the free-surface that considerably decreases the devices' performance (Kolekar and Banerjee, 2015) especially in critical flows (Riglin et al., 2015). Thus, MHK turbines must take into account the depth of the devices and their lateral separation.

To study the effects of varying MHK farm configurations, we perform a systematic study using high-resolution numerical simulations to represent different arrangements of turbines. To simulate the flow around the devices, we utilize the hybrid Detached-Eddy Simulations (DES) turbulence model (Escauriaza and Sotiropoulos, 2010, 2011a,b; Gajardo et al., 2019; Spalart and Allmaras, 1992), which is a hybrid turbulence model that works as RANS and LES. Meanwhile, the MHK devices are represented by the actuator disk approach Burton et al. (2011), where a sink of momentum is incorporated at the area occupied by each turbine. We calculate the momentum sink of farms with different distributions and number of devices and depths from these simulations. Finally, we introduce a new dimensionless thrust coefficient, C_{tFarm}, which is meant to represent the entire group of turbines. With the use of C_{tFarm}, we seek to improve the representation of turbine arrays in ocean circulation models by incorporating the interactions among devices, according to the farm's geometric characteristics. The improved representation can be used to study the interaction between entire farms of turbines and a real environment by running larger-scale numerical simulations that use data of bathymetry and tidal cycles. Results indicate that for staggered farms C_{tFarm} only depends on the lateral separation

of the devices for farms with two rows and the lateral and longitudinal separation for farms with more rows. In addition, we show that this parameter is independent of the number of columns of devices, as well as the ratio of the depth over the hub height (up to a value of 3.3).

The chapter is organized as follows: In section 2.2, we describe the numerical method for the flow and the turbines' representation approach; besides, we validate our model with experimental results. In section 2.3, we propose the thrust coefficient, C_{tFarm}, for representing an entire farm of turbines, where we propose the variables that would dominate the parameter; further, we present the setup for the numerical simulations. In section 2.4, we formulate the representation of C_{tFarm} by performing an analysis of the flow resistance induced by an array. Finally, in Section 2.5, we summarize the findings of this investigation and highlight their importance for the next chapter.

2.2 Numerical Simulations for Representing MHK Devices

To represent the flow, we employ the DES approach, which is a hybrid one-equation turbulence model that works as a Reynolds averaged Navier-Stokes (RANS) model near the solid boundaries and as LES away from them. The advantage of DES is that it can resolve the large-scale dynamics of turbulence formed in the wakes of the disks by using the LES approach at high Reynolds numbers, while the computational costs are reduced by modeling the turbulent boundary layer with a RANS approach. The governing equations used in DES are the incompressible three-dimensional Reynolds-averaged Navier-Stokes equations for mass and momentum conservation. The non-dimensional equations are written as follows:

$$\frac{\partial \tilde{u}_i}{\partial \tilde{x}_i} = 0 \tag{2.1}$$

$$\frac{\partial \tilde{u}_i}{\partial \tilde{t}} + \tilde{u_j}\frac{\partial \tilde{u}_i}{\partial \tilde{x_j}} = -\frac{\partial \tilde{p}}{\partial \tilde{x_i}} + \frac{1}{Re}\frac{\partial^2 \tilde{u}_i}{\partial \tilde{x_j}\partial \tilde{x_j}} - \frac{\partial}{\partial \tilde{x_j}}\overline{\tilde{u_i'}\tilde{u_j'}} + \tilde{f}_t, \tag{2.2}$$

where the tilde (˜) indicates the parameters are dimensionless. In the equation 2.2, $\tilde{x_i}$ are the Cartesian coordinates ($i = 1, 2, 3$) in the streamwise, spanwise, and vertical directions respectively, $\tilde{u_i}$ is the velocity of the fluid in the direction i, $\tilde{p}$ is the pressure, Re is the Reynolds number based on the length scale, $\mathcal{L}$, and a velocity scale, $\mathcal{U}$, and $\tilde{f}_t$ is the non-dimensional thrust force per unit mass exerted by the turbines. The Reynolds stresses $\overline{\tilde{u_i'}\tilde{u_j'}}$ (where the overline denotes temporal average) are modeled by using the Spalart-Allmaras (S-A) turbulence closure, which implements a single transport equation for a term related to the turbulent viscosity, ν_t, (Spalart and Allmaras, 1992). The turbulent destruction term in this equation is scaled with the distance to the nearest wall, while far from solid boundaries is scaled with the grid size, becoming a subgrid-scale model for LES in regions away from the wall, when the production balances the destruction term.

Since it has been shown that the inlet turbulence intensity is important for accurately simulating turbines (Blackmore et al., 2014; Lloyd et al., 2014), we incorporate into our model an inlet random flow generator, using the formulation proposed in Smirnov et al. (2001). This is a stochastic approach, where the inlet averaged velocity and fluctuations in time, $\overline{\tilde{u_i'}\tilde{u_i'}}$, can easily be set by using experimental data. We have to highlight that we need two inputs for this model; one is a fully developed vertical profile of the streamwise velocity. The second input is a constant value for the components $\overline{\tilde{u_i'}\tilde{u_i'}}$.

To represent the MHK devices, we use the Actuator Disk Model (ADM), where the thrust force per unit mass, per unit of volume, $f_t = F_t/(\rho\Delta\forall)$ is incorporated in

the stream-flow direction ($\tilde{x_1}$), where:

$$F_t = \frac{1}{2}\rho U_\infty^2 A_d C_t \tag{2.3}$$

In Equation 2.3, A_d is the disk area, C_t is the thrust coefficient of a single turbine, $\Delta\forall$ is the differential volume occupied by the turbine in the discretized domain, and U_∞ is the streamwise undisturbed velocity magnitude upstream of the disk.

In a turbine farm using this common parameterization, it is not always clear what velocity scale can be used to replace the undisturbed velocity, U_∞. For that reason, a second parameterization can be defined based on the the local velocity at the disk, U_d, instead of using U_∞ to calculate the force exerted by the device. To implement this, we use a modified thrust coefficient, C_t', which is related to C_t as follows:

$$C_t' = \frac{C_t}{(1-a)^2} \tag{2.4}$$

where a is a so-called induction factor (Burton et al., 2011). In this way, we calculate the thrust force by using the following expression, which is equivalent to Equation 2.3, but it is now based on the local flow velocity seen by the disk:

$$F_t = \frac{1}{2}\rho U_d^2 A_d C_t' \tag{2.5}$$

2.2.1 Force Distribution in the Actuator Disks

For representing the turbines, there are different ways to distribute the C_t', and subsequently, the force along the disks; for that we test three different distributions to choose the best one. In the first case, a $C_t' = 0.85$ is uniformly distributed; meanwhile, in the other two cases, C_t' is distributed using a Gaussian function with an average $C_t' = 0.85$, and two different standard deviation: $\sigma = \frac{D}{2}$, and $\sigma = \frac{D}{4}$, where D is the disk diameter. The experiments are based in the laboratory experiments of Chamorro

and Porté-Agel (2011), and later, by Markfort et al. (2012), which are the same we use in the next section for validating our code.

The experimental configuration consists of 30 scaled turbines distributed in a staggered way along a wind tunnel; this is shown in the schematic of Figure 2.1. In the experiments, the velocity and turbulence up- and downstream of the turbines were measured by using a hot-wire anemometer. In the wind tunnel, the Reynolds number based on the freestream velocity at the hub height, $Re_{z_{hub}} = U_0 z_{hub}/\nu$, was equal to $36,000$. In our simulations, we use the same averaged inlet velocity and turbulence intensity profiles as measured in the wind tunnel. Regarding the lateral walls, we used symmetric boundary condition. We have to mention that the computational domain is discretized using 7.3 million nodes, which allows each disk to contain at least seven grid points in the vertical direction and five in the spanwise direction, as suggested in the literature (Wu and Porté-Agel, 2013).

In this section, we only simulate the first six rows in order to save computational resources. However, for the validation (Section 2.2.2) we simulate all the 30 devices

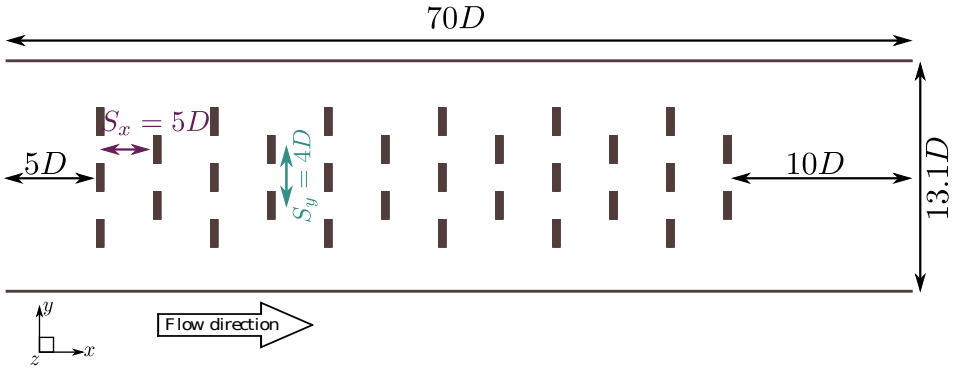

Figure 2.1. Schematic distribution of disks for the validation of numerical simulations, following the laboratory experiments of Chamorro and Porté-Agel (2011) and Markfort et al. (2012)

To make a quantitative comparison between the results of our simulations and the experimental data, we utilize the RMSE-observation standard deviation ratio (RSR) (Moriasi et al., 2007) which is defined for any variable θ as:

$$RSR = \frac{\sqrt{\sum_{i=1}^{i=n} \left(\theta_i^{obs} - \theta_i^{sim}\right)^2}}{\sqrt{\sum_{i=1}^{i=n} \left(\theta_i^{obs} - \theta_i^{mean}\right)^2}}, \tag{2.6}$$

where n is the total number of records, θ_i^{obs} are the observed data, θ_i^{sim} are the simulated results in the same location that observed data, and θ_i^{mean} is the average of the observed values. The RSR fluctuates from zero for optimal conditions, to a large positive value.

Knowing the meaning of RSR, we can interpret the comparison between the simulation and the laboratory measurement. For example, Table 2.1 shows that the RSR of the velocity profiles for the Gaussian distribution with $\sigma = \frac{D}{4}$ is the smallest, which indicates that it adjusts better to the measurements. This is corroborated by the differences between the profiles in Figure 2.2.

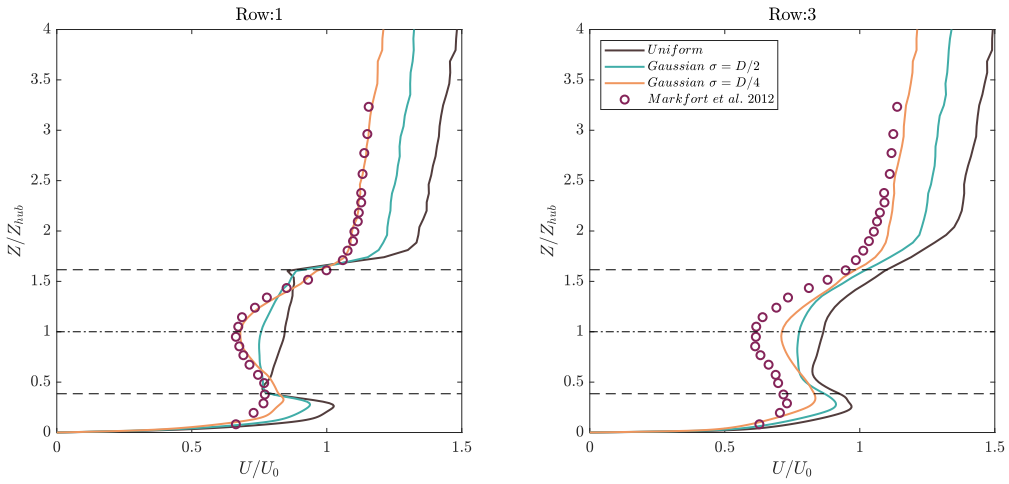

Figure 2.2. Velocity profiles 3D downstream the 1^{st} and the 3^{rd} rows of turbines at the center span of the channel. Continuous lines are the result of simulations using different distributions of C_t' over the actuator disks. Circles indicate the measurements taken by Markfort et al. (2012). Black dashed lines indicate the bottom, center, and top of the disks.

Regarding the turbulence intensity, Table 2.2 shows all the distributions have the same RSR downstream the 1^{st} row; however, in Figure 2.3 we see that the Gaussian distribution with $\sigma = \frac{D}{4}$ does not capture the peak of turbulence intensity at the top of the turbines, as the other two cases do. The figure also shows that downstream the 3^{rd} the uniform distribution with the Gaussian with $\sigma = \frac{D}{2}$, have a better performance than the other case.

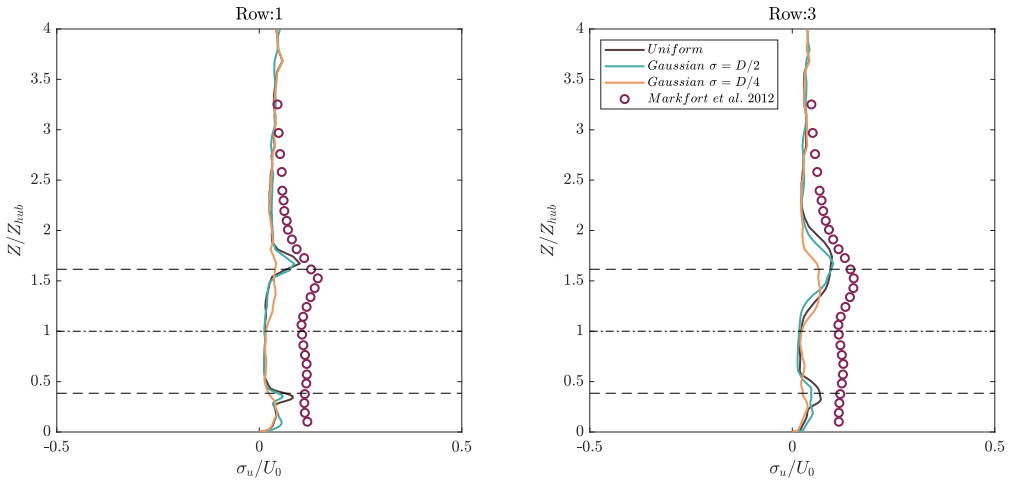

Figure 2.3. Turbulence intensity, σ_u, 3D downstream the 1^{st} and the 3^{rd} rows of turbines at the center span of the channel. Continuous lines are the result of simulations using different distributions of C_t' over the actuator disks. Circles indicate the measurements taken by Markfort et al. (2012). Black dashed lines indicate the bottom, center, and top of the disks.

TABLE 2.1

RSR FOR SIMULATED VELOCITY PROFILES DOWNSTREAM TURBINES ROWS USING DIFFERENT C_t' DISTRIBUTIONS OVER THE DISKS AREA.

Row	Uniform distribution	Gaussian distribution $\sigma = \frac{D}{2}$	Gaussian distribution $\sigma = \frac{D}{4}$
1^{st}	0.50	0.33	0.15
3^{rd}	0.45	0.44	0.26

TABLE 2.2

RSR FOR SIMULATED TURBULENT INTENSITY PROFILES DOWNSTREAM TURBINES ROWS USING DIFFERENT C_t' DISTRIBUTIONS OVER THE DISKS AREA.

Row	Uniform distribution	Gaussian distribution $\sigma = \frac{D}{2}$	Gaussian distribution $\sigma = \frac{D}{4}$
1^{st}	2.56	2.56	2.56
3^{rd}	1.81	2.10	2.25

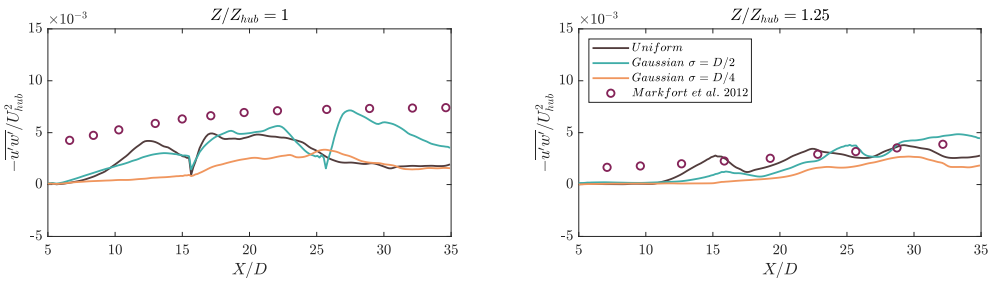

Figure 2.4. Comparison of the Reynolds stress' component $\overline{\tilde{u}'\tilde{w}'}$ between three different distributions of C_t over the disk, and an experimental data. The measurements are at the center span for two different heights. coefficient C_t.

We also observe the kinematic shear stress at the center span of the channel, $\overline{\tilde{u}'\tilde{w}'}$. Figure 2.4 shows the stress along with the flow-stream direction at two different heights. The figure depicts that the cases with uniform, and Gaussian distribution with $\sigma = \frac{D}{2}$, have a better agreement to the measurements. On the other hand, the case with Gaussian distribution and $\sigma = \frac{D}{4}$ under-predicts the kinematic shear stress, which is expected since this variable is directly related to the wake expansion. Using a value of $\sigma = \frac{D}{4}$, the force is more localized at the disk center, which produces a smaller wake than the other two distribution.

Finally, for representing a disk, a Gaussian distribution seems more suitable than a uniform one. The Gaussian distribution with $\sigma = \frac{D}{2}$ case shows good agreement with the velocity and the kinematic shear stress measurements, hence, all the simulations in this work use this distribution for representing the actuator disks.

2.2.2 Validation of DES Coupled With Actuator Disk

For validating the DES coupled with the actuator disk approach, we use the laboratory experiments of Chamorro and Porté-Agel (2011), and later, by Markfort et al. (2012), same as in Section 2.2.1. However, in this case, we simulate all the

devices with the distribution presented in Figure 2.1.

After running the numerical simulations, we calculate the time-averaged velocity and turbulence intensity profiles in the streamwise direction $\left(\sigma/U_0 = \sqrt{\overline{u_i' u_i'}}/U_0\right)$ to compare them with measurements of Markfort et al. (2012) taken three diameters downstream the 1^{st}, 5^{th}, and 11^{th} rows of turbines. On the one hand, the mean velocity profiles show good agreement with the measured data (see Figure 2.5), and for all the cases, the calculated RSR does not exceed 0.35 (see Table 2.3). The turbulence intensity profiles exhibit more disagreement, particularly downstream of the first row of turbines. Downstream of the 5^{th} and the 11^{th} rows, however, our model performs better (see Figure 2.6), with an RSR close to 2 (see Table 2.3). The simulations capture the vertical distribution, resolving almost the entire measured turbulence intensity. It is important to note that the measurements report the total turbulent intensity, whereas the computed values correspond only to the resolved component since the Spalart-Allmaras model cannot readily yield the modeled component of the normal stresses. The influence of the turbine geometry produces the largest differences in the turbulence of the wake for the first row compared to the disk simplification, and the results for this statistic improve considerably downstream, as shown in Figure 2.6.

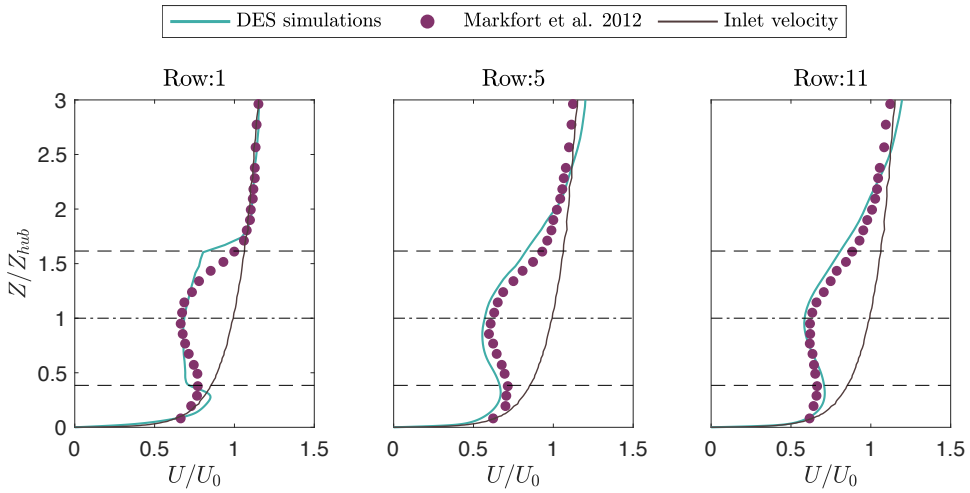

Figure 2.5. Mean streamwise velocity normalized by U_0 (the inlet velocity at the hub height, z_{hub}) as a function of Z/z_{hub}, downstream of the 1^{st}, 5^{th}, and 11^{th} rows of turbines. Circles show the measurements of Markfort et al. (2012). Continuous lines are the results of the DES simulations coupled with the actuator disk approach. Dashed lines mark the bottom, center, and top of the disks.

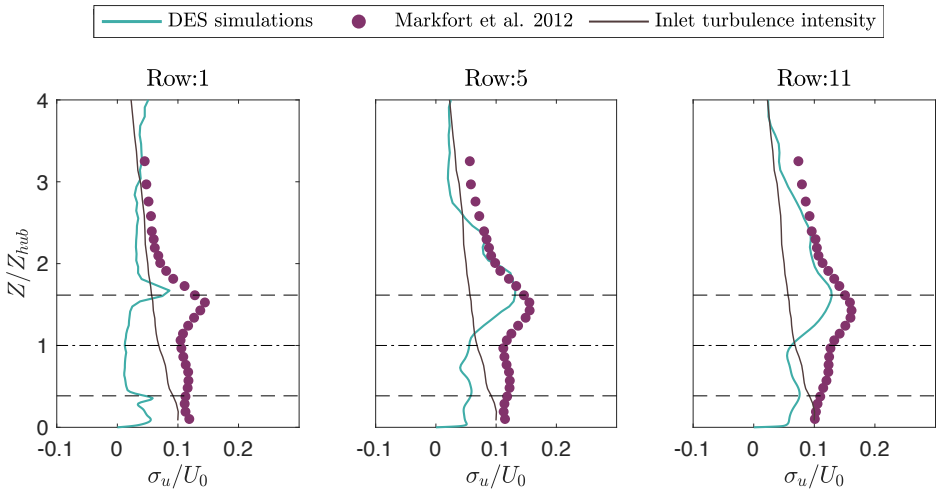

Figure 2.6. Turbulence intensity in the streamwise direction (σ_u/U_0) profile as a function of Z/z_{hub}, downstream of the 1^{st}, 5^{th}, and 11^{th} rows of turbines. Circles show the measurements of Markfort et al. (2012). Continuous lines are the results from the DES simulations coupled with the actuator disk approach. Dashed lines mark the bottom, center, and top of the disks.

TABLE 2.3

%RMSE FOR SIMULATED VELOCITY AND TURBULENT INTENSITY PROFILES DOWNSTREAM ROWS 1, 5 AND 11

Row	Velocity profile U/U_0	Turbulence Intensity $I_u = \sigma_u/U_0$
1^{st}	0.33	2.56
5^{th}	0.35	1.82
11^{th}	0.30	1.73

We acknowledge that these experiments were carried out in a wind tunnel; however, the results are equally valid for tidal applications. The last is true, because the model does not distinguish the kind of fluid, but it uses the Reynolds number as input, which is in a turbulent range. Besides, the height of the channel is sufficiently large to avoid an interaction with the free-surface, in case we want to simulate water. We have to mention that DES has also been validated before by Gajardo et al. (2019), which used the model coupled with a more complex turbine representation, known as Blade Element Momentum (BEM). In their simulations, Gajardo et al. (2019) replicated the flume experiments of the PerAWaT project carried out by Stallard et al. (2013), which consists of two rows of turbines.

The reasons for choosing this experimental case for the validation are because of the available measured data and a large number of devices (30 devices distributed in 12 rows). On the one hand, more data implies more points of comparison, making the validation more precise. On the other hand, the idea of having many rows is because we want to observe the fluctuation of the resultant force per unit area through the rows and detect where it becomes constant, for designing the next experiments.

2.3 Methodology

The resultant force exerted by different turbine arrays is calculated by using the simulated data of the validation case. To do this, we compute the net flux of momentum in the streamwise direction for several control volumes, considering the pressure drop and the viscous losses. These control volumes consider the total height of the channel, and enclose different numbers of rows, as shown in the schematic of Figure 2.7. We emphasize that in this case, we can isolate different control volumes inside the farms to calculate C_{tFarm}, rather than running entirely independent calculations. For example, when we run a case with exactly two rows of turbines, the results have a difference of around 3% to those obtained by extracting two rows from

a case with a total of twelve rows of turbines.

We compare the resultant force from the high-resolution numerical simulation with two analytical expressions, which are calculated by multiplying the resultant force of one device by the number of turbines N_t inside every control volume. In the first expression, we calculate the force by using the undisturbed velocity, U_∞, and the thrust coefficient, C_t, same as in Equation 2.3. On the other hand, in the second expression, we use the average velocity in every disk U_d, which required a modified thrust coefficient, C_t', to calculate the resultant force. In Figure 2.8, we show that the force calculated by using the undisturbed velocity overestimates the results, especially after the 3^{rd} row. This because the turbines starting at the 3^{rd} row no longer experience the undisturbed velocity, U_∞. Instead, the resultant force calculated by using the averaged velocity of the disks, U_d, provides a more accurate representation of the total force imposed by the set of turbines. We also observe that the analytical force goes up and down through the rows, which occurs because the density of turbines per unit area is smaller for rows with an even number of turbines. Further, after the 6^{th} row, all the total forces tend to remain constant, indicating that a fully developed solution can be assumed after six rows.

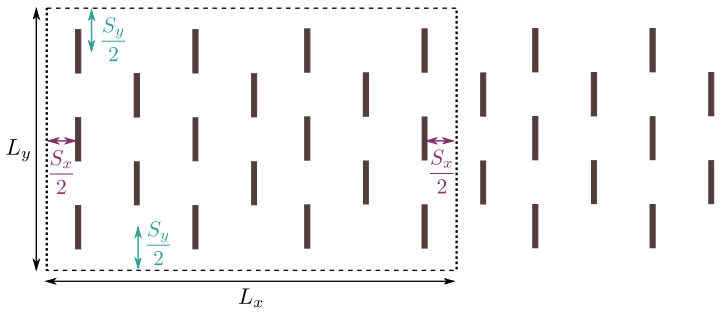

Figure 2.7. Schematic of a representative control volume used to calculate the resultant force for an array of devices. Here L_x and L_y are the length and the width of the control volume, respectively, meanwhile the height, L_z is the same as the channel. In this example, the control volume encloses 18 devices, and comprises a volume that includes from the first to the seventh row of turbines.

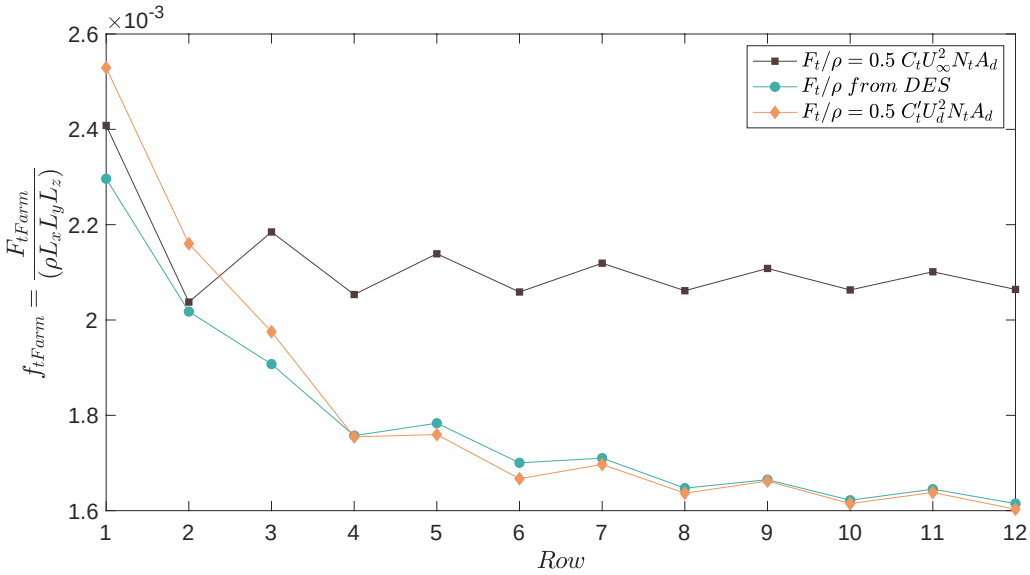

Figure 2.8. Resultant force calculated by using control volumes that go from the first row of turbines through the last one (see Figure 2.7), per unit of mass ($\rho L_x L_y L_z$). ■ Analytic force calculated as the force of one actuator disk times the total number of devices in the farm. ♦ Analytic force calculated by using the average velocity at the location of the disks, U_d, instead of the undisturbed velocity, U_∞. • Resultant force obtained from DES numerical simulations.

Due to the significant differences between the analytical solution using the undisturbed velocity, and the resultant simulated force showed in Figure 2.8, it is inferred that it is more accurate to use the local velocity to calculate the force of a set of turbines. However, we must consider that in coarser-scale models, the only known velocity at the farm location is the grid-cell horizontally-averaged velocity (denoted here by $\langle\cdot\rangle$) at the hub height (subscript h): $\langle U\rangle_h$. Therefore, it is essential to modify the force calculation to represent a farm of turbines at larger-scale models. To achieve this, we propose a thrust coefficient representative for an entire farm, C_{tFarm},

as follows:

$$C_{tFarm} = \frac{2F_{t,DES}}{\langle U \rangle_h^2 A_d N_t}, \tag{2.7}$$

where $\langle U \rangle_h$ is calculated in the area occupied by the turbines. In this way, the new coefficient not only takes into account the wake interactions but also is based on information provided by coarse-scale models.

2.3.1 Thrust Coefficient for a Farm of Turbines

To parameterize the thrust coefficient for an entire farm of turbines, C_{tFarm}, we study the main parameters that dominate the interaction between the flow and the devices. Initially, we suggest that C_{tFarm} would depend on the distance among devices in the streamwise and spanwise directions, S_x and S_y respectively; the disk diameter, D; and the size of the farm in the x and y direction, L_x and L_y. Experiments show that the ratio between the water depth, H, and the hub height, z_{hub}, is also an important variable to take into account since it can change considerably the velocity recovery downstream (Aghsaee and Markfort, 2018).

Another important factor is the angle between the flow and the turbines. Here we only consider the optimal case, where the main flow direction is perpendicular to the rotor. In practice, one should take into account the fact that the thrust coefficient of turbines could be affected up to 10% for yaw angles of 20° (Frost et al., 2017).

For these simulations, we use a flat bottom since we want to isolate the wakes' interaction according to the distribution from the bedforms. On the other hand, when we simulate the turbines in a realistic scenario, we will consider the most relevant bedforms, so we do not want to duplicate the bathymetry effect.

For the purposes of this work, we use a staggered distribution for the turbines since this is the most commonly utilized configuration and it is more efficient than

when the disks are aligned (Daskiran et al., 2015; Markfort et al., 2012; Wu and Porté-Agel, 2013). We also consider the thrust coefficient for an individual device, C_t', to normalize C_{tFarm}, in order to have a parameterization that works for any turbine. By performing numerical simulations, we study the versatility of C_{tFarm} by using different values for the aforementioned parameters, and focus on the overall problem: $C_{tFarm} = C_{tFarm}(S_x, S_y, D, L_x, L_y, H, z_{hub}, C_t')$. In nondimensional form, we cast the problem as:

$$\frac{C_{tFarm}}{C_t'} = \phi\left(\frac{S_x}{D}, \frac{S_y}{D}, \frac{L_x}{S_x}, \frac{L_y}{S_y}, \frac{H}{z_{hub}}\right). \tag{2.8}$$

Previous works have highlighted the importance of not using the area density of the turbines (i.e., $A_d/(S_xS_y)$) since this assumption considers that a change in the streamwise distance would have the same effect as a change in the spanwise direction; this has been demonstrated as being inaccurate (Simón-Moral et al., 2014). This is the reason why the parameters S_x and S_y represent different dimensionless groups in Equation 2.8. The same is true for the farm's size since the farm's width and length independently affect the overall force, even though they have the same total area $A_{Farm} = L_xL_y$. The terms L_x/S_x and L_y/S_y in Equation 2.8 represent the farm size, and they can be interpreted as the number of rows and columns of devices.

2.3.2 Setup for Numerical Simulations

We simulate seven cases, and in each of them, the turbines are distributed in a staggered pattern (same as in Figure 2.1 (i.e., odd rows have three turbines, and pairs, have two)). Since the focus of this research is to study finite-sized farms, the cases have only six rows. The cases vary the turbines separation in the streamwise (S_x/D) and spanwise (S_y/D) directions, as well as the ratio between the depth of the channel and hub height, H/z_{hub}. The simulations are summarized in Table 2.4.

TABLE 2.4

SUMMARY OF THE SIMULATED CASES.

Case	S_x/D	S_y/D	H/z_{hub}
C.1	5	4	4.2
C.2	7	4	4.2
C.3	3	4	4.2
C.4	5	2	4.2
C.5	5	6	4.2
C.6	5	4	3.3
C.7	5	4	5.0

Since our work is focused on tidal energy, we choose parameters according to the characteristics of the ocean and the MHK devices. For the diameter of the turbines, we used a typical value of $D = 10$ m, with a hub height $z_{hub} = 12$ m. Regarding the thrust coefficient, we use the same value as for the validation case (i.e., $\overline{C_t'} = 0.85$) to represent every device. In the ocean, Reynolds numbers can exceed $O(10^8)$; due to computational restrictions, we initially carry out this analysis with $Re_{z_{hub}} = 7.5 \times 10^6$. We do not expect differences in $Re_{z_{hub}}$ to impact our results since it has been shown that increments of Reynolds numbers over $O(10^4)$ do not have any significant effects on the wakes of actuator disks (Mikkelsen and Sørensen, 2003; Sørensen et al., 1998); however, we highlight that they differ on the geometrical details of each specific design. As a new generation of MHK devices emerges, future work will focus on the effects of the Reynolds number for the entire tidal cycle. Concerning the turbulence

intensity, we use an intermediate value equal to 15%. For all the simulated cases, we used the same domain and the same grid resolution as summarized in Table 2.5.

TABLE 2.5

MAIN VARIABLES COMMON FOR ALL THE SIMULATED CASES

Parameter	Value
Turbines diameter (D)	10 m
Hub height (z_{hub})	12 m
Thrust coefficient $\overline{C_t'}$	0.85
Channel length (L_x)	350 m
Channel width (L_y)	240 m
Grid resolution ($im \times jm \times km$)	$268 \times 192 \times 128$
Reynolds number based on the velocity at the hub ($Re_{z_{hub}}$)	7.5×10^6
Lateral boundary conditions	Symmetric

2.4 Results and Discussion

Using the results from simulations C.1 through C.7, we study the sensitivity of C_{tFarm} due to changes in the devices' lateral distance and the depth of the channel. From this analysis, we propose a relation between C_{tFarm} and the parameters listed in Equation 2.8. Finally, we compare results from a previous investigation related to drag parameterizations of infinite farms.

2.4.1 Formulation of the Thrust Coefficient Representative for Farms of Turbines

The solutions of the simulations in Table 2.4 are time-averaged, and we calculate the resultant force for different control volume configurations within the simulated domain (same as in section (2.3).

We observe that the effects on C_{tFarm} of changing the number of devices in the lateral direction are negligible (see Figure 2.9(a)). Actually, for all the shown cases, the coefficient only changes around 4% when we go from two to four columns of turbines. The last is reasonable because regardless of how many columns of turbines are included, the undisturbed flow upstream will face the same total area of turbines (also known as the blockage area). For this reason, we eliminate L_y/S_y from our parameterization. We have to mention that we do not show the case C.4 in Figure 2.9(a) because, in that situation, the devices are too laterally close, and it is not possible to isolate the effect of the columns of turbines to study them.

On the other hand, C_{tFarm} varies noticeably when the longitudinal length of the farm changes (see Figure 2.10(a)). When farms increase from two rows of turbines ($L_x/S_x = 2$) to three rows ($L_x/S_x = 3$), C_{tFarm} decreases. Beyond this, C_{tFarm} remains almost constant as additional rows are included. For our parameterization, we do not consider the case of one row ($L_x/S_x = 1$) since in that situation, S_x is undetermined, and one would expect the wake interactions to not play a strong role in the total effective thrust coefficient C_{tFarm}.

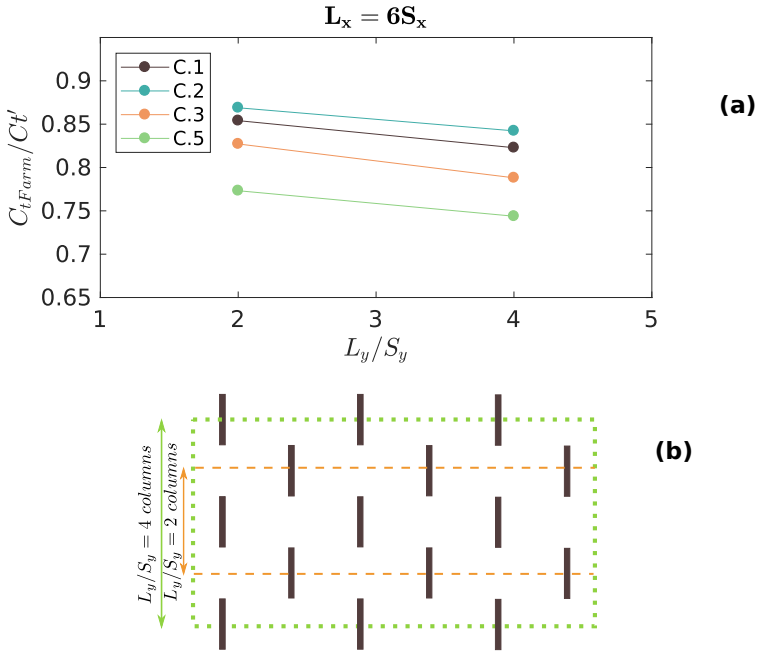

Figure 2.9. (**a**): Variation of C_{tFarm} due to changes in the size of the farm in the spanwise direction, L_y. The ratio L_y/S_y can be interpreted as the number of columns of turbines. (**b**): Schematic of the control volumes used for calculating C_{tFarm} for two and four rows of turbines.

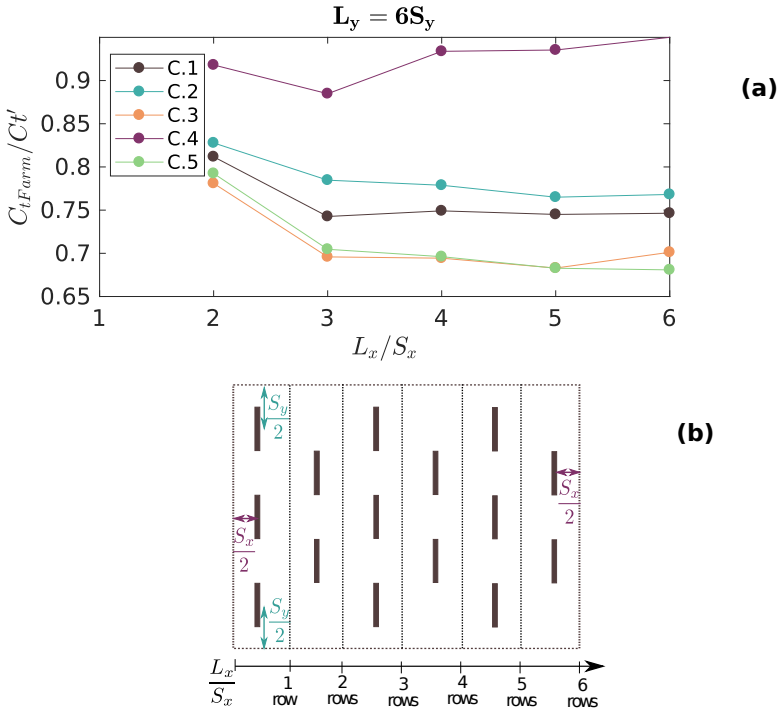

Figure 2.10. (**a**): Variation of C_{tFarm} due to changes in the size of the farm in the streamwise direction, L_x. The ratio L_x/S_x can be interpreted as the number of rows of turbines. (**b**): Schematic of the control volumes used for calculating C_{tFarm} for various numbers of rows.

For studying the effects of S_x/D, S_y/D, and H/z_{hub} on C_{tFarm}, we divide the results into two cases: one for farms with exactly two rows, and another for farms with more than two rows. This distinction is used because of the difference observed previously in Figure 2.10, for the cases where $L_x/S_x = 2$, and $L_x/S_x > 2$.

In Figure 2.11(a) the variation of C_{tFarm} as a function of streamwise separation between the devices is presented. We observe that for farms with two rows, the thrust coefficient remains almost constant. We perform more simulations with exactly two rows using even smaller values of S_x/D, and C_{tFarm} remains independent of changes in S_x/D. We also can see in Figure 2.11(a) that, for more than two rows,

C_{tFarm} increases when S_x/D increases. This is consistent with previous work for vegetation canopies (Simón-Moral et al., 2014), where the authors stated that the thrust coefficient should be maximum for isolated objects (i.e., $S_x/D \to \infty$) because the obstacles or, in our case, the turbines, are completely unsheltered.

In Figure 2.11(b), it is observed that C_{tFarm} decreases when S_y/D increases for farms with any number of rows. This is also consistent with Simón-Moral et al. (2014), where it was noted that when the devices are laterally closer, the average velocity inside the canopy is smaller, which results in a higher thrust coefficient. The aforementioned is reflected in Figure 2.10, where case C.4 is the one with the highest C_{tFarm}. The velocity inside the farm is especially low in staggered farms with laterally close devices since they block the flow. Another study (Nishino and Willden, 2012) shows that the efficiency of a wide or deep farm monotonically increases when the lateral separation between turbines decreases towards the lowest limit (i.e., $S_y/D = 1$); this is consistent with our results as well.

Regarding the ratio between the depth and the hub height (Figure 2.11(c)), we do not observe a significant change in C_{tFarm}, regardless of the number of rows. In fact, with an increment of 50% in H/z_{hub}, we calculate a change of less than 4% in C_{tFarm}. We conclude that H/z_{hub} does not play a role in our parameterization. However, we note that we can only ensure the validity of this result for cases where $H/z_{hub} \geq 3.3$, and we acknowledge that this parameter could be important for representing devices that are installed closer to the free-surface as in the case of the work of Aghsaee and Markfort (2018); Kolekar and Banerjee (2015); Riglin et al. (2015).

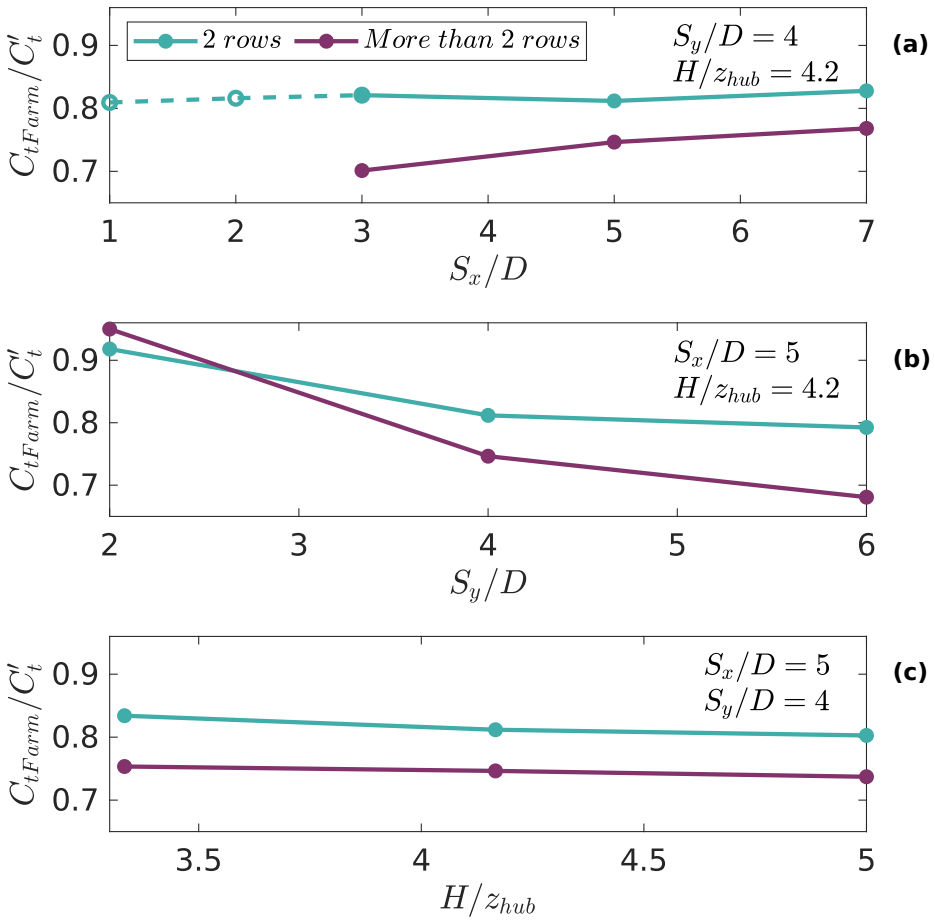

Figure 2.11. Changes in C_{tFarm} due to the variation of: (**a**) The streamwise distance between devices, S_x/D, (**b**) the spanwise distance between devices, S_y/D, and (**c**) the ratio between the depth of the channel and the hub height, H/z_{hub}. The results are divided into two cases: farms with two rows of turbines (light blue), and farms with more than two rows (purple). Since we do not observe a significant influence of S_x/D on C_{tFarm} for farms with two rows, we perform extra simulations (marked with dashed lines), where we see C_{tFarm} remains insensitive to the distance in the streamwise direction

As a summary, we infer that C_{tFarm} is not a function of L_y/S_y nor H/z_{hub}. We also observe two regimes concerning the length of the farm: one for farms with exactly two rows of turbines, and the other for farms with more than two rows. In the former, C_{tFarm} is only a function of the lateral distance of the devices (S_y/D). In the latter, C_{tFarm} is function of S_x/D in addition to S_y/D.

Considering the discussion above, we propose an analytical solution for C_{tFarm} which is characterized by two limiting cases:

1. For farms with two rows, the expression for C_{tFarm} is inversely proportional to the lateral distance between devices, S_y/D. This value can go from $S_y/D = 1$, when the turbines are adjacent to each other, to $S_y/D \to \infty$ for very laterally spaced farms, where one would expect the drag force to be additive since the wakes do not interact.

2. For farms with more than two rows, the dependence of C_{tFarm} is still inversely proportional to S_y/D but also decays exponentially with the distance between the devices in the streamwise direction S_x/D. An exponential decay is proposed because it tends to zero as $S_x/D \to 0$ (i.e., the devices get closer), which captures the fact that the flow cannot penetrate the farm. On the other hand, when the streamwise distance between the devices increases, the exponential term tends towards unity, which is equivalent to saying that C_{tFarm} becomes independent of S_x/D. This expression is similar to the one proposed by Simón-Moral et al. (2014) for parameterizing canopies of vegetation.

Thus we present the following expression for C_{tFarm}:

$$\frac{C_{tFarm}}{C_t'} = \begin{cases} \left(\boldsymbol{\beta}\frac{D}{S_y}\right) + \boldsymbol{\gamma} & , \frac{L_x}{S_x} = 2 \\ \left(1 - exp\left(-\boldsymbol{\alpha}\frac{S_x}{D}\right)\right)\left(\frac{D}{S_y}\right) + \boldsymbol{\zeta} & , \frac{L_x}{S_x} > 2 \end{cases} \tag{2.9}$$

Here, $\boldsymbol{\beta} = 0.39$, $\boldsymbol{\gamma} = 0.72$, $\boldsymbol{\alpha} = 0.25$, and $\boldsymbol{\zeta} = 0.57$ are coefficients empirically calculated by minimizing the error in the difference between the data obtained from the simulations and that predicted by the proposed relation. The value of these coefficients could be improved by running more numerical simulations to have more sample points.

The coefficient $\boldsymbol{\alpha} = 0.25$ attenuates the growth of the exponential function, and

yields a C_{tFarm}/C_t' which reaches a value of 0.99 at roughly $S_x = 19D$, meaning that for streamwise separations larger than $19D$, the wake is essentially fully recovered. This is in agreement with various recovery distances reported in the literature (Chen et al., 2017; Myers and Bahaj, 2012; Stallard et al., 2013).

With respect to the factors $\boldsymbol{\gamma}$ and $\boldsymbol{\zeta}$ in the Equation 2.9, they can be interpreted as the limit of C_{tFarm}/C_t' for very laterally spaced farms (i.e., when $S_y/D \to \infty$). In this case, the average velocity at the center of the farm tends to be the same as the undisturbed velocity, so that we can assume:

$$\lim_{S_y \to \infty} \frac{C_{tFarm}}{C_t'} = \left(\frac{U_d}{U_\infty}\right)^2 = \begin{cases} \boldsymbol{\gamma} & , \frac{L_x}{S_x} = 2 \\ \boldsymbol{\zeta} & , \frac{L_x}{S_x} > 2 \end{cases} \tag{2.10}$$

In Figures 2.12 and 2.13 we show the empirical solution proposed in Equation 2.9 with the results from the DES simulations. In both figures, we fix values of S_y/D to observe how C_{tFarm} changes with variations in S_x/D (Figure 2.12(a) and 2.13(a)), and vice versa (Figure 2.12(b) and 2.13(b)). As mentioned above, for farms with two rows, C_{tFarm} does not depend on S_x/D, which is why in Figure 2.12(a) the lines are horizontal. Meanwhile, in Figure 2.12(b), we see that all curves collapse despite different values of S_x/D. For farms with more than two rows (Figure 2.13), we see that our expression for C_{tFarm} is capable of representing the effects of changing the distance between devices in both lateral directions.

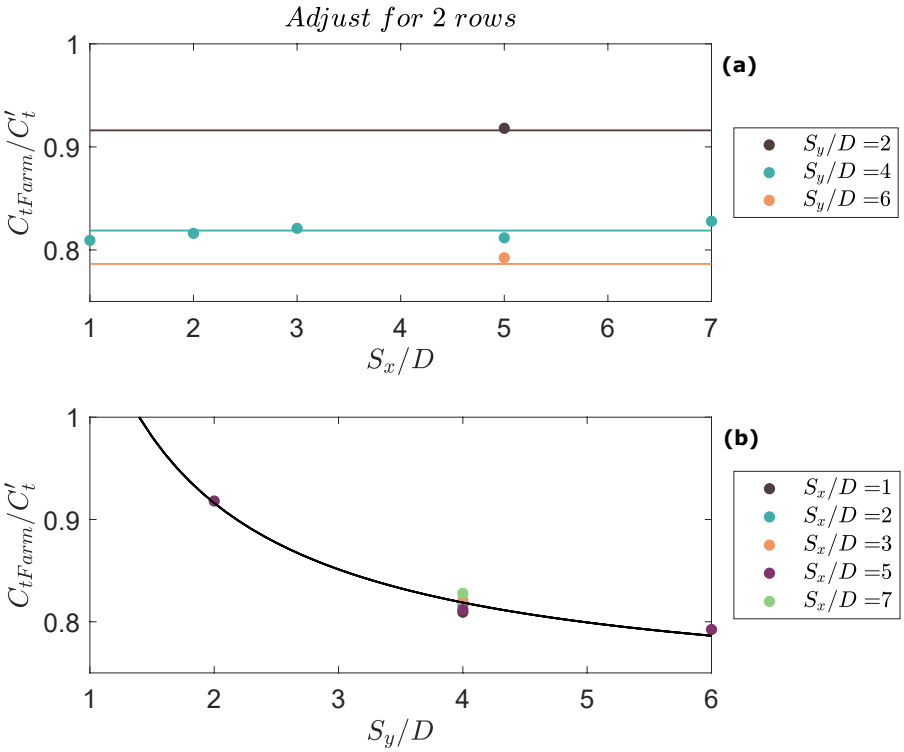

Figure 2.12. C_{tFarm}/C_t', for farms with exactly two rows of turbines, versus the disk separation in: (**a**) the streamwise direction, and (**b**) in the spanwise direction. Continuous line: Empirical solution proposed in Equation 2.9. Dots: Results from DES numerical simulations.

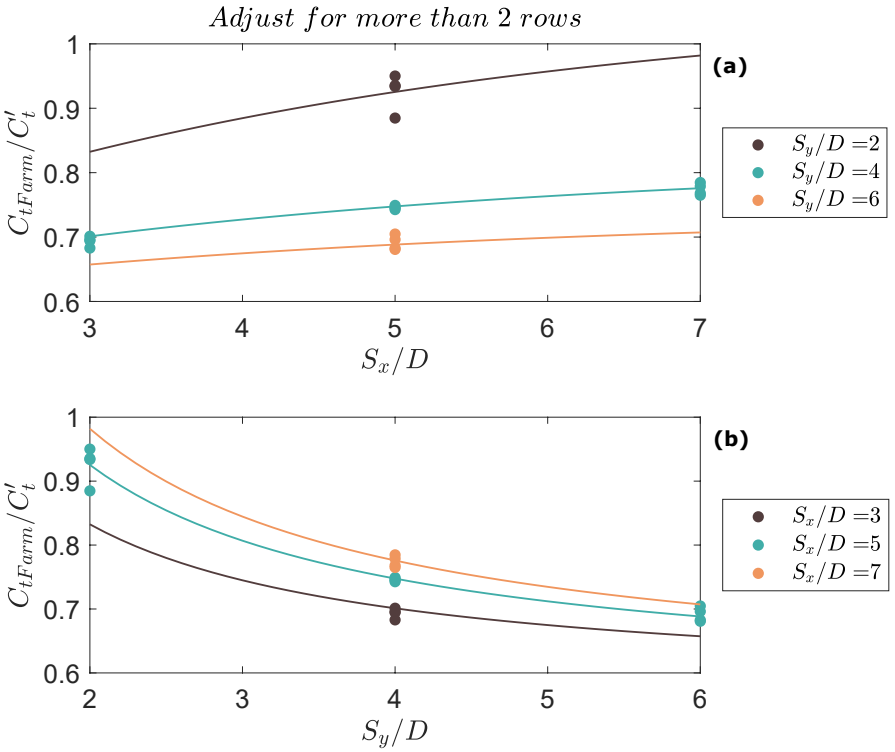

Figure 2.13. C_{tFarm}/C'_t, for farms with more than two rows of turbines, versus the disks separation in: (**a**) the streamwise direction, and (**b**) in the spanwise direction. Continuous line: Empirical solution proposed in Equation 2.9. Dots: Results from DES numerical simulations.

2.4.2 Comparison of $\mathbf{C_{tFarm}}$ Parameterization With Previous Work

To demonstrate the consistency of our parameterization with other studies, we compare our results with the parameterization proposed by Abkar and Porté-Agel (2015). As noted in the Introduction, the authors of Abkar and Porté-Agel (2015) considered an infinite farm of turbines, and incorporated a correction factor, $\xi = U_\infty/\langle U \rangle_h^2$, to account for differences in the free-stream and horizontally-averaged

velocities:

$$F_t = N_t \frac{1}{2} \rho \xi^2 \langle U \rangle_h^2 A_d, \tag{2.11}$$

In their work, Abkar and Porté-Agel (2015) showed that the implementation of ξ can improve the representation of farms of turbines in larger scale models. Their approach was empirical, so ξ was computed numerically for a wide variety of disk configurations. To compare our expression with the results of Abkar and Porté-Agel (2015), we rewrite Equation 2.9 to incorporate ξ into C_{tFarm}:

$$\frac{C_{tFarm}}{C_t'} = \frac{1}{C_t'} \frac{2F_t}{\langle U \rangle_h^2 A_d N_t} = \frac{1}{C_t'} \frac{2F_t}{U_d^2 A_d N_t} \frac{U_d^2}{\langle U \rangle_h^2} \tag{2.12}$$

Since the parameterization of Abkar and Porté-Agel (2015) was made for an infinite farm, we can assume that the flow reaches a fully developed state, which means that $2F_t / \left(U_d^2 A_d N_t C_t'\right) \rightarrow 1$. The term $U_d^2 / \langle U \rangle_h^2$ in Equation 2.12 can be compared with the ξ parameter by using the relation $U_d = (1-a)U_\infty$ (Burton et al., 2011), where $a = 0.25$ is an induction factor used by Abkar and Porté-Agel (2015). In this way, we can estimate ξ from our analytical solution.

In Table 2.6, we show that using the proposed expression, we retrieve values for ξ with an error of less than 3.5% compared with the results of Abkar and Porté-Agel (2015). The crucial difference with our work is that we can also take into account the effect of two different turbines configurations just by knowing the lateral distance between devices, without needing to run computationally expensive numerical simulations.

TABLE 2.6

COMPARISON OF THE RESULTS OF THE ξ PARAMETER PROPOSED BY ABKAR AND PORTÉ-AGEL (2015) WITH ξ CALCULATED BY USING OUR PARAMETERIZATION OF C_{tFarm}/C'_t.

S_x/D	S_y/D	C_{tFarm}/C'_t	ξ Calculated	ξ proposed by Abkar and Porté-Agel (2015)	error (%)
5	5	0.71	1.12	1.13	0.6
7	7	0.69	1.10	1.07	3.2

2.5 Summary

In this chapter, we proposed an expression for a new thrust coefficient, C_{tFarm}, which is meant to represent a finite-sized farm of MHK devices in ocean circulation models. Our primary objective is to include the resistance force's variation due to the distribution of the devices. We used the hybrid turbulence model, DES, coupled with the actuator disk approach, to simulate staggered farms of turbines by changing the lateral separation of the devices and the channel's depth.

We validated the model by replicating the laboratory experiments shown in Markfort et al. (2012). Despite the simple representation of the turbines, we could faithfully reproduce the velocity deficit downstream. With these simulations, we calculated the resultant force of various farm sizes to detect which variables are more relevant in the representation of turbine arrangements at larger scales. We also analyzed how C_{tFarm} behaves under changes in device spacing to propose an expression for this new coefficient.

Finally, we concluded that C_{tFarm} behaves differently for farms with exactly two rows, and farms with more rows. In the first scenario (farms with two rows), the lateral separation of the devices is the only variable required in the calculation of C_{tFarm}, mainly because it is primarily related to the area of the turbines which the flow faces when it enters to the farm. For laterally closer devices, C_{tFarm} increases monotonically until $S_y/D = 1$. For farms that have more than two rows, the streamwise distance between the devices becomes relevant too. This parameter was incorporated into the C_{tFarm} expression by using an exponential decay which goes from zero for farms with no space between rows (i.e., $S_x = 0$) to unity for farms with highly spaced rows (i.e., $S_x > 19D$). We also concluded that H/z_{hub} is not a relevant variable in the representation of farms of turbines, at least when its value is equal or bigger than 3.3.

With the new proposed expression, it is possible to easily calculate a thrust coefficient for a finite farm of turbines, just by knowing the number of rows and the lateral separation of the devices. However, we highlight that before using our parameterization, a few notes are necessary:

- It is designed for staggered farms, where all the turbines occupy the same ground area.
- It does not consider a significant misalignment between the mean flow direction and the turbine axes.
- It is designed for devices installed at the bottom of the sea, and which do not interact with the free-surface.

We have to highlight that further simulations are necessary to improve the precision of the coefficients presented in the equation of C_{tfarm}.

In the next chapter, we implement the C_{tFarm} coefficient into the ocean circulation model FVCOM (Chen et al., 2003) to simulate the tides and their interaction with the bathymetry in the Chacao channel. By using this model, we could study the

effects of farms of turbines in a more realistic domain with a flow that completes entire tidal cycles.

CHAPTER 3

MHK DEVICES FARM REPRESENTATION IN OCEAN CIRCULATION MODELS

3.1 Introduction

The Chacao Channel, Chile, located between Puerto Montt and Chiloé Island, represents an attractive place to harness tidal energy. Almost the 60% of the energy sources in Chiloé Island are non-renewable (CNE, Chile, 2020); however, the Chilean government is planning to reach at least a 70% of renewable sources of energy in the country by the year 2050. Chacao channel connects the Pacific ocean with the interior fjords, and narrows between the continent and Chiloé Island, which allows the flow to reaches velocities over $4m/s$ (Guerra et al., 2017). In addition, a study based on the distance to the electric grid, available resources, channel depth, and possible conflicts with the fishery industry, has shown that this channel is one of the best places in the surrounding area for installing MHK devices (Cruz et al., 2009).

Nevertheless, installing an MHK farm in the Chacao channel could negatively affect some aspects of the hydrodynamics and local habitats. The acceleration of the flow between devices and the deceleration downstream of the farms changes the bottom shear, which can move the paths of sedimentation and alter local morphodynamics (Brown and Neill, 2015; Fairley et al., 2015). Besides, the interaction of the flow and the top of the turbines raises the turbulent kinetic energy (TKE), which increments the flow mixing and could increase the sediment transport. An increment in transport of sediment could have different effects such as an alteration in the available oxygen if the sediments are high in organic matter (Gill, 2005), and impair the

fertilization of benthic organisms (Gaylord, 2008). Because of the reasons mentioned above, it is necessary to assess the impacts of the installation of marine farms in the velocity, TKE, and bottom shear.

Numerical simulations can be useful tools to study the interaction between the flow, MHK devices, and the environment at different temporal and spatial scales for what there are plenty of options for the flow solver and the turbines representation. Choosing the right tools is not trivial since the ocean dynamics are composed by different scales that cannot be covered by using only one numerical model because of the computational cost restrictions. In the representation of a farm of turbines in a realistic environment there are mainly two relevant temporal and spatial scales: One is associated with the highly turbulent zone downstream the devices known as wakes, and how the distribution of the devices can affect the resistance force of the entire farm. The other scale involved is the one related to the interaction between an entire farm of turbines with tides and the local environment.

For representing the wake's scales, there are some high-resolution solvers that can work in conjunction with different turbine representations. One example is the hybrid turbulence model called Detached Eddy Simulation (DES) (Escauriaza and Sotiropoulos, 2010, 2011a,b; Gajardo et al., 2019; Soto-Rivas et al., 2019; Spalart and Allmaras, 1992) that solves the mean velocity field close to the walls, and can calculate the large structures downstream the devices. DES can be coupled with actuator models representing the turbines as an equivalent sink of momentum, such as the Actuator disk model (ADM) (Burton et al., 2011; Meyers and Meneveau, 2012; Porté-Agel et al., 2014b; Ramos et al., 2019; Soto-Rivas et al., 2019), that distributes the force in a static disk with a diameter equal to the turbine. Some more sophisticated models can represent the rotation of the turbines (Ouro and Stoesser, 2017; Ouro et al., 2019) and even their entire geometry (Daskiran et al., 2015; Kang et al., 2012, 2014; Riglin et al., 2015, 2016; Schleicher et al., 2015). Nonetheless, it is impossible

to use those models at larger scales to represent multiple turbines interacting with realistic environments because of the differences in the spatial resolution and the physical variables between the turbine and channel scale.

At larger scales we can use ocean circulation models (OCM), which integrate the tides, the morphology of the bay or tidal channel, and couples the flow dynamics to a parameterization that represents an entire farm of turbines. Some examples are the works of Fallon et al. (2014) and Nash et al. (2014) that represented farms of MHK devices over real bathymetries by using the momentum sink approach integrated into the bi-dimensional model DIVAST (Falconer et al., 2001). In both investigations, the authors represented different turbine separations by changing the devices' density (i.e., numbers of devices per unit area) in the grid elements. An example of three-dimensional simulations is the work of Neill et al. (2012), which represented a farm of turbines in Alderney Race, France, by incorporating additional bed friction into the model 3-D POLCOMS (Holt and James, 2001). The enhancement of bed friction has also been used for 2-D simulations (Garcia-Oliva et al., 2017; Plew and Stevens, 2013); however, for three-dimensional models, oversimplifies the computations to represent the flow depth and the vertical position of the devices. Another three-dimensional example is the finite-volume model ROMS (Shchepetkin and McWilliams, 2005), which was used by Roc et al. (2013) to represent devices using the momentum sink approach over a flat bathymetry. Later, Goward Brown et al. (2017) used the same approach of Roc et al. (2013) to model turbines in Pentland Firth, United Kingdom, using tides and bathymetry data of the area. Another well-known 3-D model is FVCOM (Chen et al., 2003), which has the advantage of using unstructured elements to adapt the grid to the coastline. By using the momentum sink approach, some studies have represented MHK devices in FVCOM over flat bathymetries (Yang et al., 2013) and under realistic conditions (Murray and Gallego, 2017; Wang and Yang, 2017; Yang et al., 2014).

However, in all the investigations mentioned above the analysis did not consider the changes on the resistant force caused by different turbine distributions. This problem can be solved by representing just one turbine per grid cell, but in that case, the location of the devices is restricted by the grid resolution. Considering the distribution of the devices is essential because depending on the distance between the turbines and their disposition, the velocity of the flow can change in direction and magnitude, producing more efficient configurations than others (Myers and Bahaj, 2012; Riglin et al., 2016). As we can see, multiple previous investigations use OCM to represent MHK devices in real marine environments; however, most of them simulated an unrealistic number of turbines that exceeded hundreds and even thousands of units (Dominicis et al., 2017; Garcia-Oliva et al., 2017; Yang et al., 2013). Another limitation in the representation of marine turbines in OCM is the lack of field measurements for validating their performance. Some investigations use OCM to replicate laboratory conditions with MHK devices that have shown good agreement between simulated and measured data (Roc et al., 2013; Thiébot et al., 2016).

In this Chapter, we use numerical simulations to represent a farm of MHK devices in the Chacao channel and assess their effects on the local environment. For representing the interactions between tides and the bathymetry, we use the OCM model FVCOM; meanwhile, for representing a finite farm of turbines we incorporate to FVCOM the tidal turbine module provided by Murray and Gallego (2017), incorporating the parameterization we derived in Chapter II, C_{tFarm} (Soto-Rivas et al., 2019), which considers the separation between devices and the number of rows. For obtaining the parameterization, we used a high-resolution numerical simulation to represent every device inside a group of turbines and recognize the most critical factors in a particular farm's resistance force. Here, we evaluate how tides and different local bathymetries interact with the farms. In particular, we observe changes in the streamwise velocity, TKE, and shear stresses at the bed since they can potentially

produce negative impacts in the local environment.

The Chapter is organized as follows: In section 3.2, we introduce the model FVCOM coupled with the momentum sink approach for representing farms of turbines. In section 3.3, we study the undisturbed conditions in the Chacao channel to select the most suitable place for installing a farm of turbines, according to the ranges of operation of a commercial device. After choosing the farm's location, we analyze the local bathymetry using the variogram method to design an appropriate numerical grid to represent the essential features of the bed and relate them to the flow/turbines interaction. In section 3.4, we show the results of running three independent simulations by placing a farm with the same number of turbines in each location. The simulated farm is finite-sized, so we can implement the coefficient C_{tFarm} we propose in Chapter II. In section 3.5, we discuss the results. We have to highlight that there are no available measurements of the flow downstream real MHK farms in terrain to validate our model; however, our goal is to predict the changes in the velocity of the flow, and the energy budget before installing them in the Chacao channel. Finally, in section 3.6, we present a summary of the Chapter.

3.2 Numerical Simulations of MHK Farms in the Chacao Channel

For simulating the tides in the Chacao channel, we use FVCOM (Chen et al., 2003), a three-dimensional, unstructured, finite-volume hydrodynamic model that solves the primitive ocean circulation equations for mass, momentum, salinity, and temperature of the flow forced by tides, wind stress, and river discharges, among others. The equations for mass and momentum conservation solved by FVCOM in the x, y, and z directions (East, North, and vertical directions, respectively) are as follows:

$$\frac{\partial u}{\partial x} + \frac{\partial v}{\partial y} + \frac{\partial w}{\partial z} = 0 \tag{3.1}$$

$$\frac{\partial u}{\partial t} + u\frac{\partial u}{\partial x} + v\frac{\partial u}{\partial y} + w\frac{\partial u}{\partial z} - fv = -\frac{1}{\rho}\frac{\partial P}{\partial x} - \frac{1}{\rho}\frac{\partial q_0}{\partial x} + \frac{\partial}{\partial z}\left(K_m\frac{\partial u}{\partial z}\right) + F_u \qquad (3.2)$$

$$\frac{\partial v}{\partial t} + u\frac{\partial v}{\partial x} + v\frac{\partial v}{\partial y} + w\frac{\partial v}{\partial z} - fu = -\frac{1}{\rho}\frac{\partial P}{\partial y} - \frac{1}{\rho}\frac{\partial q_0}{\partial y} + \frac{\partial}{\partial z}\left(K_m\frac{\partial v}{\partial z}\right) + F_v \qquad (3.3)$$

$$\frac{\partial w}{\partial t} + u\frac{\partial w}{\partial x} + v\frac{\partial w}{\partial y} + w\frac{\partial w}{\partial z} = -\frac{1}{\rho}\frac{\partial q_0}{\partial z} + \frac{\partial}{\partial z}\left(K_m\frac{\partial w}{\partial z}\right) + F_w \qquad (3.4)$$

where u, v, and w are the velocities in the East, North, and vertical directions, respectively, f is the Coriolis parameter, F_u and F_v are the horizontal momentum diffusivity terms, P and q_0 are the hydrostatic and non-hydrostatic pressures, respectively, and K_m is the vertical eddy viscosity coefficient.

For the turbulent kinetic energy (TKE), q, we implement the Mellor-Yamada closure scheme that use an equation for q and other for q^2l, where $q = \sqrt{(u'^2 + v'^2)/2}$ and l is the turbulent macro-scale (Mellor and Yamada, 1982). In this model, the TKE is defined by velocity fluctuations in the horizontal directions, and is diffused in the vertical direction by using a vertical eddy diffusion coefficient, K_q. The two equations for the closure model are as follows:

$$\frac{\partial q^2}{\partial t} + u\frac{\partial q^2}{\partial x} + v\frac{\partial q^2}{\partial y} + w\frac{\partial q^2}{\partial z} = 2(P_s + P_b - \varepsilon) + \frac{\partial}{\partial z}\left(K_q\frac{\partial q^2}{\partial z}\right) + F_q \qquad (3.5)$$

$$\frac{\partial q^2 l}{\partial t} + u\frac{\partial q^2 l}{\partial x} + v\frac{\partial q^2 l}{\partial y} + w\frac{\partial q^2 l}{\partial z} = \left(E_1(P_s + P_b) - \frac{\tilde{W}}{E_1}\varepsilon\right) + \frac{\partial}{\partial z}\left(K_q\frac{\partial q^2 l}{\partial z}\right) + F_t \qquad (3.6)$$

where P_s and P_b are the shear and buoyancy production terms, F_q and F_l represent the horizontal diffusion of the TKE and macro-scale, ε is the dissipation rate of TKE, $\tilde{W}$ is a wall proximity function, and E_1 is a model coefficient (more details about these equations can be found in Chen et al. (2003)).

The use of FVCOM for simulating the Chacao channel was validated in the work of Guerra et al. (2017), where field measurements were compared with simulated velocities and TKE profiles. Guerra et al. (2017) carried out high-resolution measurements of the bathymetry every 10 m, tidal currents by using Acoustic Doppler Current Profilers (ADCPs), and sea-level elevation from tidal gauges.

One of the advantages of FVCOM is the option to use nested domains, which reduces the computational cost by extracting the boundary conditions from a larger domain with less resolution. Figure 3.1 shows the domain used to simulate the flow around the entire Chiloé island to extract the boundary conditions for the Chacao channel (zoom shown in Figure 3.1). We use the domain highlighted in orange in Figure 3.1 in all the following simulations.

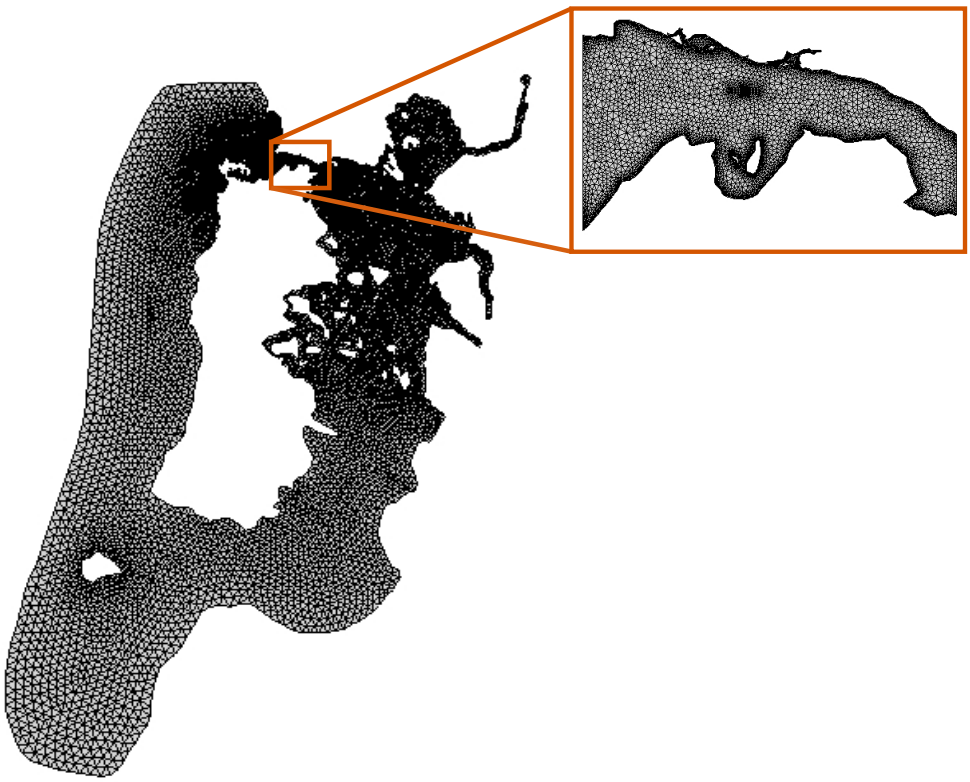

Figure 3.1. Grid for the numerical simulations of the Chacao channel in FVCOM. The entire mesh surrounds the entire Chiloé island and is used to obtain the boundary conditions for the Chacao channel. Meanwhile, the zoom shows the domain we use for all the simulations, which has a higher resolution.

3.2.1 Incorporation of Farms of Turbines in FVCOM

To incorporate the farms of turbines in FVCOM, we use the tidal turbine module provided by Murray and Gallego (2017). This module includes the force exerted by the devices, F_{tFarm}, in the momentum conservation equations in the mean streamwise

direction, x (Equation 3.2) as follows:

$$\frac{\partial u}{\partial t}+u\frac{\partial u}{\partial x}+v\frac{\partial u}{\partial y}+w\frac{\partial u}{\partial z}-fv=-\frac{1}{\rho}\frac{\partial P}{\partial x}-\frac{1}{\rho}\frac{\partial q_0}{\partial x}+\frac{\partial}{\partial z}\left(K_m\frac{\partial u}{\partial z}\right)+F_x-\mathbf{F_{tFarm}} \quad (3.7)$$

In the last equation, we improve F_{tFarm} by using the coefficient C_{tFarm} we calculated in the previous chapter as:

$$F_{tFarm}=\frac{1}{2}\rho u^2 A_d C_{tFarm} N_t. \quad (3.8)$$

Here, A_d is the area of each disk, same as Chapter II; meanwhile, N_t is the total number of devices per grid cell. The velocity in the streamwise direction u corresponds to the velocity in the grid cell in the vertical layer where the turbines are located, which is equivalent to $\langle U\rangle_h$ from Chapter II (see Equation 2.7).

Some studies suggest incorporating new terms to the TKE equations for representing MHK devices in ocean circulation models (Li et al., 2017; Roc et al., 2013), and wind turbines in mesoscale models (Kasmi and Masson, 2008; Rados et al., 2009; Réthoré et al., 2009). With the suggested modifications, Equations 3.5 and 3.6 are:

$$\frac{\partial q^2}{\partial t}+u\frac{\partial q^2}{\partial x}+v\frac{\partial q^2}{\partial y}+w\frac{\partial q^2}{\partial z}=2(P_s+P_b+\mathbf{P_{tp}}-\mathbf{P_{td}}-\varepsilon)+\frac{\partial}{\partial z}\left(K_q\frac{\partial q^2}{\partial z}\right)+F_q \quad (3.9)$$

$$\frac{\partial q^2 l}{\partial t}+u\frac{\partial q^2 l}{\partial x}+v\frac{\partial q^2 l}{\partial y}+w\frac{\partial q^2 l}{\partial z}=\left(E_1(P_s+P_b)-\mathbf{P_l}-\frac{\tilde{W}}{E_1}\varepsilon\right)+\frac{\partial}{\partial z}\left(K_q\frac{\partial q^2 l}{\partial z}\right)+F_t \quad (3.10)$$

where the new terms are P_{tp}, P_{td}, and P_l which represents the turbines' production and dissipation, and an additional term that interferes in the turbulence length scale,

respectively.

Previous investigations that have used the modified TKE equations (Kasmi and Masson, 2008; Li et al., 2017; Rados et al., 2009; Roc et al., 2013; Réthoré et al., 2009) showed significant improvements in velocity and TKE in the near wake (around up to $8D$ downstream the devices). However, the new terms, P_{tp}, P_{td}, and P_l, are empirical and have been calibrated for specific circumstances, besides some of their assumptions are only valid for atmospheric conditions. For this reason, we do not modify the TKE equations, but we acknowledge the limitation of our representation in the near wake.

3.3 Methodology

The first step for studying the interactions of turbines with the flow and the bathymetry of the Chacao channel is to run a base case without MHK devices, which we labeled as case 0. For the simulations with turbine farms, we select three zones to compare the changes in the flow-farm interaction due to the local conditions. With the results of case 0, we choose the most suitable places for installing the turbines based on real MHK devices' operational depth and velocity. Later, we characterize the local bathymetries of every zone, for which we use the variogram method to know the leading length scales of bed features and design an appropriate grid discretization. After simulating a mid-sized farm of turbines in the three different zones, we compare the velocity, TKE, and bottom shear downstream of the farms with the base case without devices.

We run all the simulations in the zone highlighted in orange in Figure 3.1, which is discretized with around four thousand nodes in the horizontal directions and ten layers in the vertical direction. For the vertical discretization, we use the sigma-layer approach, which consists of the even division of the depth, which means, in deeper zones, the layers cover a larger space. For all the cases, the turbines are represented

by an average of two sigma layers. Every case is run during 45 simulation days. The boundary conditions for the channel's inlet and outlet are obtained from a larger domain using the nesting option of FVCOM. Meanwhile, the boundary conditions of the larger domain are the tides obtained from the software TPXO (Egbert and Erofeeva, 2002). For the bottom roughness, we use a value of $z_0 = 40$ mm, which was calibrated before by Guerra et al. (2017).

3.3.1 Choice of Farm Location

For the representation of the disks in the Chacao channel, we use the features of a real MHK device, to define suitable places for the installation based on the depth and velocity ranges. The device we choose is the *Sabella* D10 turbine (Paboeuf et al., 2016), which has a diameter $D = 10$ m and a hub height $z_{hub} = 12$ m. For the thrust coefficient, we use a typical value of $C_t = 0.8$, which is equivalent to use a modified coefficient $C_t' = 1.5$. Concerning the velocity, the cut-in speed of the devices is equal to 0.4 m/s; meanwhile, the cut-out speed is 4 m/s (Paboeuf et al., 2016).

For the farm location, we select an area with a depth range between 40 m and 85 m, according to the operating depth. Figure 3.2, shows the minimum and maximum depths through the entire simulated time at every point. The gray areas of the figure are the places out of the imposed limits. Figure 3.2 also shows two restricted areas where it is not possible to install the turbines; one of them is an anchoring forbidden area, and the other one is an indigenous protected area.

Another factor to consider in the farm location is the available power, which is proportional to cubed velocity. Figure 3.3, is colored by the absolute value of the time-averaged velocity, which is divided into two regimes; flood (where the flow goes from West to East), and ebb (where the flow goes from East to West). Grays areas on the figure show the points where the averaged velocity is out of the functioning range. One relevant point in Figure 3.3 is the velocity asymmetry since it shows that

the ebb has a higher magnitude than the flood regime in some places, such as the East end of the domain.

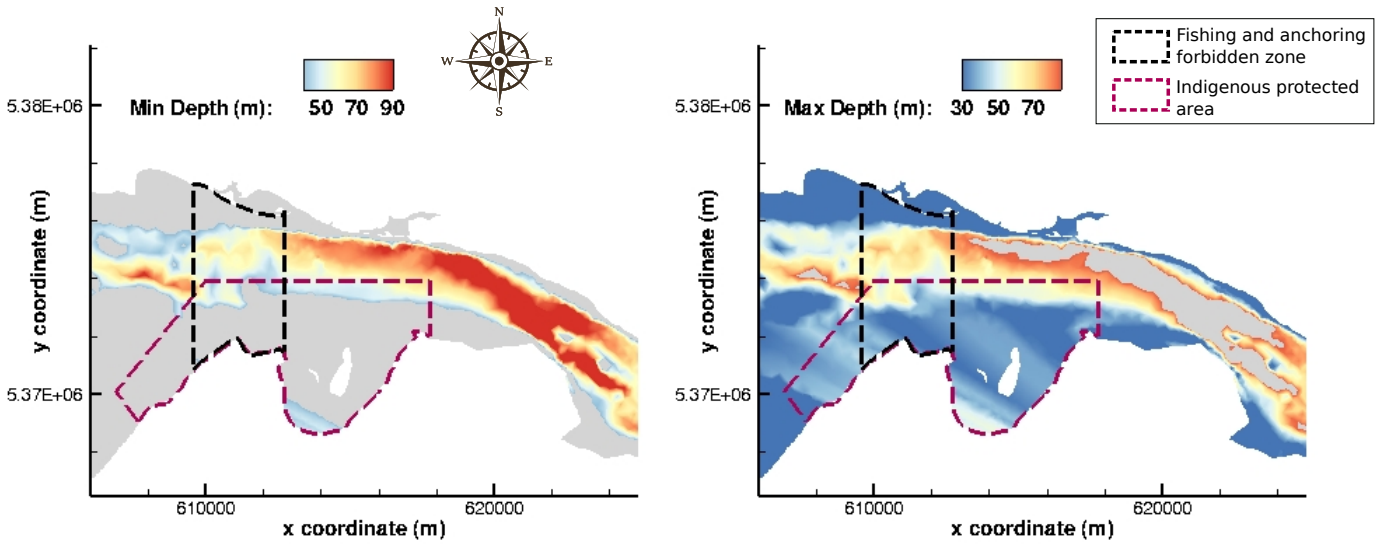

Figure 3.2. Minimum (left) and maximum (right) depth at every point through the time in the Chacao channel. Gray areas show the points where the minimum depth is under 40 m, and the maximum depth is over 85 m. Enclosed in dashed lines are the areas where the installation of MHK devices is restricted.

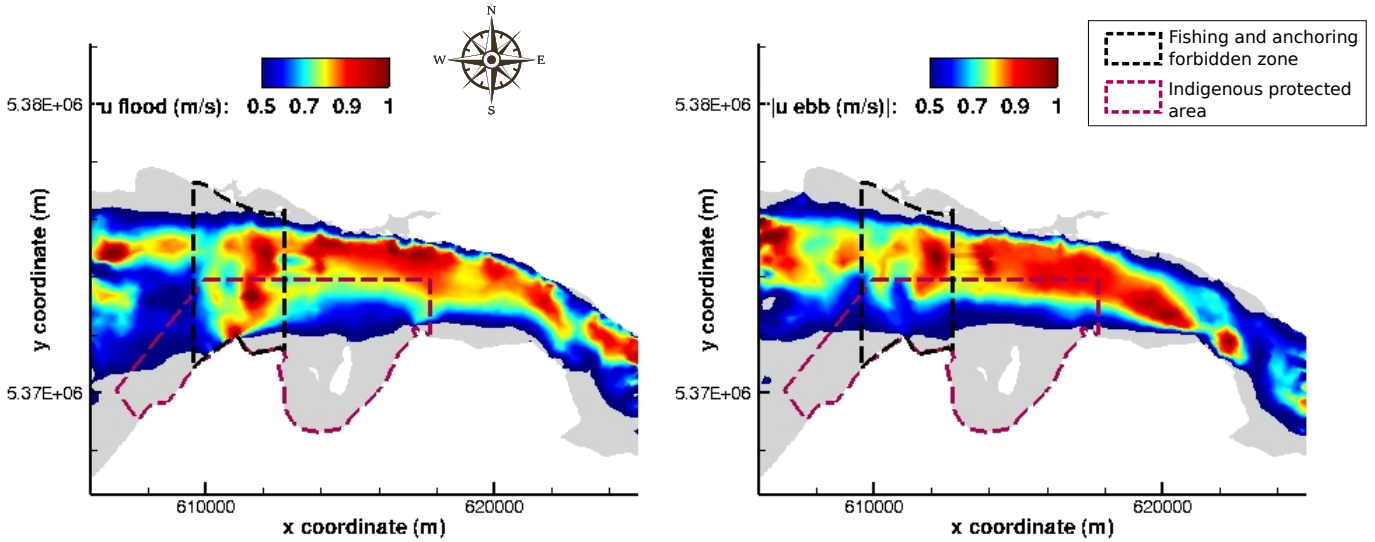

Figure 3.3. Absolute value of the time-averaged velocity at the hub height. Left: Ebb flow. Right: Flood flow. Gray areas show the points where the velocity is under 0.4 m/s and over 4 m/s. Enclosed in dashed lines are the areas where the installation of MHK devices is restricted.

We simulate three different farms of turbines labeled as cases A, B, and C, in the locations shown in Figure 3.4. The figure shows that case C is the closest one to the coastline and also is the deepest one; meanwhile, case A is the furthest one from the coastline and the shallowest. The reason for studying three farms across the channel is to compare the flow-farm interaction with different local conditions.

The area occupied by the farms determines the dimensions of each zone. Because this work's scope is to study finite-sized farms, we simulate medium farms with a total of 27 turbines distributed in a staggered way. The separation between devices in the streamwise direction is equal to $5D$ to harness the acceleration produced by the discs upstream, as is recommended in O'Doherty et al. (2011). For the lateral separation, we choose a distance of $4D$ to avoid significant interaction among the wakes that could reduce the performance of the turbines Riglin et al. (2016). With this characteristics the dimensions of each zone are $300 \times 200m^2$ as shown in Figure 3.4.

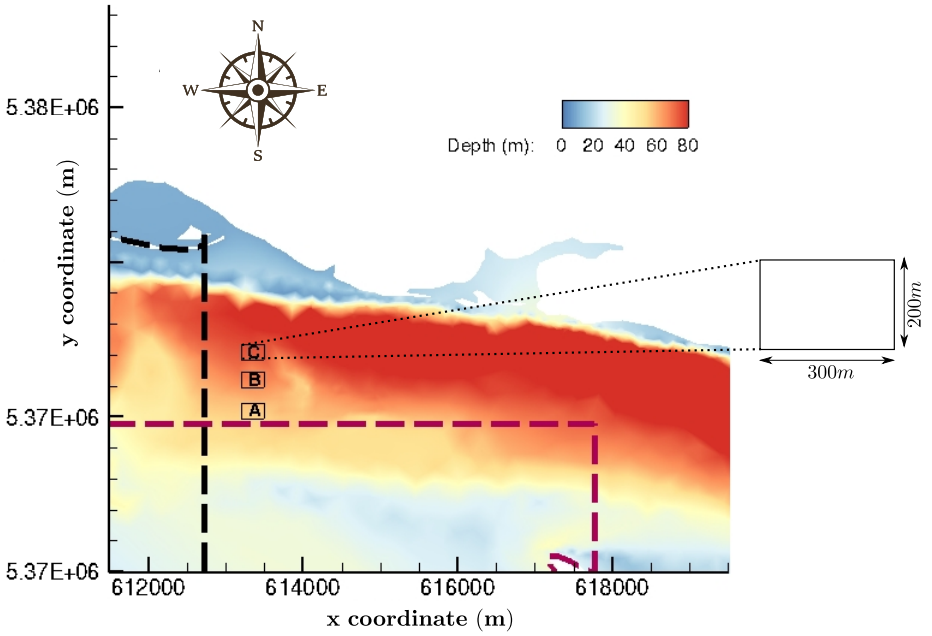

Figure 3.4. Map of the chosen zones for simulating farms in the Chacao channel labeled as A, B, and C, colored by the bathymetry. We also show a schematic of zone C dimensions, which are the same for zones A and B.

3.3.2 Bathymetry Characterization

To provide a physical basis for the size of the bathymetry's discretization, we study the local bathymetry of cases A, B, and C to understand the turbine-bathymetry interactions. While we have a high-resolution bathymetry of 10 m provided by Guerra et al. (2017), the resolution of our model will be coarser to avoid excessively high computational costs. The computational grid resolution resolves the dominant length scales in different directions. To recognize those scales and characterize the bedforms, we use the variogram method (Mark and Aronson, 1984) in 2-dimensions over the high-resolution bathymetry. A variogram, γ, provides the degree of linear scale dependency of a field and is defined as half of the variance between every point separated

by different distances, as follows:

$$\gamma(r) = \frac{1}{2N(r)} \sum_{i=1}^{N(r)} \sum_{j=i+1}^{N(r)} (Z_i - Z_j)^2 \tag{3.11}$$

where r is the distance between two points, N is the total number of points in a discretized domain, and Z is the surface elevation. In a log-log plot of r versus γ, we can observe that for small r, the variogram increases monotonically, meanwhile for $r > r_s$, the variogram converges to a saturation value, where r_s is the characteristic bedform length scale, that can be understood as the length where the structures are correlated, or as the predominant wavelength.

We can calculate variograms in different directions to study the level of anisotropy of the terrain. In other words, we can calculate all the points of a variogram by using a vector with a variable size, r, but with a fixed direction, θ. Figure 3.5 shows a schematic of a discretized bathymetry to explain how a 2-dimensional variogram works. In Figure 3.5 (i) we can calculate the sum of the differences in the elevation between the tails and the heads of the vectors with magnitude $r = r_1$, which will allow us to get one point of variogram in latitude 0^o (East direction). Another point of the variogram in latitude 0^o can be obtained by proceeding the same way, but using vectors with larger magnitude, $r = r_2$, as shown in Figure 3.5 (ii). The complete variogram in 0^o orientation is calculated by increasing k up to the entire domain size. Another variogram of the same bathymetry can be calculated by using vectors with a different orientation, as in Figures 3.5 (iii) and (iv), where we observe two different magnitudes of r for vectors with latitude $\theta = 45^o$ (North-East direction).

If the variograms of a surface calculated for different angles are identical, it means the terrain is isotropic. On the other hand, if there is a direction, θ where the variogram has a higher correlation than the others, then there is an anisotropy in that direction produced by features of the bed with a specific orientation. Figure 3.6

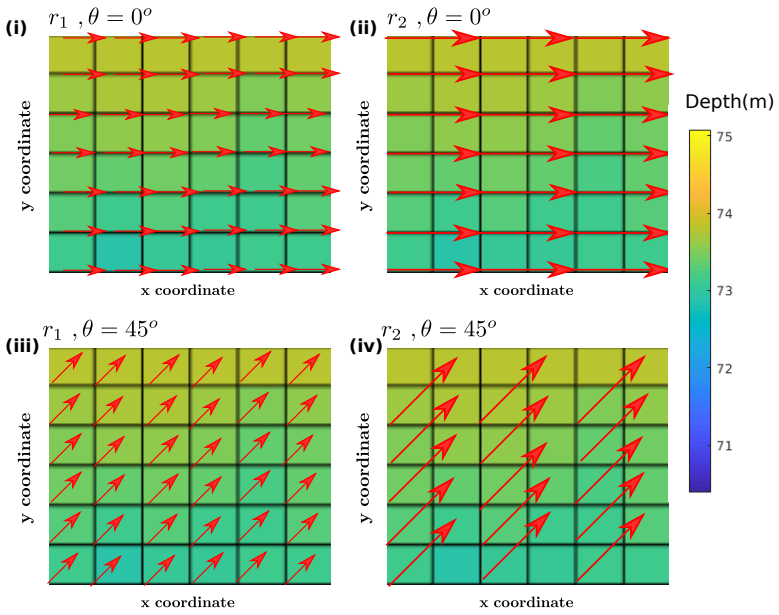

Figure 3.5. Scheme of the vectors used for calculating the directional variograms of a discretized bathymetry. (i) and (ii) are schemes of the vectors with magnitude $k = k_1$, and k_2, respectively, for calculating the variogram in latitude 0^o (East direction). (iii) and (iv) schemes of the vectors with magnitude $k = k_1$, and k_2, respectively, for calculating the variogram in latitude 45^o (North-East direction).

shows the variogram calculated in different directions for the zones A, B, and C in the Chacao channel, by using the high-resolution bathymetry data of 10 m. There, it is shown that the bathymetry for the cases A and B is slightly more correlated in the North direction (i.e., latitude 90^o); meanwhile, in zone C, latitude 90^o is the second that dominates. Those above were expected since the tides in the Chacao channel go from West to East and vice-versa (flood, and ebb tide respectively), which allows the bathymetry to be oriented in that direction.

Figure 3.6 also has information about the wavelength of the bedforms and their amplitude. For example, for cases A and B, the variograms in latitude 0^o show a length scale of around 150 m; however, after reaching the local maximum, we see an increase or decrease of the variograms, which is known as cyclicity (Gringarten and Deutsch, 2001). This cyclicity must be due to the size of the zones we are studying, which do not allow for the observation of larger dominant structures. In the other directions of cases A and B, there is no clear saturation value, which means the dominant wavelengths in those directions are larger than the farm size. In case C, we also observe cyclicity in latitudes 30^o and 60^o; however, for the latitude 0^o, we can see a visible wavelength of around 150 m. Regarding the amplitude of the bedforms, they are directly related to the variogram. Figure 3.6 tells us that the amplitude of case A is smaller than in case B, and they are smaller than in case C, just by observing the value of the variogram associated with the local, or global maximum associated with the dominant length scale.

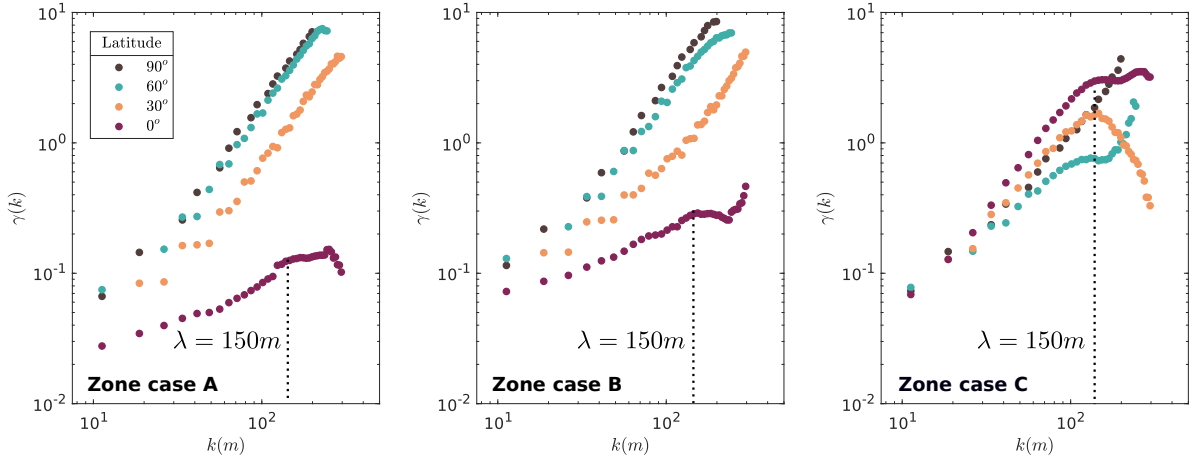

Figure 3.6. Variograms of the bathymetry of the simulated cases in the Chacao channel (marked in Figure 3.4), calculated in different directions, where 0^o corresponds to the East direction, and 90^o, to the North direction. The data set used for calculating them corresponds to the high-resolution bathymetric data (10 m)

With this information, we can design the computational grid around the farms such that we incorporate the main scales of the local bathymetry. As we see in the variograms, the smaller dominant length scale is equal to 150 m, so we can ensure that for a discretization equal or less than that value in x and y directions around the turbines we can represent the most relevant bedforms. In Figure 3.7 we show the FVCOM discretization of the entire domain with the high-resolution bathymetry data interpolated to the nodes. In the figure, we emphasize the elements we use in and around the zones with turbines, which are 100 m $\times$ 150 m.

In Figure 3.8, we show the high-resolution bathymetry with the interpolated bathymetry over the FVCOM grid (see Figure 3.7) in the longitudinal direction at the center span of the zones of cases A, B, and C. In the figure, we confirm we are using an appropriate resolution since the differences between the high-resolution (dashed lines) versus the grid resolution profiles (continuous lines) are smaller than the governing bedforms. We can also use Figure 3.8 to interpret the variograms, for example, in cases A and B, we can see that the bathymetry is nearly flat, which coincides with the fact that the bedform length scales are more extensive than the farm size. However, in case B we observe larger bedforms than case A, since, as we mentioned before, case B has a larger local maximum in the variogram, than case A. We also observe that case C has more fluctuations in the amplitude of the bedforms, which are around 5 m ($D/2$); meanwhile case B has fluctuations in the amplitude around 1 m ($D/10$) (see Figure 3.7). The last is consistent with the variogram that shows the largest amplitudes in latitude 0^o for case C.

We focus the variogram analysis in the longitudinal direction because it is the most relevant since the flow goes mainly through East and West along with the tides. Nonetheless, we also plot variograms in the other directions to corroborate that there are no larger dominant length scales we should take into account. Also, Peebles and Johnson (2015) performed numerical simulations of turbine arrays with different

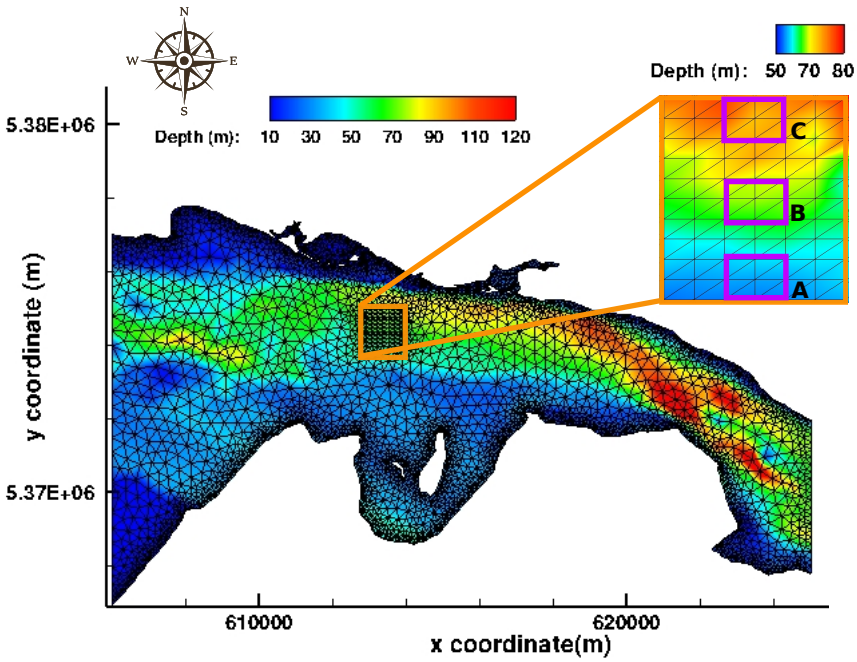

Figure 3.7. Discretized domain for the simulations with turbines in FVCOM for the Chacao channel, colored by the interpolated high-resolution bathymetric data. The zoom highlights the area where the turbines are simulated; there, every element has a height of 100 m and a width of 150 m. The rectangles in purple indicate the exact area of zones A, B, and C. The legend at the left corresponds to the bathymetry of the entire domain; meanwhile, the legend at the right, belongs to the bathymetry of the zoomed area.

bottom slopes that showed that lateral sloping has a negligible impact over turbine arrays performance. In their simulations, Peebles and Johnson (2015) showed that farms with a longitudinal slope of around 5^o have a net thrust force increment over 100% compared to a flat bottom, while a lateral slope of around 13^o, has an increment less than 5% in the net force.

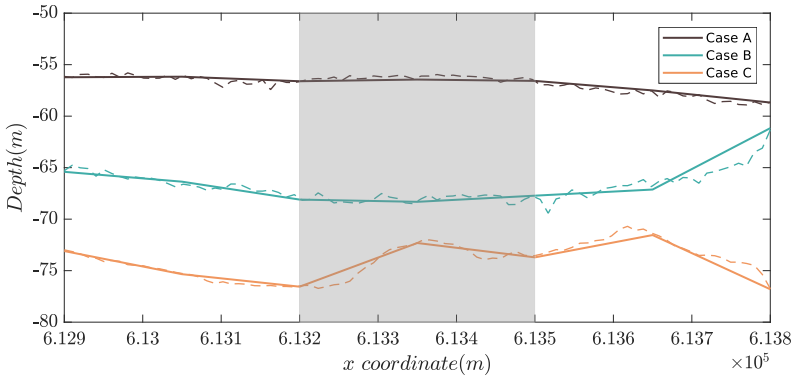

Figure 3.8. Bathymetry at the center-span of the zones of cases A, B, and C. In continuous line, is the bathymetry used for the simulations. In dashed lines, is the high-resolution bathymetry taken from Guerra et al. (2017) every 10 m. The zone occupied by the farms is marked in gray.

3.3.3 Simulation Cases

The farm we simulate has a total of 27 devices distributed in a staggered configuration because it is more efficient than an aligned distribution (Daskiran et al., 2015; Markfort et al., 2012; Wu and Porté-Agel, 2013). The turbines have a diameter of $D = 10$ m, and the center is located 12 m from the bottom. Each farm contains three rows of five turbines, interspersed with three rows of four turbines, as shown in Figure 3.9. With these characteristics we get a $C_{tFarm} = 1.12$ by using Equation 2.9

from Chapter II. A summary of the simulation inputs is presented in Table 3.1.

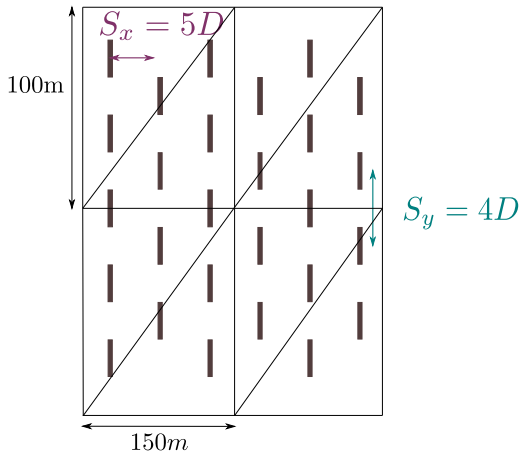

Figure 3.9. Scheme of turbines distribution for cases A, B, and C, where S_x is the distance between rows, and S_y, the lateral distance between the center of the disks. Black lines show the computational grid used in FVCOM for representing the farms, which are the same purples rectangles highlighted in the zoomed area of Figure 3.7.

TABLE 3.1

MAIN VARIABLES FOR THE SIMULATED CASES IN FVCOM

Parameter	Value
Turbines diameter (D)	10 m
Hub height (z_{hub})	12 m
Thrust coefficient C'_{tFarm}	1.12
Longitudinal disk separation (S_x/D)	$5D$
Lateral disk separation (S_y/D)	$4D$
$\overline{H}/z_{hub}$ case A	4.7
$\overline{H}/z_{hub}$ case B	5.6
$\overline{H}/z_{hub}$ case C	6.2
Simulation time	45 days
Bottom roughness (z_0)	40 mm
Grid nodes	$4,164$
Sigma layers	10

3.4 Results

Below, we show the results of numerical simulations in the Chacao channel without devices (case 0), and with devices (cases A, B, and C). We run each of the cases independently for a simulation time of 45 days and using the same boundary and initial conditions.

Here we present the changes in the velocity, TKE, and bottom shear produced by the turbines. We observe not only the effects in the flow inside the farms, but also

the consequences of the turbines downstream. Finally, we show how the theoretical power of the farms change according to their location in the channel.

3.4.1 Chacao Channel Simulations Without Turbines

To know the conditions before installing turbines, we run numerical simulations of the Chacao channel without devices, and then, we average the results depending on if they belong to flood or ebb regime; the flood regime is defined as all the periods when the flow goes from West to East; meanwhile, the ebb regime occurs when the flow goes from East to West. We have to highlight that we call "upstream of the farm" the West side of the farm during the flood regime, and the East side of the farm, during the ebb regime.

Figure 3.10 shows the velocity in the zone of cases A, B, and C before, incorporating the farms of turbines. All the profiles are at the center span of every zone, and a distance from the bottom equal to the hub height. In the figure, we observe that for all the cases, the average velocity is over 0.7 m/s. As we mention before, we observe an asymmetry between the ebb and flood regimes; at the beginning of the farm zones, all the cases have a higher velocity intensity in the ebb regime; however, inside the farm zone, case C shows a higher intensity for flood regime. Another aspect to notice is in the flood regime, the incidence velocity in the C case zone is more than a 12% higher than the other cases; meanwhile, all the cases have a negligible effect on the ebb regime difference between them.

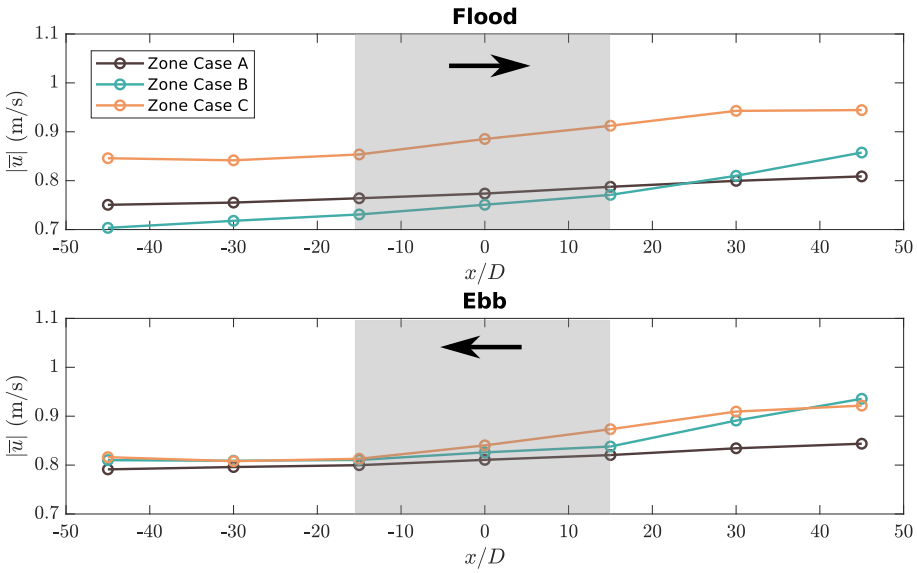

Figure 3.10. Absolute velocity in the streamwise direction, u, at the hub height, before simulating turbines in zones A, B, and C (see Figure 3.4). The profiles are located at the center span of every zone. In the streamwise direction, the profiles go from $45D$ upstream to the center of the farm location ($x/D = 0$), to $45D$ downstream. The gray areas indicate the location of the farms in the next simulations; meanwhile, the black arrows indicate the flow direction.

The direction of the flow is also related to the energy that can be extracted by MHK devices, and our C_{tFarm} model is designed for flows nearly aligned to the turbine axis. Figure 3.11 show the velocity angle before simulating the turbines, where 0^o corresponds to a constant latitude. We observe that all the cases have a misalignment less than 6^o, except in the case C for the flood regime that shows a misalignment of around 8^o, which does not cause significant differences with respect to a 0^o flow (Frost et al., 2017; Musa et al., 2020).

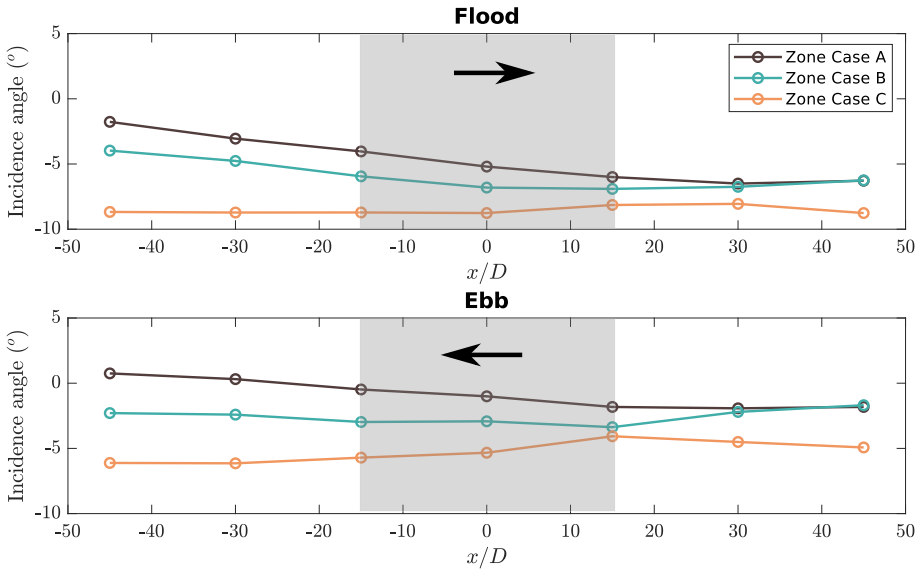

Figure 3.11. Incidence angle of velocity, at the hub height, before simulating turbines in zones A, B, and C (see Figure 3.4). The profiles are located at the center span of every zone. In the streamwise direction, the profiles go from $45D$ upstream to the center of the farm location ($x/D = 0$), to $45D$ downstream. The gray areas indicate the farms' location; meanwhile, the black arrows indicate the flow direction.

Regarding the initial modeled TKE (refer to Equations 3.5 and 3.6), in Figure 3.12, we observe profiles at the center span of every zone, at the height of the top turbine since that is the most affected area when the devices are installed. The figure depicts that for the flood regime, case C has the highest TKE, and case A has the lowest; however, in the ebb regime the opposite occurs. The last is explained by the asymmetric morphology of the channel that produces different interactions with the coast for both regimes.

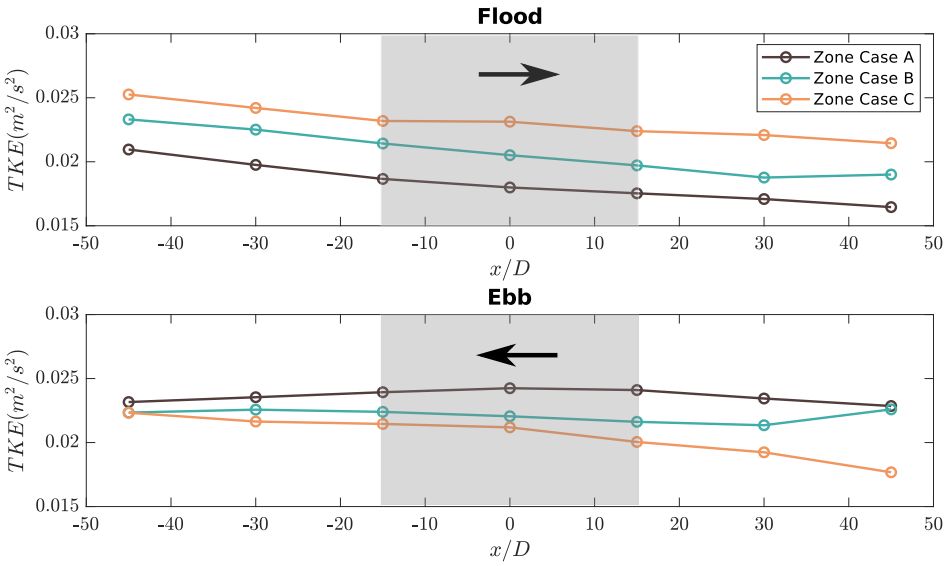

Figure 3.12. Modeled TKE at the top turbines height before simulating them in zones A, B, and C (see Figure 3.4). The profiles are located in the center span of every zone. In the streamwise direction, the profiles go from $45D$ upstream to the center of the farm location ($x/D = 0$) to $45D$ downstream. The gray areas indicate the location of the farms in the next simulations; meanwhile, the black arrows indicate the flow direction.

From the FVCOM simulations we can obtain the resolved shear stress at the bed, τ_b, as follows:

$$(\tau_{bx}, \tau_{by}) = C_d \sqrt{u^2 + v^2}(u, v) \tag{3.12}$$

where the drag coefficient, C_d is determined as

$$C_d = max\left(\frac{\kappa^2}{\ln\left(\frac{z_{ab}}{z_0}\right)^2}, 0.0025\right) \tag{3.13}$$

here, $\kappa = 0.4$ is the von Karman constant, and z_0 is the bottom roughness parameter,

which is equal to 40 mm in all the simulations we run. Finally, z_{ab} is the height of the first sigma layer above the bottom, which is around 3 m for the zone A, 3.5 m for the zone B, and 4 m for the zone C.

While we use the same bottom roughness, z_0, for all the domains, that does not necessarily imply all the cases have the same shear at the bottom. The bed stress τ_b depends on the local velocity and the distance of the first sigma layer from the floor (see Equations 3.12 and 3.13). Although we obtained a unique value of z_0 from a previous calibration with real data, we acknowledge that this parameter can change along the channel; however, we use the same value for the three cases to compare the effect of the bathymetric features.

Figure 3.13 shows that the shear at the bottom in the flood regime is different among the cases; at the beginning of the farms the differences are over 10%. On the other hand, at the ebb regime, the differences among cases are negligible. In the figure, we can also observe that, in this study case, the bottom shear is not related to the bedforms since case A is the flattest; however, at the beginning of the farms, its bottom shear is between cases B and C, for ebb and flood. With the results shown in Figure 3.13 we corroborate that the shear is different among cases despite using the same roughness z_0 in the entire domain for all the simulations.

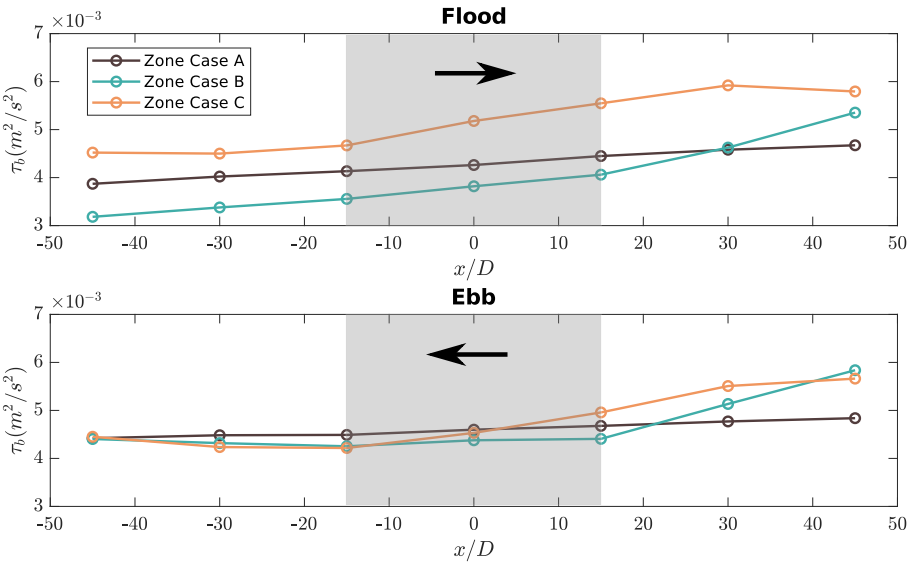

Figure 3.13. Bottom shear, τ_b before simulating the turbines in zones A, B, and C (see Figure 3.4). The profiles are located in the center span of every zone. In the streamwise direction, the profiles go from $45D$ upstream to the center of the farm location ($x/D = 0$) to $45D$ downstream. The gray areas indicate the location of the farms in the next simulations; meanwhile, the black arrows indicate the flow direction.

3.4.2 Chacao Channel Simulations With Farms of Turbines

Below, we present the changes in the flow caused by the farms by comparing the cases with devices with the base case. In this section, we calculate the absolute change, which is the direct subtraction between the cases with turbines minus the base case. Additionally, we calculate the percentage change, which is the absolute difference between the cases with turbines and without turbines normalized by the base case, and then multiplied by 100. In other words, a percentage change equal to 100% means the variable duplicates its value with respect to the base case. The reason for using the percentage change is to normalize cases A, B, and C, and compare them despite their initial conditions.

In Figure 3.14, we show the difference in the velocity with respect to the base case in m/s, in slices that pass through the farms' center. There, we observe that we are able to capture the velocity deficit produced by the turbines in all the cases. The figure depicts that the wakes are different among the cases in direction and magnitude even though the simulated farm is the same. For example, the wakes for cases A and B are nearly straight; meanwhile, the wakes for case C show a slight deviation of less than 10^o for ebb and flood. Additionally, Figure 3.14 shows than the cases with higher undisturbed velocity (see Figure 3.10), has a higher absolute velocity deficit, which is in agreement with the results of Guillou and Thiébot (2016).

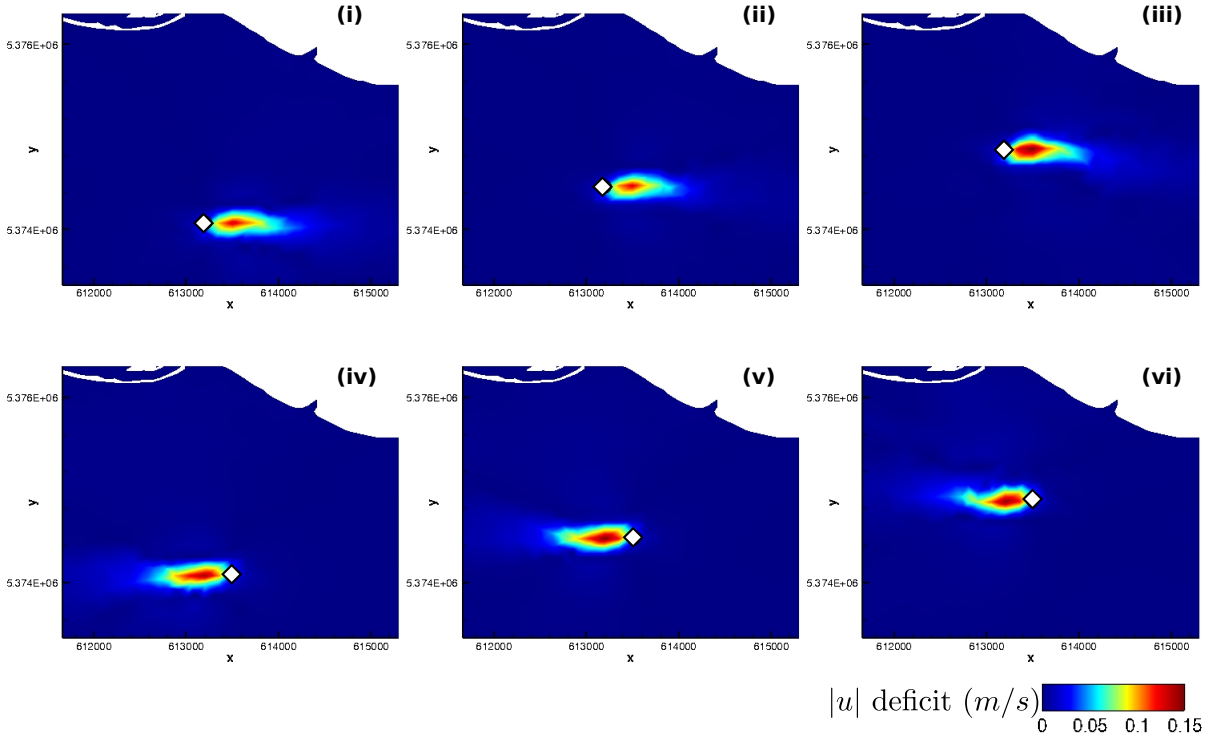

Figure 3.14. Slices at farm center coloured by the absolute velocity deficit in the streamwise direction, in m/s, with respect to the results of case 0. (**i**), (**ii**), (**iii**) are cases A, B, and C, respectively for the flood regime. (**iv**), (**v**), (**vi**) are cases A, B, and C, respectively for the ebb regime. White diamonds indicates the center of the farms.

To study the averaged velocity we also calculate the percentage of velocity deficit for each case at the hub height, and the farm center span. In Figure 3.15, we show that the highest deficit occurs just at the end of the farm for all the cases, and is around 15% to 20%. The figure also shows that there are no considerable differences in the percentage deficit inside the farms, nor the maximum between the cases.

Then downstream, Figure 3.15 shows that all of the cases reach a wake recovery of 95% around $45D$ to $60D$ downstream the end of the farms for the flood regime, and $50D$ to $65D$ for the ebb. This distance seems more significant compared to the around $30D$ for the wake recovery of one device shown in the literature (Aghsaee and Markfort, 2018; Myers and Bahaj, 2010); however, we can find studies of wakes that last more than $100D$ for farms of turbines (Eriksson et al., 2017; Fitch et al., 2012). In Figure 3.15 we can also observe that case A has a higher percentage of velocity deficit than the other two cases, which lasts up to $65D$ downstream for flood, and it is seen between $50D$ to $85D$ downstream the end of the farm for the ebb regime.

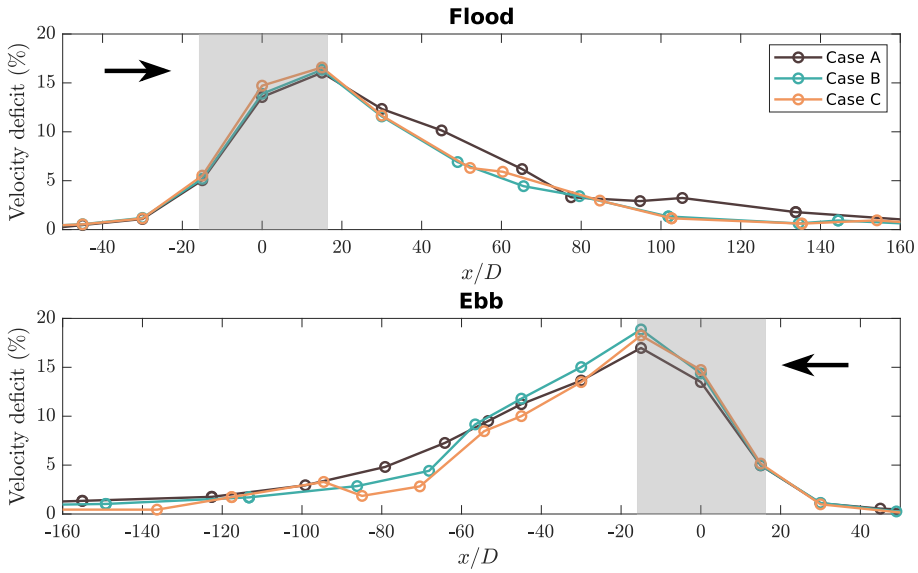

Figure 3.15. Percentage of the absolute velocity deficit in the streamwise direction, u, at the farm center height, and farm's center span, due to the device's installation. The 100% are the results of case 0 in the same location as the other cases. The location of the farms is highlighted in gray; meanwhile, $x/D = 0$ is the center. The black arrows indicate the flow direction.

If we compare Figure 3.14 with Figure 3.15, we can observe some differences in the results. On the one hand, we can see that for cases A and B, the absolute difference (Figure 3.14), and the percentage deficit (Figure 3.14) follow the same tendency, i.e., both have more intensity for ebb than for flood. On the other hand, case C shows a higher intensity in the percentage difference for ebb than flood; meanwhile, in the absolute difference, we see a stronger wake for the flood than for ebb. The aforementioned is not a contradiction since the percentage deficit is the change in velocity normalized by the local undisturbed velocity, and here is calculated to compare the cases to each other. However, to compare the real magnitude of the local effects of a farm, it is more important to observe the absolute deficit.

The study of the TKE is quite different to the velocity since we cannot reproduce the increment of the turbulence in the near-wake, as we mention in Section 3.2; however, we are still able to reproduce the location of the maximum increment, and the magnitude beyond $8D$ downstream the farms of TKE (Kasmi and Masson, 2008; Li et al., 2017). In Figure 3.16, we show the percentage increment in the modeled TKE caused by the farms at the farm's center span and the top of the height of the turbines (where the most significant changes occur). The figure shows that the maximum change in TKE occurs at the end of the farms for all the cases, the same as the velocity deficit.

In Figure 3.16 we can also see that the percentage of TKE increment is considerably higher for case A than for the other cases, in both regimes. The last is striking since case A is the one with the highest initial TKE for flood and the lowest for the ebb. Although we acknowledge we cannot reproduce the magnitude of TKE with precision inside the farm, we can recognize which farm has the highest increment, and in which location.

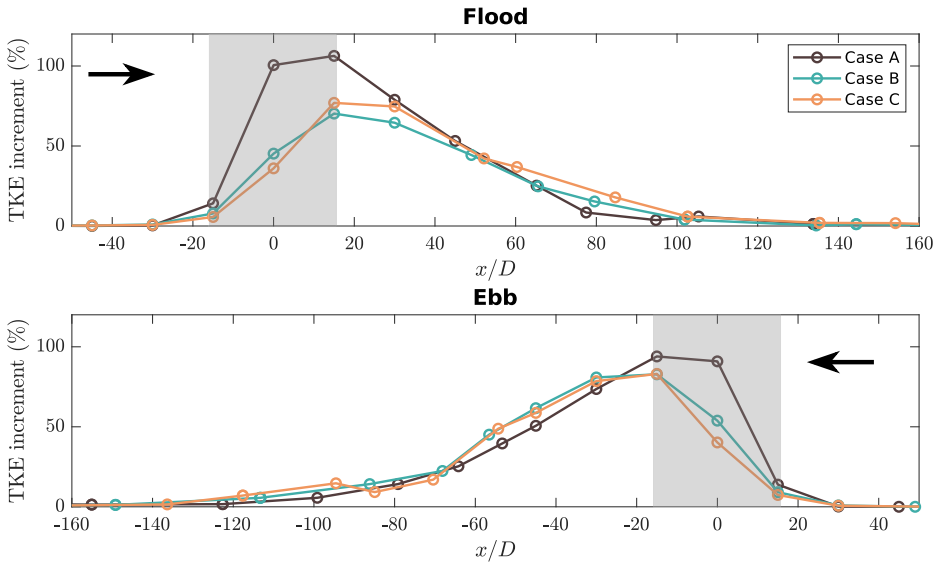

Figure 3.16. Percentage of modeled TKE increment at the height of the top turbines, and farm center span, due to the device's installation. The 100% are the results of case 0 in the same location as the other cases. The location of the farms is highlighted in gray; meanwhile, $x/D = 0$ is the center. The black arrows indicate the flow direction.

Regarding the shear at the bottom, in Figure 3.17 we see that the percentage deficit of τ_b is similar inside the farm among the cases in both regimes, even though the initial condition for the flood regime show an around 10% of difference between cases. We propose that the similarity of the bottom shear deficit is not because we use the same z_0, but because the devices have the same hub height, z_{hub}. We also have to mention that Guillou and Thiébot (2016) show that the deficit of bottom shear in terrain with turbines decreases when the z_0 increases.

Figure 3.17 also shows a positive percentage deficit of τ_b, which has been seen in other studies (Guillou and Thiébot, 2016; Thiébot et al., 2015). The reduction in the bottom shear is a consequence of the velocity reduction in the area of the farms.

However, as Li et al. (2017), the shear stress should increase in 3-D models since they can capture the acceleration of the flow under the devices, contrary to 2-D models that only calculate the vertical average velocity deficit. Following those mentioned above, we performed another simulation with the same conditions but with an improved vertical resolution to see if we capture any acceleration under the turbines that produces a negative deficit of τ_b. The new simulations show that duplicating the vertical resolution barely changes the vertical profiles of velocity and TKE (see Appendix A). The above suggests that the vertical resolution is sufficient, but probably the devices are too close to the bottom to capture a considerable acceleration under them.

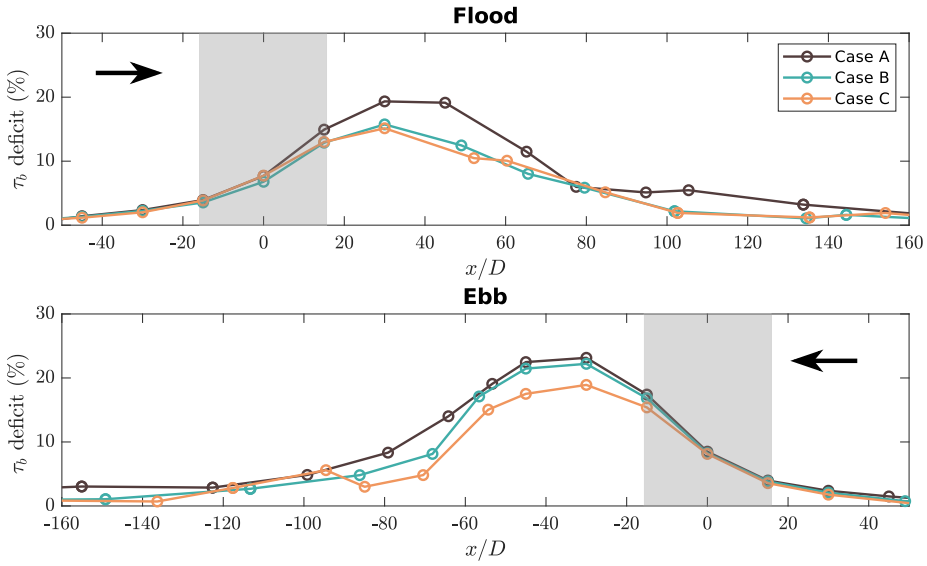

Figure 3.17. Percentage of bottom shear stress, τ_b, deficit, due to the farms installation, at the farm center span. The 100% are the results of case 0 in the same location of the other cases. The location of the farms is highlighted in gray; meanwhile, $x/D = 0$ is the center. The black arrows indicate the flow direction.

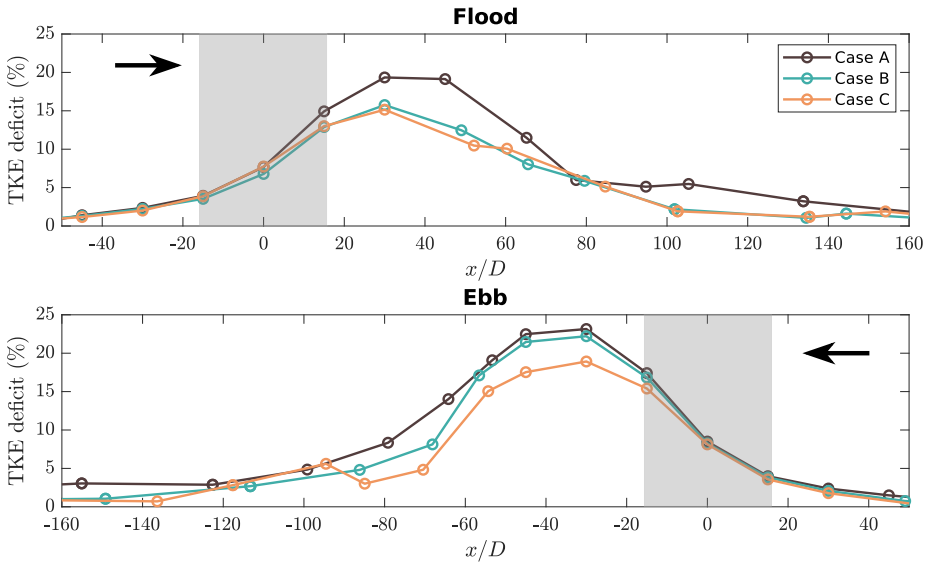

Figure 3.18. Percentage of modeled TKE deficit at the bottom, and farm center span, due to the farms installation. The 100% are the results of case 0 in the same location of the other cases. The location of the farms is highlighted in gray; meanwhile, $x/D = 0$ is the center. The black arrows indicate the flow direction.

In Figure 3.17, we can also see that the peak of percentage bottom shear deficit occurs around $15D$ downstream of the farm, where case A reaches the maximum deficit of τ_b among the cases. To study these differences, we plot the turbulent kinetic energy at the bottom, since the shear is one of the sources of TKE. In Figure 3.18 we see that, unlike the TKE at the top of the turbines, the TKE at the bottom decreases with the devices. Particularly, we can observe that all the cases have the highest TKE deficit downstream of the farm, which coincides with the location of the highest τ_b deficit.

Finally, to study the entire performance of all the cases, we calculate the averaged theoretical extractable power, $\overline{P}$, by using different control volumes around each farm. Figure 3.19 shows that the power is larger in the ebb regime than in flood for cases A and B; meanwhile, in case C occurs the opposite. We also observe that case C has

the highest power for the flood regime, and case A has the highest ebb regime.

In Figure 3.19, we also observe that the average power normalized by the water density, $\overline{P}/\rho$ is $O(10^3)$ for all the cases in both regimes. If we consider the water's density is $\rho \approx 1,000 kg/m^3$, we would obtain an average extractable power of roughly $1MW$. However, in the calculation, we are not taking into account the devices' capacity or efficiency, which would result in an even smaller power.

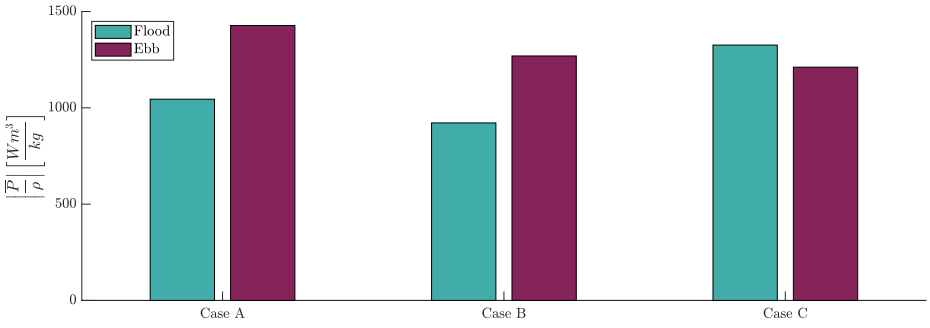

Figure 3.19. Theoretical extractable power, P, of cases A, B, and C, in flood, and ebb regime.

3.5 Discussion

Comparing the scenarios with and without turbines, we observe that the velocity inside the farms, has a similar percentage deficit between the cases despite the differences in the initial velocity. On the other hand, downstream the farms we observe that case A has a wake that recovers slower than the other cases, particularly in the flood regime. The last can be explained by the low input TKE of case A in the flood regime (see Figure 3.12) since low TKE implies a decrease in the mixing, and consequently, a slower wake recovery. We also observe that the initial velocity incident

angle also has no relation with the wake downstream the farms (considering that all the cases have an incident angle less than 8^o). The last is observed in the wake of the farm in case C that shows a similar misalignment for ebb and flood; however, the inlet incident angle shows a considerable misalignment only for flood regime (see Figure 3.11). Instead, we suggest that the closeness of case C to the coastline affects the wake direction downstream of the farm. Nonetheless, the proximity of the coast is not enough to notice a significant flow acceleration around the farms (see Figure 3.14).

The percentage change of TKE has different behaviors; it increases at the top of the disks and decreases at the bottom of the channel. On the one hand, the TKE increment occurs because of the shear layer at the top of the disks. This layer causes instabilities that are not affected by the surface due to the depth of the devices. In the results, we observe that case A has the most elevated percentage TKE increment, which implies that in that case, the farm disturbs the ambient turbulence more than in the other cases. The last is the consequence of the higher perturbation that the turbines represent in a smooth terrain for both regimes.

On the other hand, the TKE at the bottom decreases the same as the shear, which is produced by the reduction of the velocity below the devices. The TKE and the shear at the bottom are directly related since τ_b acts as a source of TKE. Inside the farms, the percentage changes of both variables are similar among the cases, probably because the distance of the devices over the bottom is the same. However, downstream the farms, we observe differences: case A has the highest percentage deficit of TKE and shear at the bottom, and case C has the lowest. We do not observe a relation between the initial conditions that explain the differences in the bottom shear downstream cases A and C. Nevertheless; we could say that flatter bathymetries exert less resistance to the flow near the bottom, so the resistance that the turbines generate is more significant than in a rough bathymetry as in case C.

To study the changes in the bottom shear it is relevant to predict the modifications in the sediment transport, even though we do not use the FVCOM sediment module. We acknowledge that the erosion/deposition is a complex process that depends on the sediment characteristics and the bottom shear. However, with the fluctuations in τ_b we can recognize which zones are more likely to have erosion, and which ones, deposition. Figure 3.20 shows the difference in the bottom shear of the base case minus the case A, for the flood and ebb regimes. We observe that the turbines would cause a sediment deposition downstream the farm that would be more noticeable from the farm ends to around two times the farm size downstream. The last is consequent with the experiments of Hill et al. (2016) which showed that the sediment is accumulated downstream of two turbines aligned one behind the other; however, they also showed an erosion in the very near wake (less than $3D$) of the upstream device, which is smaller than our horizontal resolution, so it is not captured by our simulations. We also observe in Figure 3.20 a slight decrease in the bottom shear at the sides of the farms, which would trigger an erosion process in the area.

Finally, we calculate the theoretical averaged power, $\overline{P}$, of each farm to observe how the location can alter this variable. The results show that power is directly related to the initial conditions. For example, we see that the cases with higher initial velocity in one regime show greater $\overline{P}$ in the same regime after simulating the turbines (i.e., cases A and B have higher $\overline{P}$ for ebb than flood; meanwhile in case C occurs the opposite). The last is also observed in the wake downstream of the farms shown in Figure 3.14.

Regarding the relation between $\overline{P}$ and TKE, we observe that the most significant increment in $\overline{P}$ occurs in case C for flood, and in case A for ebb which are the cases with higher initial TKE for flood, and ebb, respectively. Those above explain the more available energy, the more power a farm can extract.

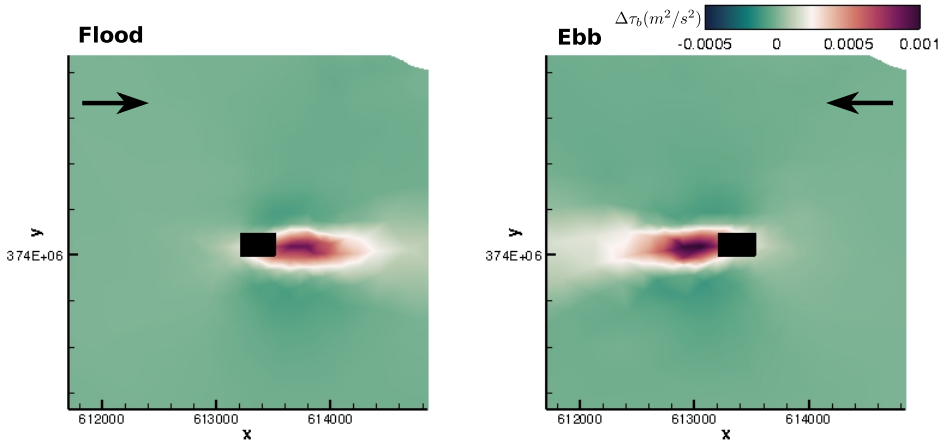

Figure 3.20. Difference in the bottom shear, $\Delta\tau_b(m^2/s^2)$, caused by the farm installation in case A, where a positive difference implies a decrease in the bottom shear. Right figure corresponds to the flood regime, and left figure, to the ebb. Black rectangles indicate the area occupied by the turbines; meanwhile the arrows indicates the flow direction.

3.6 Summary

In this Chapter, we looked for representing farms of MHK turbines in a real tidal channel by using a parameterization from a high-resolution model. For that, we ran numerical simulations using the ocean circulation model FVCOM to represent MHK farms in the Chacao Channel, Chile. For simulating the farms, we used an extension of FVCOM provided by Murray and Gallego (2017), which is based on the momentum sink approach, and that we modified to represent the specific characteristic of the group of devices, such as the lateral and longitudinal separation. To include those specific features of the farms in the resistance force, we used the thrust coefficient, C_{tFarm}, we derived from a high-resolution model, where we represented every device with more than one node (see Chapter II).

The first simulation consisted of running a base case without turbines to represent the undisturbed conditions of velocity, TKE, and bottom shear in the Chacao channel. We used those simulations to choose three suitable places to install a farm

of turbines based on the operation range of depth and velocity of a specific commercial MHK device. The purpose of choosing three different locations, which we called cases, is to observe how our parameterization works under different local conditions of flow and bathymetry.

Before running the simulations with turbines, we characterized the local bathymetry of the three cases, for which we used the variogram method. The variogram shows the scale where the bedforms are related and the zones with a larger amplitude. In the streamwise direction, we observed that the cases had different length scales and amplitudes. The first case had the largest length scale and was the smoothest one. The second case had bedforms with amplitudes of around $D/10$. Finally, the last one had the smallest length scale, and more bedform irregularities, with amplitudes around $D/2$. This information was relevant for two reasons: one is to design a computational mesh representing the most relevant bedforms; on the other hand, we could interpret the changes in the flow and relate them with the local bathymetry.

We ran the three cases with a finite-sized farm with devices distributed in a staggered way. All the simulations were run independently by using the same initial and boundary conditions. The hub height was 12 m over the bottom for all the devices; however, not all of them had the same depth. We have to highlight that we could use C_{tFarm} to represent these turbines because we met the conditions: to represent medium-sized staggered farms, with a ratio $z_{hub}/H > 4.7$.

With the results, we calculated the absolute changes produced by the farms of turbines, which depicted that cases with higher initial velocity had a more significant change in the same variable. Meanwhile, the theoretical extractable power, showed that the farms with higher inlet velocity in one regime had a greater $\overline{P}$ in the same regime. Finally, we observed that the cases with the highest theoretical $\overline{P}$ coincided with the ones with a larger initial TKE.

We calculated the percentage change of velocity, TKE, and bottom shear, because

of this way, we made those variables independent of the initial conditions so that we could compare each other. We acknowledge that the horizontal resolution of our model was around $10D$ inside the farms, so we barely had a couple of nodes there; however, with the bathymetry's characterization, we could ensure we represented the dominant bedforms. With the results, we observed that local bathymetries with bedforms smaller than the turbines' diameter could affect the percentage difference of velocity, TKE, and bottom shear that can last further $100D$ downstream the farm. In particular, flatter bathymetries can have a higher percentage change in TKE and bottom shear considerably.

We also observed that the velocity deficit of cases with flatter bathymetries and low initial TKE recovers slower and have a higher percentage increment of TKE at the top of the disk, probably because the turbines alter the ambient turbulence more than in cases with larger bedforms. At the bottom of the channel, contrary to the top of the disks, the TKE decreased with the bottom shear, τ_b. We observed that rougher bathymetries with bedform amplitudes around $D/2$ had a lower percentage of τ_b deficit since the presence of the turbines means less flow resistance that in flatter bathymetries.

Another variable we analyzed is the probable effects of the turbines over sediment transport. Even though we did not simulate the sediments, we could predict the zones likable to have erosion or deposition by observing a positive or negative deficit of τ_b, respectively. We noted that we were not capable of capture the erosion in the near-wake of the turbines because of the grid resolution; however, we captured the deposition in the far-wake and erosion in the lateral sides of the farms.

In this work, we incorporated a parameterization from a high-resolution model into an OCM for representing the characteristics of a finite farm of turbines in a specific environment. Using a modified version of the actuator disk approach, we could represent the flow under and over a finite farm of MHK devices in different

locations of the Chacao channel. We also observed how the effects over velocity, TKE, and bottom shear downstream of a farm could be very different according to its location. With our results, we give more insights to predict and mitigate the impacts of installing a farm in a determined location. Future works should be focused in to simulate turbines farthest to the bottom to observe if the initial conditions and bathymetry are affected to the same extent. Additionally, to run higher devices could be useful to see if it is possible to capture the acceleration under them , and the increase in the bottom shear.

CHAPTER 4

CONCLUSIONS

At the beginning of this work, we proposed that adopting a multiscale approach, we can use a high-resolution model to derive a parameterization for marine hydrokinetic (MHK) devices and represent farms of turbines with realistic tides and bathymetry in ocean circulation models (OCM).

In Chapter II, we used the high-resolution model DES (Detached eddy simulations) coupled with the actuator disk approach to simulate every device in farms with different depths and horizontal distribution. With the results, we were able to recognize the variables that dominate the resistance force of a particular group of turbines. Using those dominant parameters, we propose a parameterization, C_{tFarm}, which is a thrust coefficient representative of an entire farm of turbines that considers the devices' lateral separation and the number of rows.

In Chapter III, we use the ocean circulation model, FVCOM, to represent the flow in the Chacao Channel, Chile. We used as input the tides of the zone and a high-resolution bathymetry of 10 m. After recognizing the base conditions, we could represent a finite farm of turbines, using the momentum sink approach provided by Murray and Gallego (2017), and improved by incorporating the parameterization, C_{tFarm}. With the parameterization, we could integrate a specific farm of turbines in the model in different locations of the Chacao channel.

After completing the research, we conclude that our hypothesis was correct; we could utilize a multiscale approach to parameterize the resistance force of an entire farm of turbines at the wakes' scale, and then incorporate it into a model at tides'

scale. This way, we can easily calculate the resistance force of a specific finite farm of turbines that can be used in any location, considering the devices' distribution, and the number of rows, but without simulating each device.

4.1 Thesis Summary

In this work, we carried out a multiscale analysis for representing farms of marine hydrokinetic (MHK) devices in a real tidal channel using an ocean circulation model (OCM). The reason of using a multiscale analysis for representing farms of turbines is because the resolution of the OCM does not allow to represent every turbine per node, so what is commonly done is to multiply the force of one turbine by the total number of the devices in a cell, which is not precise. In addition, the current works use to represent huge farms that can exceed hundreds or thousands of devices, which is not realistic, given the level of development of MHK devices' technology. For the reasons mentioned above, before using an OCM, we need to use a high-resolution numerical model, to represent every turbine and understand the wakes' interactions in a finite farm. First, we studied the interaction of the devices' wakes with the flow and each other using the high-resolution model at the wakes' scale. With that model, we obtained a parameterization of the resistance force for an entire farm of turbines with different configurations (Chapter II). Later, we simulated a farm of turbines in a real tidal channel, for what we used the OCM, FVCOM, where we incorporated the parameterization we previously derived (Chapter III).

The location we chose to represent farms of turbines was the Chacao channel, Chile, characterized by having high velocities due to the sea narrowing between the continent and Chiloé Island. This place has plenty of advantages for marine energies, such a closeness to the electrical grid and an appropriate depth for the disk installation. However, before installing MHK devices, it is necessary to evaluate the negative impacts over some variables such as the velocity, turbulent kinetic energy (TKE),

and bottom shear (τ_b) since they can modify the morphology and the ecosystem.

In Chapter II, we looked to study the wakes' interaction inside a farm to obtain a parameterization of the resistance force that considers the disk's distribution. For this part of the work, we needed to use a high-resolution model, able to represent every one of the devices. For the flow solver, we used the hybrid turbulence model, DES; meanwhile, we used the actuator disk approach for the disks' representation. Both DES, coupled with the actuator disk approach, was validated with laboratory measurements in the same Chapter. We simulated different turbines distributions, and depths to identify the dominant variables in the resistance force, and to proposed a new thrust coefficient, C_{tFarm}. With the simulations' time-averaged results, we used different control volumes around the farms to calculate the value of C_{tFarm} for each case. After that, we observed that C_{tFarm} depends on the lateral distances for farms with two rows and lateral and longitudinal distances for farms with more than two rows. However, we have to highlight that our expression is only valid for farms with a staggered distribution, almost perpendicular to the mean flow, and are deep enough, so they do not interact with the free-surface. This Chapter is of vital importance for Chapter III since the use of C_{tFarm} improves the representation of farms of turbines, so the simulations of devices in the Chacao channel can be more realistic.

In Chapter III, we simulated a finite farm of turbines with 27 devices in the Chacao channel by incorporating to FVCOM the momentum sink approach provided by Murray and Gallego (2017), and improved by the use of our parameterization, C_{tFarm}. Before simulating the turbines, we ran a base case to choose three suitable locations for installing a farm, according to the operational rages of a particular MHK commercial device with a diameter,$D = 10$ m, and a hub's height, $z_{hub} = 12$ m. The reason for choosing different locations was to study how the local and initial conditions can affect the wakes' dynamics of the same farm. For all the simulations, we used realistic tides as boundary conditions, and we interpolated a high-resolution

bathymetry data of 10 m into the computational grid. After choosing the three locations, we characterized the local bathymetry by using the variogram method to relate changes in the flow according to the different bathymetries and to design a computational grid that represents the most dominant bedforms on the farm. The bathymetry characterization shows that one of the cases has a nearly flat bathymetry, another case has amplitudes around $D/10$, and the last case is the rougher with amplitudes around $D/2$. After running three independent numerical simulations of the same farm located in different places, and the same boundary conditions, we studied the changes in velocity, TKE, and bottom shear because those variables can affect the morphodynamics and the ecosystems.

After simulating the three cases independently, we observed that, even though we used the same farm, the velocity, TKE, and bottom shear are affected differently according to the initial condition and the local bathymetry. To compare the cases with each other, we calculated the percentage change to normalize the fluctuations in the mentioned variables by the conditions shown in the base case. The percentage change showed that cases with smoother bathymetries and low initial TKE at the top of the disks have a slower wake velocity recovery. We also observed that the TKE behaves differently at the top of the disks and the channel's bottom. At the top, the percentage of TKE increases, where its value is higher in cases with smoother bathymetries because the effect of the turbines alters the ambient turbulence more than in cases with larger bedforms. At the bottom of the channel, the TKE decreases with the bottom shear. There, we observed that rougher bathymetries with bedform amplitudes around $D/2$ have a lower percentage of τ_b deficit since the presence of the turbines means less flow resistance that in flatter bathymetries.

Another variable we analyzed was the probable effects of the turbines over sediment transport. Although we did not simulate the sediments, we could predict the erosion/deposition according to an increasing or decreasing of τ_b, respectively. We

noted that we were not capable of capturing the erosion in the near-wake of the turbines, presumably because of the lateral grid resolution; however, we captured the deposition in the far-wake and the erosion in the lateral sides of the farms. With the percentage deficit, we observe that inside the farms, this variable is equal for all the cases, probably because the height of the devices from the bottom is the same. Downstream the farm, the percentage deficit depicts that flatter bathymetries are more likable to have a percentage increase in the sediment.

Besides studying the percentage change, we also analyzed the absolute difference between the cases with and without turbines. While the percentage change is useful to compare the cases with each other, the absolute change gives information about the real magnitude of the variations product of the farm. With the simulations results, we observed that cases with a more significant initial velocity and TKE have a larger absolute difference of those variables, no matter the bedforms amplitudes (as long as the amplitudes are less than $D/2$). With the differences in the velocity field, we also observed that the wakes tend to be straight where the incident angle is at least 8^o or less; however, the morphodynamics and the closeness of the farm to the coast, can deviate the wake.

Finally, we calculated the theoretical power of the farm according to the different locations. We calculated the theoretical and not the real power because the last one depends on the device's design and capacity, and the limitations of the electric grid connection. The extractable power showed a clear tendency: cases with higher initial velocity in one regime (i.e., ebb or flood) presented a higher power in the same regime, while the cases with more significant power in the ebb and flood regimes coincide with the ones with a larger initial TKE.

After finishing our analyzes, we can say that we could use a high-resolution model to simulate the wakes interactions inside a farm of turbines to recognize the variables that dominate in the resistance force. After that, we could incorporate that in-

formation in a larger scale model to simulate the interaction of a farm of turbines with realistic tides and bathymetries. We showed that the same farm could affect the velocity, TKE, and bottom shear differently according to the initial and local conditions.

4.2 Thesis Contribution

This thesis's objective was to perform a multiscale analysis to represent a farm of turbines at the scales of the wakes and the tides. The importance of starting this work by using the high-resolution model, DES, was to recognize how the disposition of the devices affects an entire farm's resistance force. In Chapter II, we showed the parameters that dominate in the resistance force of a finite staggered farm, and most importantly, we provided a parameterization for calculating a thrust coefficient representative of a whole farm, C_{tFarm}. The advantage of this parameterization is to improve the MHK farms' representation of into OCM, by considering the distribution of the devices. Further, the calculation and use of C_{tFarm} into an OCM is easy so that it can be applied in any tidal channel.

In Chapter III, we used the parameterization in FVCOM to prove that our representation could be incorporated into a larger scale model. There, we showed how simple it was to simulate a specific finite staggered farm of turbines in a realistic tidal channel. Finally, we described the effects downstream of that farm at different locations, and we showed how the local condition could change the effects over velocity, TKE, and shear bottom downstream.

4.3 Future Work

Based on the results obtained in Chapter II, we propose that future works should be focused on expanding the parameterization of C_{tFarm} to other kinds of farms. For example, the aligned configuration should be included since it is the most studied

after the staggered configuration. Another significant improvement to C_{tFarm} could be the incorporation of an option to represent devices that interact with the free-surface. The last is because the MHK turbines still not converge to a unique design, and one of the promising devices are the floating ones coupled with offshore wind turbines.

On the other hand, to complement the results of Chapter III, we suggest simulating devices with a more significant distance to the bottom to observe if this way, the model can capture the erosion inside the farm. Future works should incorporate sediment transport to the OCM to describe how the turbines interact with a dynamic bathymetry that could even have bedforms with amplitudes larger than the diameter of the turbines.

Finally, we propose to execute another multiscale analysis to obtain a parameterization of devices interacting with the free-surface in a high-resolution model and incorporate it into an ocean circulation model that represents the waves.

APPENDIX A

NUMERICAL SIMULATIONS OF DEVICES IN CHACAO CHANNEL USING AN IMPROVED VERTICAL RESOLUTION

To discard errors due to a lack of nodes under the turbines, we run an extra simulation of case B in FVCOM with an improved vertical resolution (from ten to twenty-one sigma layers). In Figure A.1 we compare the velocity and TKE profiles of the cases with two different vertical resolutions. In the figure, we can observe a negligible disagreement between the profiles with different sigma layers. In Figure A.1(a) and (c) we also see that the velocity deficit starts from the bottom and is maximum around the center of the disks (12 m from the bottom). We propose our decrease in TKE at the bottom, and subsequently, τ_b is produced by the closeness of the disks to the bottom and the turbines density that do not allow the flow acceleration shown by Li et al. (2017).

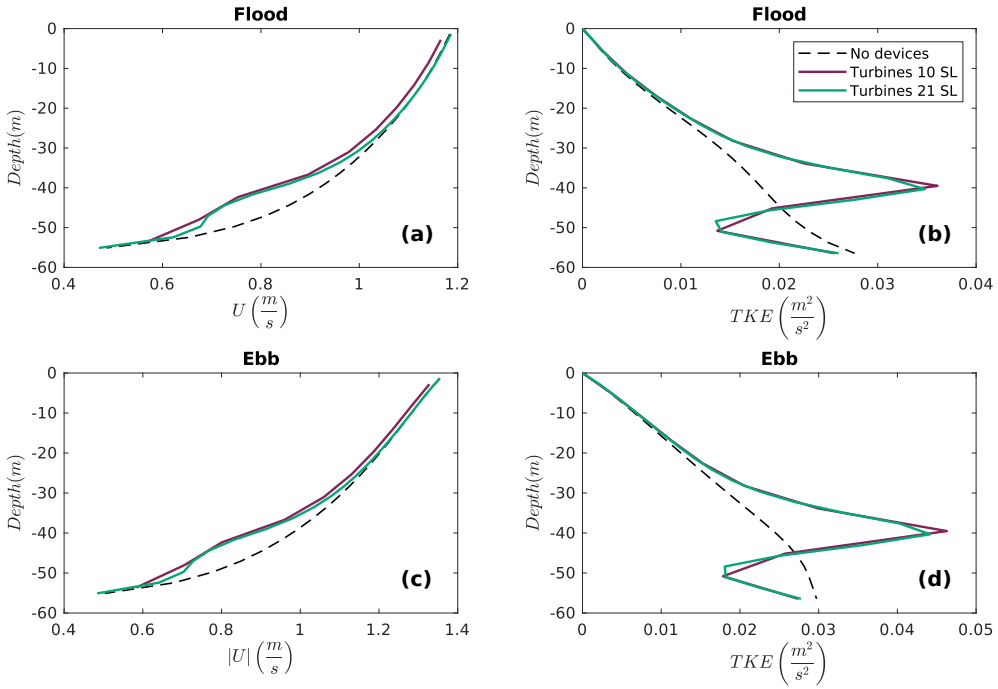

Figure A.1. Vertical velocity and TKE profiles at the center of the farm of case A in spanwise and streamwise directions. (a) and (b) are profiles for flood regime; meanwhile, (c) and (d) are profiles for the ebb regime. In purple, profiles obtained from the original simulations (i.e., using ten sigma layers). In green, profiles obtained by using 21 sigma layers in the simulations. In dashed lines, Profiles obtained from simulations without turbines and with 21 sigma layers.

BIBLIOGRAPHY

M. Abkar and F. Porté-Agel. A new wind-farm parameterization for large-scale atmospheric models. *Journal of Renewable and Sustainable Energy*, 7(1):013121, 2015. doi: 10.1063/1.4907600.

P. Aghsaee and C. D. Markfort. Effects of flow depth variations on the wake recovery behind a horizontal-axis hydrokinetic in-stream turbine. *Renewable Energy*, 125: 620–629, 2018. doi: 10.1016/j.renene.2018.02.137.

T. Blackmore, W. M. J. Batten, and A. S. Bahaj. Influence of turbulence on the wake of a marine current turbine simulator. *Proceedings of the Royal Society A: Mathematical, Physical and Engineering Sciences*, 470(2170):20140331, 2014. doi: 10.1098/rspa.2014.0331. URL `https://royalsocietypublishing.org/doi/abs/10.1098/rspa.2014.0331`.

M. Breuer, N. Jovičić, and K. Mazaev. Comparison of des, rans and les for the separated flow around a flat plate at high incidence. *International Journal for Numerical Methods in Fluids*, 41(4):357–388, 2003. doi: 10.1002/fld.445. URL `https://onlinelibrary.wiley.com/doi/abs/10.1002/fld.445`.

A. J. G. Brown and S. P. Neill. Hydrodynamic response to large scale tidal energy extraction. In *European Wave and Tidal Energy Conference 2015*, 2015.

T. Burton, D. Sharpe, N. Jenkins, and E. Bossanyi. *Wind Energy Handbook*. John Wiley & Sons, Ltd, Baffins Lane, Chichester West Sussex, PO19 1UD, England, 2011. ISBN: 0-471-48997-2.

M. Calaf, C. Meneveau, and J. Meyers. Large eddy simulation study of fully developed wind-turbine array boundary layers. *Physics of Fluids*, 22(1):015110, 2010. doi: 10.1063/1.3291077.

M. Calaf, M. B. Parlange, and C. Meneveau. Large eddy simulation study of scalar transport in fully developed wind-turbine array boundary layers. *Physics of Fluids*, 23(12):126603, 2011. doi: 10.1063/1.3663376.

L. P. Chamorro and F. Porté-Agel. Turbulent flow inside and above a wind farm: A wind-tunnel study. *Energies*, 4(11):1916–1936, 2011. doi: 10.3390/en4111916.

C. Chen, H. Liu, and R. C. Beardsley. An unstructured grid, finite-volume, three-dimensional, primitive equations ocean model: Application to coastal ocean and

estuaries. *Journal of Atmospheric and Oceanic Technology*, 20(1):159–186, 2003. doi: 10.1175/1520-0426(2003)020⟨0159:AUGFVT⟩2.0.CO;2.

Y. Chen, B. Lin, J. Lin, and S. Wang. Experimental study of wake structure behind a horizontal axis tidal stream turbine. *Applied energy*, 196:82 – 96, 2017. doi: 10.1016/j.apenergy.2017.03.126.

CNE, Chile. Reporte capacidad instalada generación. Technical report, Comisión Nacional de Energía, 2020.

A. Creech, W. G. Früh, and A. E. Maguire. Simulations of an offshore wind farm using large-eddy simulation and a torque-controlled actuator disc model. *Surveys in Geophysics*, 36(3):427–481, 2015. doi: 10.1007/s10712-015-9313-7.

J. Cruz, M. Thomson, and E. Stavroulia. Preliminary site selection - chilean marine energy resources. Technical report, Garrad Hassan and Partners Limited, 2009.

C. Daskiran, J. Riglin, and A. Oztekin. Computational study of multiple hydrokinetic turbines: the effect of wake. In *ASME International Mechanical Engineering Congress and Exposition*, volume 57465, page V07AT09A021. American Society of Mechanical Engineers, 2015.

M. D. Dominicis, R. O. Murray, and J. Wolf. Multi-scale ocean response to a large tidal stream turbine array. *Renewable Energy*, 114:1160 – 1179, 2017. ISSN 0960-1481. doi: 10.1016/j.renene.2017.07.058. URL `http://www.sciencedirect.com/science/article/pii/S096014811730678X`.

G. D. Egbert and S. Y. Erofeeva. Efficient inverse modeling of barotropic ocean tides. *Journal of Atmospheric and Oceanic Technology*, 19(2):183–204, 2002. doi: 10.1175/1520-0426(2002)019⟨0183:EIMOBO⟩2.0.CO;2.

O. Eriksson, M. Baltscheffsky, S.-P. Breton, S. Söderberg, and S. Ivanell. The long distance wake behind horns rev i studied using large eddy simulations and a wind-turbine parameterization in WRF. *Journal of Physics: Conference Series*, 854: 012012, may 2017. doi: 10.1088/1742-6596/854/1/012012.

C. Escauriaza and F. Sotiropoulos. Reynolds number effects on the coherent dynamics of the turbulent horseshoe vortex system. *Flow, Turbulence and Combustion*, 86 (2):231–262, Mar 2010. doi: 10.1007/s10494-010-9315-y.

C. Escauriaza and F. Sotiropoulos. Initial stages of erosion and bed form development in a turbulent flow around a cylindrical pier. *Journal of Geophysical Research: Earth Surface*, 116(F03007), 2011a. doi: 10.1029/2010JF001749.

C. Escauriaza and F. Sotiropoulos. Lagrangian model of bed-load transport in turbulent junction flows. *Journal of Fluid Mechanics*, 666:36–76, 2011b. doi: 10.1017/S0022112010004192.

I. Fairley, I. Masters, and H. Karunarathna. The cumulative impact of tidal stream turbine arrays on sediment transport in the pentland firth. *Renewable Energy*, 80:755 – 769, 2015. ISSN 0960-1481. doi: https://doi.org/10.1016/j.renene.2015.03.004. URL http://www.sciencedirect.com/science/article/pii/S096014811500186X.

R. Falconer, B. Lin, Y. Win, and E. Harris. Divast model reference manual (user manual). *Cardiff University, Hydro-Environmental Research Centre*, 2001.

D. Fallon, M. Hartnett, A. Olbert, and S. Nash. The effects of array configuration on the hydro-environmental impacts of tidal turbines. *Renewable Energy*, 64:10 – 25, 2014. ISSN 0960-1481. doi: 10.1016/j.renene.2013.10.035. URL http://www.sciencedirect.com/science/article/pii/S0960148113005661.

A. C. Fitch, J. B. Olson, J. K. Lundquist, J. Dudhia, A. K. Gupta, J. Michalakes, and I. Barstad. Local and mesoscale impacts of wind farms as parameterized in a mesoscale nwp model. *Monthly Weather Review*, 140(9):3017–3038, 2012. doi: 10.1175/MWR-D-11-00352.1.

C. Frost, P. Evans, M. Harrold, A. Mason-Jones, T. O'Doherty, and D. O'Doherty. The impact of axial flow misalignment on a tidal turbine. *Renewable Energy*, (113): 1333–1344, 2017. doi: http://dx.doi.org/10.1016/j.renene.2017.07.006.

D. Gajardo, C. Escauriaza, and D. M. Ingram. Capturing the development and interactions of wakes in tidal turbine arrays using a coupled bem-des model. *Ocean Engineering*, 181:71 – 88, 2019. doi: 10.1016/j.oceaneng.2019.03.064.

M. Garcia-Oliva, S. Djordjević, and G. R. Tabor. The influence of channel geometry on tidal energy extraction in estuaries. *Renewable Energy*, 101:514 – 525, 2017. doi: 10.1016/j.renene.2016.09.009.

B. Gaylord. Hydrodynamic context for considering turbulence impacts on external fertilization. *The Biological Bulletin*, 214(3):315–318, 2008. doi: 10.2307/25470672. URL https://doi.org/10.2307/25470672. PMID: 18574107.

A. B. Gill. Offshore renewable energy: Ecological implications of generating electricity in the coastal zone. *Journal of Applied Ecology*, 42(4):605–615, 2005. ISSN 00218901, 13652664. doi: 10.1111/j.1365-2664.2005.01060.x.

A. J. Goward Brown, S. P. Neill, and M. J. Lewis. Tidal energy extraction in three-dimensional ocean models. *Renewable Energy*, 114:244 – 257, 2017. ISSN 0960-1481. doi: 10.1016/j.renene.2017.04.032. URL http://www.sciencedirect.com/science/article/pii/S0960148117303397. Wave and Tidal Resource Characterization.

E. Gringarten and C. V. Deutsch. Teacher's aide variogram interpretation and modeling. *Mathematical Geology*, 33(4):507–534, 2001. ISSN 1573-8868. doi: 10.1023/A:1011093014141. URL https://doi.org/10.1023/A:1011093014141.

M. Guerra, R. Cienfuegos, J. Thomson, and L. Suarez. Tidal energy resource characterization in chacao channel, chile. *International Journal of Marine Energy*, 20: 1–16, 2017. doi: https://doi.org/10.1016/j.ijome.2017.11.002.

N. Guillou and J. Thiébot. The impact of seabed rock roughness on tidal stream power extraction. *Energy*, 112:762 – 773, 2016. doi: 10.1016/j.energy.2016.06.053.

G. Hagerman, B. P. B, R. Bedard, and M. Previsic. Epri guideline methodology for estimating tidal current energy resources and power production by tidal in-stream energy conversion (tisec) devices. Technical report, Electric Power Research Institute, 2006.

C. Hill, M. Musa, and M. Guala. Interaction between instream axial flow hydrokinetic turbines and uni-directional flow bedforms. *Renewable Energy*, 86:409 – 421, 2016. doi: 10.1016/j.renene.2015.08.019.

J. T. Holt and I. D. James. An s coordinate density evolving model of the northwest european continental shelf: 1. model description and density structure. *Journal of Geophysical Research: Oceans*, 106(C7):14015–14034, 2001. doi: 10.1029/2000JC000304. URL `https://agupubs.onlinelibrary.wiley.com/doi/abs/10.1029/2000JC000304`.

IEA and World Bank. Sustainable energy for all. Available online: `https://datacatalog.worldbank.org/dataset/sustainable-energy-all` (accessed on 18 March 2019), 2015.

S. Kang, I. Borazjani, J. Colby, and F. Sotiropoulos. Numerical simulation of 3d flow past a real-life marine hydrokinetic turbine. *Advances in Water Resources*, 39, 2012. doi: 10.1016/j.advwatres.2011.12.012.

S. Kang, L. Chamorro, C. Hill, R. Arndt, and F. Sotiropoulos. Flow structure interaction around an axial-flow hydrokinetic turbine: Experiments and CFD simulations. *Journal of Physics: Conference Series*, 555:012097, 2014. doi: 10.1088/1742-6596/555/1/012097.

A. E. Kasmi and C. Masson. An extended k– model for turbulent flow through horizontal-axis wind turbines. *Journal of Wind Engineering and Industrial Aerodynamics*, 96(1):103 – 122, 2008. doi: 10.1016/j.jweia.2007.03.007.

N. Kolekar and A. Banerjee. Performance characterization and placement of a marine hydrokinetic turbine in a tidal channel under boundary proximity and blockage effects. *Applied Energy*, 148:121 – 133, 2015. doi: 10.1016/j.apenergy.2015.03.052.

S. C. Kramer and M. D. Piggott. A correction to the enhanced bottom drag parameterisation of tidal turbines. *Renewable Energy*, 92:385 – 396, 2016. ISSN 0960-1481. doi: https://doi.org/10.1016/j.renene.2016.02.022.

X. Li, M. Li, S. J. McLelland, L.-B. Jordan, S. M. Simmons, L. O. Amoudry, R. Ramirez-Mendoza, and P. D. Thorne. Modelling tidal stream turbines in a three-dimensional wave-current fully coupled oceanographic model. *Renewable Energy*, 114:297 – 307, 2017. doi: 10.1016/j.renene.2017.02.033.

T. P. Lloyd, S. R. Turnock, and V. F. Humphrey. Assessing the influence of inflow turbulence on noise and performance of a tidal turbine using large eddy simulations. *Renewable Energy*, 71:742–754, 2014. doi: 0.1016/j.renene.2014.06.011.

N. Marjanovic, J. D. Mirocha, B. Kosović, J. K. Lundquist, and F. K. Chow. Implementation of a generalized actuator line model for wind turbine parameterization in the weather research and forecasting model. *Journal of Renewable and Sustainable Energy*, 9(6):063308, 2017. doi: 10.1063/1.4989443.

D. M. Mark and P. B. Aronson. Scale-dependent fractal dimensions of topographic surfaces: An empirical investigation, with applications in geomorphology and computer mapping. *Journal of the International Association for Mathematical Geology*, 16(7):671–683, 1984. doi: 10.1007/BF01033029.

C. D. Markfort, W. Zhang, and F. Porté-Agel. Turbulent flow and scalar transport through and over aligned and staggered wind farms. *Journal of Turbulence*, 13 (33), 2012. doi: 10.1080/14685248.2012.709635.

G. L. Mellor and T. Yamada. Development of a turbulence closure model for geophysical fluid problems. *Reviews of Geophysics*, 20(4):851–875, 1982. doi: 10.1029/RG020i004p00851.

J. Meyers and C. Meneveau. Optimal turbine spacing in fully developed wind farm boundary layers. *Wind Energy*, 15(2):305–317, 2012. doi: 10.1002/we.469.

R. F. Mikkelsen and J. N. Sørensen. *Actuator disc methods applied to wind turbines*. Degree of doctor of philosophy in mechanical engineering, Technical University of Denmark, 2003.

D. N. Moriasi, J. G. Arnold, M. W. Van Liew, R. L. Bingner, R. D. Harmel, and T. L. Veith. Model evaluation guidelines for systematic quantification of accuracy in watershed simulations. *Transactions of the ASABE*, 50(3):885–900, 2007. doi: 10.13031/2013.23153.

R. O. Murray and A. Gallego. A modelling study of the tidal stream resource of the pentland firth, scotland. *Renewable Energy*, 102:326 – 340, 2017. doi: https://doi.org/10.1016/j.renene.2016.10.053.

M. Musa, C. Hill, F. Sotiropoulos, and M. Guala. Performance and resilience of hydrokinetic turbine arrays under large migrating fluvial bedforms. *Nature Energy*, 3(10):839–846, 2018. doi: 10.1038/s41560-018-0218-9.

M. Musa, C. Hill, and M. Guala. Interaction between hydrokinetic turbine wakes and sediment dynamics: array performance and geomorphic effects under different siting strategies and sediment transport conditions. *Renewable Energy*, 138:738 – 753, 2019. doi: 10.1016/j.renene.2019.02.009.

M. Musa, G. Ravanelli, W. Bertoldi, and M. Guala. Hydrokinetic turbines in yawed conditions: Toward synergistic fluvial installations. *Journal of Hydraulic Engineering*, 146(4):04020019, 2020. doi: 10.1061/(ASCE)HY.1943-7900.0001707.

L. Myers and A. Bahaj. An experimental investigation simulating flow effects in first generation marine current energy converter arrays. *Renewable Energy*, 37:28–36, 2012. doi: https://doi.org/10.1016/j.renene.2011.03.043.

L. Myers and A. Bahaj. Experimental analysis of the flow field around horizontal axis tidal turbines by use of scale mesh disk rotor simulators. *Ocean Engineering*, 37(2):218 – 227, 2010. doi: 10.1016/j.oceaneng.2009.11.004.

S. Nash, N. O'Brien, A. Olbert, and M. Hartnett. Modelling the far field hydro-environmental impacts of tidal farms – a focus on tidal regime, inter-tidal zones and flushing. *Computers Geosciences*, 71:20–27, 2014. doi: 10.1016/j.cageo.2014.02.001. Marine Renewable Energy.

S. P. Neill, J. R. Jordan, and S. J. Couch. Impact of tidal energy converter (tec) arrays on the dynamics of headland sand banks. *Renewable Energy*, 37(1):387 – 397, 2012. ISSN 0960-1481. doi: 10.1016/j.renene.2011.07.003. URL `http://www.sciencedirect.com/science/article/pii/S0960148111003855`.

T. Nishino and R. H. J. Willden. The efficiency of an array of tidal turbines partially blocking a wide channel. *Journal of Fluid Mechanics*, 708:596–606, 2012. doi: 10.1017/jfm.2012.349.

P. Ouro and T. Stoesser. An immersed boundary-based large-eddy simulation approach to predict the performance of vertical axis tidal turbines. *Computers Fluids*, 152:74 – 87, 2017. ISSN 0045-7930. doi: 10.1016/j.compfluid.2017.04.003.

P. Ouro, L. Ramírez, and M. Harrold. Analysis of array spacing on tidal stream turbine farm performance using large-eddy simulation. *Journal of Fluids and Structures*, 91:102732, 2019. ISSN 0889-9746. doi: 10.1016/j.jfluidstructs.2019.102732.

D. M. O'Doherty, A. Mason-Jones, C. Morris, T. O'Doherty, C. Byrne, P. W. Prickett, and R. I. Grosvenor. Interaction of marine turbines in close proximity. In *9th European Wave and Tidal Energy Conference (EWTEC). Southampton, UK*, pages 10–14, 2011.

S. Paboeuf, P. Yen Kai Sun, L.-M. Macadré, and G. Malgorn. Power performance assessment of the tidal turbine sabella d10 following iec62600-200. volume Volume 6: Ocean Space Utilization; Ocean Renewable Energy of *International Conference on Offshore Mechanics and Arctic Engineering*, 2016. doi: 10.1115/OMAE2016-54836.

G. Peebles and E. Johnson. Bathymetric effects on marine hydrokinetic turbine array optimization. In *World Environmental and Water Resources Congress 2015*, pages 1302–1311, 2015. doi: 10.1061/9780784479162.128.

M. Piano, P. Robins, A. Davies, and S. Neill. The influence of intra-array wake dynamics on depth-averaged kinetic tidal turbine energy extraction simulations. *Energies*, 11(10):2852, Oct 2018. ISSN 1996-1073. doi: 10.3390/en11102852. URL http://dx.doi.org/10.3390/en11102852.

D. R. Plew and C. L. Stevens. Numerical modelling of the effect of turbines on currents in a tidal channel – tory channel, new zealand. *Renewable Energy*, 57: 269 – 282, 2013. ISSN 0960-1481. doi: 10.1016/j.renene.2013.02.001. URL http://www.sciencedirect.com/science/article/pii/S096014811300092X.

S. B. Pope. *Turbulent flows*. Cambridge University Press, Cambridge, 2000. ISBN: 978-0-521-59886-6.

F. Porté-Agel, Y.-T. Wu, H. Lu, and R. J. Conzemius. Large-eddy simulation of atmospheric boundary layer flow through wind turbines and wind farms. *Journal of Wind Engineering and Industrial Aerodynamics*, 99(4):154 – 168, 2011. ISSN 0167-6105. doi: 10.1016/j.jweia.2011.01.011. URL http://www.sciencedirect.com/science/article/pii/S0167610511000134. The Fifth International Symposium on Computational Wind Engineering.

F. Porté-Agel, H. Lu, and Y.-T. Wu. Interaction between large wind farms and the atmospheric boundary layer. *Procedia IUTAM*, 10:307 – 318, 2014a. ISSN 2210-9838. doi: 10.1016/j.piutam.2014.01.026. Mechanics for the World: Proceedings of the 23rd International Congress of Theoretical and Applied Mechanics, ICTAM2012.

F. Porté-Agel, H. Lu, and Y.-T. Wu. Interaction between large wind farms and the atmospheric boundary layer. *Procedia IUTAM*, 10:307 – 318, 2014b. ISSN 2210-9838. doi: https://doi.org/10.1016/j.piutam.2014.01.026. URL http://www.sciencedirect.com/science/article/pii/S2210983814000273. Mechanics for the World: Proceedings of the 23rd International Congress of Theoretical and Applied Mechanics, ICTAM2012.

K. Rados, J. Prospathopoulos, N. C. Stefanatos, E. Politis, P. Chaviaropoulos, and A. Zervos. Cfd modeling issues of wind turbine wakes under stable atmospheric conditions. In *European Wind Energy Conference and Exhibition 2009, EWEC 2009*, 2009.

V. Ramos, R. Carballo, and J. V. Ringwood. Application of the actuator disc theory of delft3d-flow to model far-field hydrodynamic impacts of tidal turbines. *Renewable Energy*, 139:1320 – 1335, 2019. ISSN 0960-1481. doi: 10.1016/j.renene.2019.02.094.

J. Riglin, W. Chris Schleicher, I.-H. Liu, and A. Oztekin. Characterization of a micro-hydrokinetic turbine in close proximity to the free surface. *Ocean Engineering*, 110:270 – 280, 2015. ISSN 0029-8018. doi: https://doi.org/10.1016/j.oceaneng.2015.10.026. URL `http://www.sciencedirect.com/science/article/pii/S0029801815005636`.

J. Riglin, C. Daskiran, J. Jonas, W. C. Schleicher, and A. Oztekin. Hydrokinetic turbine array characteristics for river applications and spatially restricted flows. *Renewable Energy*, 97:274 – 283, 2016. ISSN 0960-1481. doi: https://doi.org/10.1016/j.renene.2016.05.081. URL `http://www.sciencedirect.com/science/article/pii/S0960148116304918`.

P. E. Robins, S. P. Neill, M. J. Lewis, and S. L. Ward. Characterising the spatial and temporal variability of the tidal-stream energy resource over the northwest european shelf seas. *Applied Energy*, 147:510 – 522, 2015. doi: 10.1016/j.apenergy.2015.03.045.

T. Roc, D. Conley, and D. Greaves. Methodology for tidal turbine representation in ocean circulation model. *Renewable Energy*, 51:448–464, 2013. doi: https://doi.org/10.1016/j.renene.2012.09.039.

P.-E. Réthoré, N. Sørensen, A. Bechmann, and F. Zhale. Study of the atmospheric wake turbulence of a cfd actuator disc model. *EWEC 2009*, 2009.

W. Schleicher, J. Riglin, and A. Oztekin. Numerical characterization of a preliminary portable micro-hydrokinetic turbine rotor design. *Renewable Energy*, 76:234 – 241, 2015. ISSN 0960-1481. doi: https://doi.org/10.1016/j.renene.2014.11.032. URL `http://www.sciencedirect.com/science/article/pii/S0960148114007472`.

J. Schluntz and R. Willden. The effect of blockage on tidal turbine rotor design and performance. *Renewable Energy*, 81:432 – 441, 2015. doi: 10.1016/j.renene.2015.02.050.

A. Shchepetkin and J. McWilliams. The regional oceanic modeling system (roms): oceanic model. *Ocean Modelling*, 9, 2005. doi: 10.1016/j.ocemod.2004.08.002.

A. Simón-Moral, J. L. Santiago, E. S. Krayenhoff, and A. Martilli. Streamwise versus spanwise spacing of obstacle arrays: Parametrization of the effects on drag and turbulence. *Bound-Layer Meteorology*, 151(3):579–596, Jun 2014. doi: 10.1007/s10546-013-9901-3.

A. Smirnov, S. Shi, and I. Celic. Random flow generation technique for large eddy simulations and particle-dynamics modeling. *Journal of Fluids Engineering*, 123:359–371, 2001. doi: 10.1115/1.1369598.

J. N. Sørensen and W. Z. Shen. Numerical modeling of wind turbine wakes. *Journal of fluids engineering*, 124(2):393–399, 2002. doi: 10.1115/1.1471361.

K. Soto-Rivas, D. Richter, and C. Escauriaza. A formulation of the thrust coefficient for representing finite-sized farms of tidal energy converters. *Energies*, 12(20):3861, 2019. doi: 10.3390/en12203861.

P. Spalart and S. Allmaras. A one-equation turbulence model for aerodynamic flows. In *30th Aerospace Sciences Meeting and Exhibit*, 1992. doi: 10.2514/6.1992-439. URL `https://arc.aiaa.org/doi/abs/10.2514/6.1992-439`.

T. Stallard, R. Collings, T. Feng, and J. Whelan. Interactions between tidal turbine wakes: experimental study of a group of three-bladed rotors. *Philosophical Transactions of the Royal Society of London: A*, 371(1985):20120159, 2013. doi: 10.1098/rsta.2012.0159.

P. Stansby and T. Stallard. Fast optimisation of tidal stream turbine positions for power generation in small arrays with low blockage based on superposition of self-similar far-wake velocity deficit profiles. *Renewable Energy*, 92:366 – 375, 2016. doi: 10.1016/j.renene.2016.02.019.

R. J. Stevens, L. A. Martínez-Tossas, and C. Meneveau. Comparison of wind farm large eddy simulations using actuator disk and actuator line models with wind tunnel experiments. *Renewable Energy*, 116:470 – 478, 2018. doi: 10.1016/j.renene.2017.08.072.

J. N. Sørensen, W. Z. Shen, and X. Munduate. Analysis of wake states by a full-field actuator disc model. *Wind Energy*, 1(2):73–88, 1998. doi: 10.1002/(SICI)1099-1824(199812)1:2⟨73::AID-WE12⟩3.0.CO;2-L.

M. Tarbotton and M. Larson. Canada ocean energy atlas phase 1 : potential tidal current energy resources analysis background, 2006.

J. Thiébot, P. B. du Bois, and S. Guillou. Numerical modeling of the effect of tidal stream turbines on the hydrodynamics and the sediment transport – application to the alderney race (raz blanchard), france. *Renewable Energy*, 75:356 – 365, 2015. doi: 10.1016/j.renene.2014.10.021.

J. Thiébot, S. Guillou, and V. T. Nguyen. Modelling the effect of large arrays of tidal turbines with depth-averaged actuator disks. *Ocean Engineering*, 126:265 – 275, 2016. doi: 10.1016/j.oceaneng.2016.09.021.

B. J. Vanderwende, B. Kosović, J. K. Lundquist, and J. D. Mirocha. Simulating effects of a wind-turbine array using les and rans. *Journal of Advances in Modeling Earth Systems*, 8:1376–1390, 2016. doi: 10.1002/2016MS000652.

T. Wang and Z. Yang. A modeling study of tidal energy extraction and the associated impact on tidal circulation in a multi-inlet bay system of puget sound. *Renewable Energy*, 114:204–214, 2017. ISSN 0960-1481. doi: 10.1016/j.renene.2017.03.049. URL `http://www.sciencedirect.com/science/article/pii/S0960148117302409`. Wave and Tidal Resource Characterization.

Y.-T. Wu and F. Porté-Agel. Simulation of turbulent flow inside and above wind farms: Model validation and layout effects. *Boundary-Layer Meteorology*, 146(2): 181–205, Feb 2013. doi: 10.1007/s10546-012-9757-y.

Z. Yang, T. Wang, and A. E. Copping. Modeling tidal stream energy extraction and its effects on transport processes in a tidal channel and bay system using a three-dimensional coastal ocean model. *Renewable Energy*, 50:605 – 613, 2013. doi: 10.1016/j.renene.2012.07.024.

Z. Yang, T. Wang, A. Copping, and S. Geerlofs. Modeling of in-stream tidal energy development and its potential effects in tacoma narrows, washington, usa. *Ocean and Coastal Management*, 99:52 – 62, 2014. ISSN 0964-5691. doi: 10.1016/j.ocecoaman.2014.02.010. Science in support of governance of wave and tidal energy developments.